DOCTORAT BRETAGNE LOIRE SCIENCES POUR L'INGENIEUR

Oniris
École Nationale Vétérinaire, Agroalimentaire et de l'Alimentation — Nantes Atlantique
Santé et alimentation au cœur de la vie

UNIVERSITÉ DE NANTES

THESE DE DOCTORAT DE

ONIRIS
DELIVREE CONJOINTEMENT AVEC
L'UNIVERSITE DE NANTES

ECOLE DOCTORALE N° 602
Sciences pour l'Ingénieur
Spécialité : Génie des Procédés et Bioprocédés

BADRI Deyae

Numerical study of frost formation on an industrial food freezing system

Thèse présentée et soutenue à Oniris, Nantes, le 09 Décembre 2021

Unité de recherche : GEPEA

Thèse N° :

Rapporteurs avant soutenance :

Jocelyn BONJOUR Professeur – INSA LYON
Vincent LEMORT Professeur – Université de Liège

Composition du Jury :

Président : Pr Assaad ZOUGHAIB

Examinateurs :	Assaad ZOUGHAIB	Professeur – MINES ParisTech
	Hong Minh HOANG LE	Chargée de recherche – INRAE Antony
	Jocelyn BONJOUR	Professeur – INSA LYON
	Vincent LEMORT	Professeur – Université de Liège
Dir. de thèse :	Michel HAVET	Professeur – Oniris
Co-dir. de thèse :	Olivier ROUAUD	Professeur – Oniris
Co-enc. de thèse :	Cyril TOUBLANC	Maître de conférence – Oniris

Preface

This thesis work carried out within the Joined Research Unit GEPEA (UMR 6144, CNRS, ONIRIS, University of Nantes, IMT-Atlantique) is as part of the ADEME FOODEFREEZE project coordinated by Cyril TOUBLANC from GEPEA laboratory. This project concerns the management of frost in industrial freezers and includes academic (ONIRIS) and industrial (AQUIMER, GEA, CRITT, & CETIAT) partners. The project is subdivided into different tasks, one of which concerns this thesis work: dynamic modeling of a complete industrial food freezing system under frosting conditions.

This work, sponsored by French Environment and Energy Management Agency ADEME, has been carried out in the period from October 2018 to December 2021 under the supervision of professor Michel HAVET, associate professor Cyril TOUBLANC, and professor Olivier ROUAUD.

Oniris, GEPEA Laboratory, December 2021

BADRI Deyae

Dedication

This thesis is dedicated

to my mother, TAZI Naila, and my father, BADRI Abdellatif who cares a lot for my education with infinite love and affection. No dedication could be enough to express what you both deserve for all the sacrifices you have made for me. May God preserve you and blesses you with good health, long life and happiness.

to my brothers Kamal, Ayoub and Mohammed, my faithful companions. I love you.

to the person who means a lot to me, my best friend, OUAZZANI CHAHIDI Laila who was there for me throughout this process and gave me lots of love and support. I miss you.

to my supervisors, HAVET Michel, TOUBLANC Cyril, and ROUAUD Olivier. A special and sincere thanks to you for all your efforts. You have always been here for me. May this work be the expression of my gratitude and respect.

To my grandparents.

To my aunts and uncles.

To all my family, young and old.

To my friends.

Acknowledgments

I would like to express my sincere thanks to all those who have contributed to the achievement of this work.

I would like to express my gratitude to my supervisor Prof. HAVET Michel, for the confidence, the support he gave me, and the knowledge he shared with me. His immense knowledge and plentiful experience have encouraged me in all the time of this academic research and daily life.

I also express my gratitude to my co-supervisor Dr. TOUBLANC Cyril for his availability, kindness, and for human qualities of generosity, support and precious help in the most delicate moments. Despite the occupations and the responsibilities he assumes, he always had time to listen to me, advise me, and answer all my questions.

I would like to thank my co-supervisor Prof. ROUAUD Olivier for his continuous support, kind help and patience during my PhD study. Meeting and working with brilliant team allowed me to progress and to feel supported and surrounded.

My grateful thanks to the technical staff who greatly contributed to the success of this project, Mr. GUIHARD Luc, and Mrs. CHEVALLIER Sylvie.

Many thanks must be given to the ADEME for the financial support, to the FOODEFREEZE partners as well as the dedicated staff of CETIAT who provided relevant experimental data used to consolidate and approve the numerical model. I also wish to thank Mr. AUFFRET Yannick for sharing his expertise in refrigeration systems.

I extend my sincere thanks to all the jury members for agreeing to read the manuscript and to participate in the defense of this thesis.

Finally, I would like to thank my wonderful mam and dad, my brothers, my family and my friends for their love and unequivocal support. Without their encouragement, this achievement would not have been possible.

Table of Contents

Preface 2

Dedication 3

Acknowledgments 4

Index of figures 8

Index of tables 11

Nomenclature 12

General Introduction 15

CHAPTER I: Background, research motivation and literature review 19

I.1. Fundamentals and background 19

I.2. Problem formulation 22

I.3. Research motivations and objectives 23

I.4. Literature Review 25

I.4-1. Preliminary overview of research on industrial freezing conditions 25

I.4-2. Frost formation process, frost growth and frost properties 29

I.4-3. Frost Effects 46

I.4-4. Frost management techniques 50

I.5. Summary and conclusion 57

CHAPTER II: Frost modeling for a system approach 61

II.1. Freezing system description 61

II.2. System modeling architecture and procedure 63

II.3. Development and validation of a frost model adapted to a system approach 66

II.3-1. Main concept and assumptions 66

II.3-2. At frost/air interface 68

II.3-3. Inside the frost layer 68

II.3-4. Correlations and initial conditions 71

II.3-5. Frost model Validation 74
II.4. Summary: 90
CHAPTER III: Numerical and experimental study of an industrial freezer under frosting conditions 92
III.1. Evaporator model 92
III.2. Fan model 94
III.3. Compressor model 96
III.4. Tank model 99
III.5. Valve model 100
III.6. Pump model 100
III.7. Condenser model 101
III.8. Cooling tower model 101
III.9. Tunnel and product 103
III.9-1. Freezer Space 103
III.10. System control 104
III.11. Experiment and instrumentation 105
III.11-1. Pressures and air velocity 105
III.11-2. Air and refrigerant temperatures 106
III.11-3. Air-product heat exchange quality 107
III.11-4. Product water losses 108
III.11-5. Frost growth and evaporator cross section area 109
III.12. Results and discussions 111
III.12-1. Fan pressure, Evaporator and tunnel pressure drop. 111
III.12-2. Evaporator cross section area 112
III.12-3. Air-product heat transfer coefficient 113
III.13. Summary 114

CHAPTER IV: Results analysis and sensitivity study 116
IV.1. Nominal conditions 116
IV.1-1. Local Analysis 116
IV.1-2. System-level Analysis 121
IV.1-3. Product quality analysis 125
IV.2. Sensitivity Study and optimization strategies 128
IV.2-1. Product water losses. 128
IV.2-2. Fan control mode 136
IV.3. Summary 140
Conclusions and future works 141
References 145

Index of figures

Figure I.1: Schematic of a spiral air blast freezer under frosting conditions. 20

Figure I.2: Different types of air blast freezers: a) tunnel freezers, b) single belt freezer, c) spiral belt freezer, d) fluidized bed freezer. 21

Figure I.3: Distribution of numerical and experimental works on frosting and defrosting published from 1957 to 2020. 26

Figure I.4: Data analysis of Frosting/Defrosting studies (numerical and experimental) – (a) Wall Temperature range (b) Air Temperature range..... 27

Figure I.5: Data analysis of Frosting/Defrosting studies (Numerical and Experimental) – Air velocity. 28

Figure I.6: Data analysis of Frosting/Defrosting studies (Numerical and Experimental) – Operating Conditions. 30

Figure I.7: Effect of surface temperature and air humidity on the shape of the earliest ice crystals; I: super-cooled water droplets, II: irregular crystals, III: flake crystals, IV: needle and pole crystals, V: feather crystals [48]. 31

Figure I.8: Airflow in a CFD Simulation when a highly porous frost is formed, adapted from [81]. 38

Figure I.9: Transport phenomena in a porous frost layer. 39

Figure I.10: Illustration of mass transfer in an industrial freezer. 41

Figure I.11: Schematic of freezer air infiltration. 42

Figure I.12: Psychrometric diagram - Air heat and mass transfer through coil - favorable and unfavorable frost theory. 44

Figure I.13: Unfavorable and favorable frosting conditions on a psychrometric chart [108]. 45

Figure I.14: Variation of overall heat transfer coefficient with frost thickness for different fin spacing (Tevap=-10 °C, Vair =3 m/s) [109]. 46

Figure I.15: Coil performance and airflow rates in frosting conditions as a function of time, adapted from [116]. 49

Figure I.16: Coil performance and airflow rates in frosting conditions as a function of frost mass, adapted from [116]. 49

Figure I.17: Unfavorable frost forming due to the presence of supersaturated air or/and a high coil temperature difference..... 50

Figure I.18: Frost mass reduction versus applied voltage and evaporation temperature (T_{air} = 0 °C, RH = 80%, V_{air} = 3 m/s, t = 10,800 s) [131]. 53

Figure I.19: Dehydration losses during freezing versus the inlet product temperature. 56

Figure II.1: Schematic of the freezing system & P-h diagram. 61

Figure II.2: Freezing system modeling architecture. 64

Figure II.3: Heat and mass transfer on frost surface and inside frost layer. 67

Figure II.4: Experimental and numerical frost thickness at T_{wall} = -25 °C, T_a = 13 °C, ωa= 0.0039 kg/kg, V_a = 2.12 m/s – Case 1A. 75

Figure II.5. Experimental and numerical frost thickness at T_{wall} = -9 °C, T_a = 13 °C,ωa= 0.0069 kg/kg, V_a = 2.18 m/s – Case 2A. 75

Figure II.6: Experimental and numerical frost thickness at T_{wall} = -15 °C, T_a =13 °C, ωa = 0.0069 kg/kg, V_a = 2.18 m/s – Case 3A. 76

Figure II.7: Temporal variation of mass flux in case 1A and case 2A. 77

Figure II.8: Frost density versus time in case 2A and case 3A. 78

Figure II.9: Experimental setup, Mao et al. [31]. 79

Figure II.10: Cells basic element for the finned tube heat exchanger. 81

Figure II.11: Schematic representation of the void ratio of a finned tube heat exchanger. 84

Figure II.12: Simplified front view of a frosted finned tube heat exchanger. 85

Figure II.13: Schematic view of the discretization for the finned tube heat exchanger reported by. Padhmanabhan et al. [174]. 86

Figure II.14: Measured and simulated frost thickness at V_a = 0.96 m/s, T_{ref} = -22.8 °C, RH = 82%, T_a = 1.7 °C. 89

Figure III.1: Schematic presentation of evaporator geometry of the freezing system. 93

Figure III.2: Axial and centrifuge fan operating zones 95

Figure III.3: Screw compressor with slide valve. 96

Figure III.4: Example of relationship of slide valve position and swept volume. 97

Figure III.5: Comparison between compressor shaft power between the model and constructor data for HP Compressor. 98

Figure III.6: Comparison between compressor shaft power between the model and constructor data for LP Compressor 98

Figure III.7: Condenser geometry. 101

Figure III.8: Air loop model on Dymola layout. 103

Figure III.9: Air velocity measured on the frontal side of the evaporator (measured by CETIAT). 106

Figure III.10: Thermocouples location at the entrance of the evaporator 106

Figure III.11: Airflow device for air-product convective heat transfer coefficient measurement 107

Figure III.12: First air-product convective heat transfer coefficient measurements as function of the position on the conveyor belt. 108

Figure III.13: Location of the recording camera in front of the evaporator 109

Figure III.14: Image processing - Coil and free section mask. 110

Figure III.15: Example of image processing. 110

Figure III.16: Experimental and numerical results: Fan pressure, pressure drop through the evaporator coil and tunnel. 111

Figure III.17: Experimental and numerical results of the cross section area opening ratio. 112

Figure III.18: Experimental and numerical results: Air-product convective heat transfer coefficient. 113

Figure IV.1: Frost Thickness distribution along the evaporator. 117

Figure IV.2: Frost morphology and distribution on the cross section area. 118

Figure IV.3: Frost density distribution along the airflow direction. 119

Figure IV.4: Comparison between air-side and frost layer thermal resistances 120

Figure IV.5: Air volume flow rate and cooling capacity. 120

Figure IV.6: Compressors' Volumetric efficiencies and Drivers' positions. 122

Figure IV.7: Freezer temperature evolution. 123

Figure IV.8: Instantaneous and average COP of the freezing system. 124

Figure IV.9: Cooling energy and energy consumption of each component of the freezing system as function of time. 125

Figure IV.10: Practical definition of the freezing process. 126

Figure IV.11: Effects of food water losses on cooling capacity. 129

Figure IV.12: Sensitivity of the airflow and pressure drop to food water losses. 130

Figure IV.13: Fan operating points for different amount of product water losses 131

Figure IV.14: Cross section area blockage ratio for different amounts of moisture released by products. 131

Figure IV.15: Schematic of evaporator geometry sections for frost mass analysis. 132

Figure IV.16: Frost mass for different amounts of moisture released by products. 134

Figure IV.17: Air-product heat transfer coefficient and air velocity depending on product water losses. 135

Figure IV.18: Frost thickness at the leading edge under different fun control modes 136

Figure IV.19: Cooling capacity versus time under different fan control mode. 138

Figure IV.20: Fan shaft power under different control modes 139

Index of tables

Table I.1: Summary of air blast freezers characteristics (Adapted from [9], [10]). 22

Table I.2: Experimental and numerical studies of frosting/defrosting under freezing conditions. 29

Table I.3: Frost thickness and air velocity relationship interpretation in the literature. 34

Table I.4: Correlations of Rough and Smooth frost surface for frost properties under freezer operating conditions [31]. 36

Table II.1: Freezing system data and operating conditions. 62

Table II.2: Empirical coefficients of the diffusion coefficient equation. 72

Table II.3: Experimental Conditions used for frost validation. 74

Table II.4: Experimental operating conditions used for validation, from Mao et al. [31]. 79

Table II.5: Experimental and numerical results for frost characteristics under freezing conditions, using data from Mao et al. [31]. 80

Table II.6: Finned tube heat exchanger geometric data used for frost model validation [174]. 86

Table III.1: Evaporator fan parameters. 94

Table III.2: Key parameters for the LP and HP compressors. 99

Table III.3: Condenser geometric data. 101

Table III.4: Minimum and maximum limits for approach temperature in York and Actual models. 102

Table III.5: Experimental results of the amount of food water losses during freezing. 109

Table IV.1: Pizza ingredients and thermal properties [169]. 127

Table IV.2: Energy performance and food quality indicators at the end of one production day - 15 hours. 128

Table IV.3: Summary of the numerical conditions for product water losses sensitivity analysis. 129

Table IV.4: Sensitivity of frost properties to food water losses. 134

Table IV.5: Sensitivity of energy performance and food quality to food water losses within 12 hours. 135

Table IV.6: Energy performance and productivity under different fan control modes. 138

Nomenclature

$\mathbf{A_w}$	water activity ($= \frac{p_v}{p_{sat}}$)
$\boldsymbol{A}$	Area (m²)
Bi	Biot number
$\boldsymbol{C}$	specific heat capacity of air (J/kg^{-1}.K^{-1})
$\mathbf{C_{vap\text{-}eq}}$	water vapor concentration in equilibrium with the product surface (kg.m^{-3})
$\mathbf{C_{vap\text{-}sur}}$	water vapor concentration in the surrounding air (kg.m^{-3})
d	diameter (m)
D	water vapor diffusion coefficient (m².s^{-1})
E	energy transfer coefficient (W.m^{-2}.K^{-1})
Fl	filing level (m^3)
$\mathbf{F_o}$	Fourrier number
h	specific enthalpy (J.kg^{-1})
$\mathbf{h_m}$	vaporization coefficient (m.s^{-1})
H	height (m)
k	thermal conductivity (W.m^{-1}.K^{-1}) or polytropic index (-)
K	overall coefficient of heat transmission (W.m^{-2}.K^{-1})
L	length (m)
Le	Lewis number
$\boldsymbol{L_f}$	latent heat of fusion (J.kg^{-1})
$\boldsymbol{L_{sv}}$	latent heat of condensation or sublimation of water vapor (J.kg^{-1})
$\dot{\boldsymbol{m}}$	mass flow rate (kg.s^{-1})
$\boldsymbol{m}''$	mass concentration (kg.m^{-2})
$\dot{\boldsymbol{m}}''$	mass flux (kg.s^{-1}.m^{-2})
MRI	frost Mass Reduction Index
Nu	Nusselt number
p	pressure (Pa)
P	pitch (m)
Pr	Prandtl number
q	vapor quality
$\dot{\boldsymbol{Q}}$	heat transfer rate (W)
$\dot{\boldsymbol{Q}}''$	heat flux (W.m^{-2})
Re	Reynolds number
S	cross section area (m²) or tube distance (m)

$\boldsymbol{SHR}$	sensible heat ratio ($= \frac{\emptyset_S}{\emptyset_S+\emptyset_L}$)
t	time (s)
T	temperature (K)
U	heat transfer coefficient ($W.m^{-2}.K^{-1}$)
UA	sensible capacity rating ($W.K^{-1}$)
$\boldsymbol{v}$	specific volume ($m^3.kg^{-1}$)
V	velocity ($m.s^{-1}$) or volume (m^3)
$\dot{\boldsymbol{V}}$	volume flow rate ($m^3.s^{-1}$)
$\dot{\boldsymbol{W}}$	power (W)
$\boldsymbol{x}$	distance from the leading edge of the test plate (m)
$\boldsymbol{x}^*$	dimensionless position ($= \frac{x}{D_h}$)

abbreviation

CAF	constant airflow rates
FPI	fins per inch
GHG	greenhouse gas
HGD	hot gas defrosting
HVAC	heating, ventilation and air-conditioning
HP	high pressure
HT	high temperature
IIR	International Institute of Refrigeration
LP	low pressure
LT	low temperature
RH	relative humidity
TD	air refrigerant temperature difference
VAF	variable airflow rates

Greek letters

$\boldsymbol{\alpha}$	convective heat transfer coefficient ($W.m^{-2}.K^{-1}$), mass transfer coefficient ($kg.s^{-1}.m^{-2}$) or absorption coefficient (s^{-1})
$\boldsymbol{\delta}$	thickness (mm)
$\boldsymbol{\varepsilon}$	porosity
$\boldsymbol{\eta}$	efficiency
$\boldsymbol{\mu}$	diffusion resistance factor
$\boldsymbol{\rho}$	density ($kg.m^{-3}$)

τ	tortuosity factor (-) or pressure ratio (-)
ω	humidity ratio ($kg.kg^{-1}$)

Subscripts

a	air
ab	absorption
adp	apparatus dew-point
avg	average
c	cell
da	dry air
e	on
eff	effective
evap	evaporation
ext	outer
f	fin
fr	frost
F	freezer
hyd	hydraulic
ini	initial
inst	instantaneous
l	latent
L	longitudinal
m	mass
p	product
ref	refrigerant
s	sensible
sat	saturated
T	transversal
v	vapor, vaporization
w	water
wb	wet-bulb
0	dry conditions

General Introduction

The freezing and storage of products at negative temperature (below 0 °C), are very widespread in the food industry because they contribute to maintaining product quality over long periods.

During food freezing process, the temperature and humidity levels that the freezer's evaporator encounters can lead to a frost formation. When frost accumulates on coil surfaces, it gradually degrades system performance and potentially food quality. In order to limit these two effects, defrosting processes are needed to remove frost from coil surfaces. However, these defrosting operations represent an additional energy cost, product quality deteriorations and loss of productivity. Hence, both the frosting and the defrosting processes penalize the energy efficiency of the freezing system and also the food quality.

To deal with the problem of frost formation in industrial freezers, it is first essential to understand the fundamental aspects of frost formation on the exchanger. That means; to be able to predict the characteristics of frost as a function of operating conditions. However, most of the studies available in the literature have been limited to very simple geometries and/or under heat pump or cooling conditions. Moreover, the most used method of frost properties prediction is based on empirical correlations developed via experimental data. However, the reliability of such correlations would be poor and they are also limited to the range of the experimental data used to fit them. An alternative way of presenting frost characteristics on heat exchanger is through a physical/numerical model. This is the approach taken in this thesis because numerical models and simulations include the essential physics of frost growth. Numerical models are important because they can simulate a wider range of operating conditions and account for time variable operating conditions that are common in practice but often impractical in experimental research.

In order to optimize the freezing system that operates under frosting conditions, it is important to investigate and predict dynamic behavior of the overall system taking the frosting circumstances into account. In this way, it will be possible to quantify the energy and economic costs induced by these phenomena, to make decisions regarding the design of the system and its operative control. In the last few decades, many studies have been conducted on these different frosting and defrosting issues, but very few of them have placed this topic in the context of industrial food freezing. Most of them dealt with refrigeration and heat pump applications.

The primary goal of this study is to provide new knowledge about the frosting phenomenon in industrial food freezers by investigating via a numerical approach the whole freezing system behavior under frosting conditions. Then, simulations are performed to bring relevant data about the energy cost of frosting phenomenon. Sensitivity analysis of the whole process to product water losses and fan control mode are conducted. The results analysis combines both system energy performance and food quality aspects.

The present document is organized as following:

The first chapter describes briefly the general context of this thesis by highlighting the main objectives. Then a literature review of the various efforts made over the last 50 years to manage frost is reported. These efforts include that concerning frost formation process, frost growth and properties, frost effect, and defrosting technologies, by both experimental investigations and different numerical approaches. Thereafter, a particular analyze is made in order to discuss all the specificities and the related challenges but also to highlight the literature gap related to frosting in industrial food freezer.

Chapter 2 describes a numerical model of frost process based on mass and energy conservation equations. This model predicts temporal variations of frost formation rate, frost properties (e.g., thickness and density) and other relevant variables such as heat and mass flux through the frost layer. For different geometries and different physical situations, simulation results were found to agree closely with available experimental data from the literature. Thereafter, it is applied to a regressive fin pitch evaporator coil in order to analyze the industrial freezer behavior during frost growth.

Chapter 3 describes an industrial ammonia freezing system operating under frosting conditions. The chapter starts by describing the operation principle of the whole system and its nominal conditions. Then, each component is described and modeled individually. These components include evaporator, fans, compressors, receivers, valves, condenser, pumps, and the cooling tower. A methodology is proposed to take into account the heat and mass transfer between the air inside the freezer and the food product. Then, the experimental study, that has been conducted in order to quantify the influence of frost formation on the performance of the same industrial ammonia freezing system, is described. The experiment facility and the characterization measurements are presented. Finally, a comparison between the experimental data and the numerical model predictions is performed and the behavior of system is discussed.

Chapter 4 presents a sensitivity analysis of the freezing system to food water losses. Three conditions are compared and both energy performance and food quality are reported for the three amounts of moisture released by products during freezing. Then, a sensitivity analysis to fan control mode is presented. The objective is to investigate the effect of changing control strategy on the system behavior.

Finally, the conclusions from this research are presented and recommendations for future work are proposed.

CHAPTER I

Background, research motivation and literature review

CHAPTER I: Background, research motivation and literature review

I.1. Fundamentals and background

The use of refrigeration in the food sector is continually expanding to meet the needs of the population [1]. Most existing refrigerating equipment is based on vapor cycle, which implies environmental issues. Indeed, refrigeration consumes about 15% of global electrical energy consumed worldwide, and the latter is mostly produced using fossil fuels [1]. Refrigeration is the major energy-intensive process of the food chain and, in high-income countries, it is the major contributor of GHG emissions combined from energy consumption and refrigerant leakage in the postproduction food chain [2]. As promoted by IIR, reducing the energy consumption of refrigerating equipment must become a key environmental priority throughout the sector. The growth of the frozen food industry has also increased the need for new technologies to improve freezing process efficiency and reduce its cost [3].The freezing and storage of products at negative temperatures (*below 0 °C),* are very widespread in the food industry because they contribute to maintaining product quality over long periods. Since a single-stage vapor-compression refrigeration system is insufficient for these low-temperature applications, refrigeration units are usually designed in two stages or in cascade.

In food industry, two temperature categories are used to describe either frozen foods or deep-frozen food. The term frozen food is used to describe products, which are maintained at a steady temperature of -10 °C or colder. The term deep frozen food is used when the product temperature rapidly reaches -18 °C and is maintained at this temperature or colder. These products are frozen by different techniques which involve rapid and sudden freezing, exposing them intensely to temperatures from -30 °C to -196 °C, until the product core temperature reaches -18 °C. Thanks to this process, the water contained in the cells of the products is finely crystallized [4], [5]. Thus, the treated products retain their freshness, textures and flavors, keeping their essential nutrients and vitamins. The deep-freezing process requires specific equipment which may be divided into the following main groups according to the heat transfer medium [6]: direct contact (plate, band and drum freezers), air or other gaseous media (blast freezers), liquid (immersion freezers) and cryogenic medium (liquid nitrogen and solid or liquid carbon dioxide freezers).

Air-blast freezers are the most common type of food freezer in which individual product items or cardboard products are placed in a forced air stream within a cabinet or tunnel. When the

products are unpackaged, they release moisture due to the evaporation of water. Moreover, moisture can also enter into the freezer, especially from the freezer openings designed for the entry and exit of products (**Figure I.1**). To ensure freezing, air is cooled through the evaporator and pulsed onto the product by fans at high-speeds ranging from 3 m/s to 6 m/s and at a temperature ranging from -25 °C to -40 °C or less, then it is recycled to be cooled again.

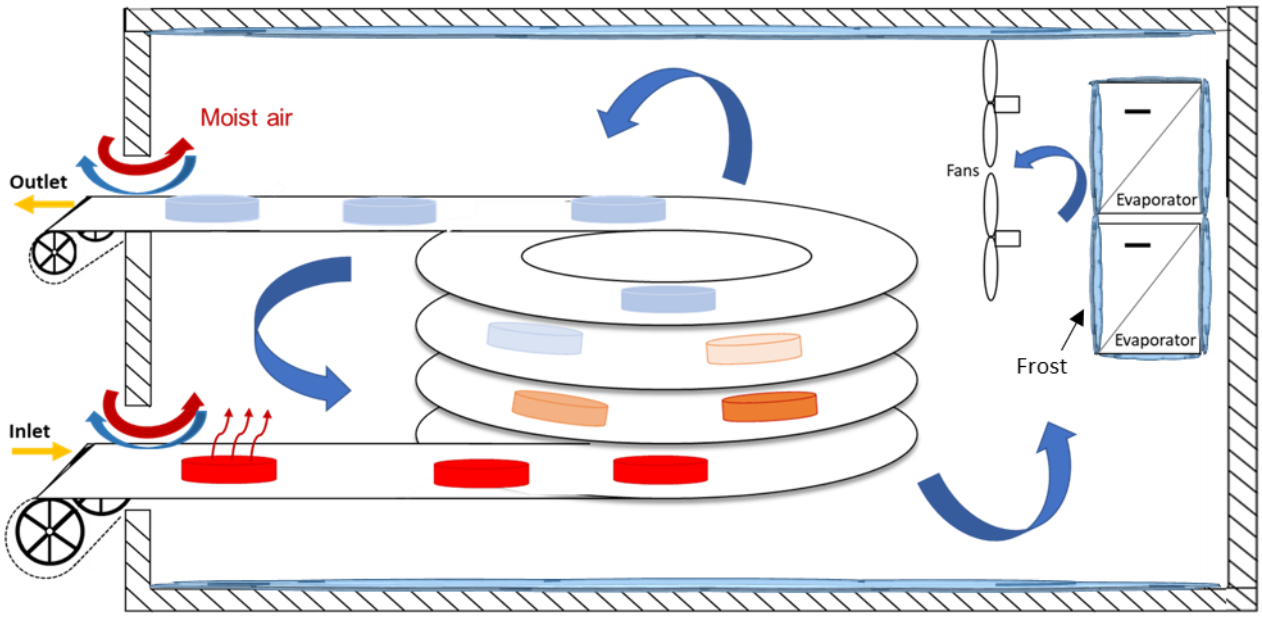

Figure I.1: Schematic of a spiral air blast freezer under frosting conditions.

The various types of these air-blast freezers include tunnel freezers, belt freezers, and fluidized bed freezers, etc. Each type is particularly suited to a specific type of product, and has its particular design, and efficiency [7] (**Figure I.2**).

Tunnel freezers are insulated rooms in which refrigerated air is circulated as closely as possible to the product placed on trays or special spacers, which stand in or pass through the tunnel in racks or trolleys one behind the other or singly. The racks or trolleys are operating with manual loading and unloading or with automated continuous operation.

Belt freezers are considered as continuous air blast freezers that use belt or conveyors for moving the product through the freezer. They are provided with a single belt, with belt positioned above each other or as a spiral belt where the products orientation changes during processing allowing uniform freezing.

Fluidized bed freezers are also continuous air blast freezer where the products are subjected to an upward air stream. They are therefore kept in flotation and frozen by the cold airflow directed from bottom to top. At an appropriate air velocity, the individual products will float each one

separated from the other but surrounded by air and free to move. In this state the mass of particles behaves like a fluid.

Each type of the air blast freezer described above has its own characteristics and operating parameters. Some of them are summarized in **Table I.1**. However, even if these freezers seem to be adequate to allow a good quick-freezing process, the food industry is constantly looking for more and more efficient systems. For that, these industrial freezers have evolved over the years. Several improvements have been done to standardize the distribution of airflow (rotating blades, baffles), to improve the insulation, to reduce the loss of mass of the products and increase the speed of freezing, to offer an optimal freezer design, to have better regulation of its components and a better control of environmental constraints [8]. Nevertheless, there is still a bit of empiricism in these developments and also there is still major problem which strongly influence the efficiency of these freezers: the formation of frost.

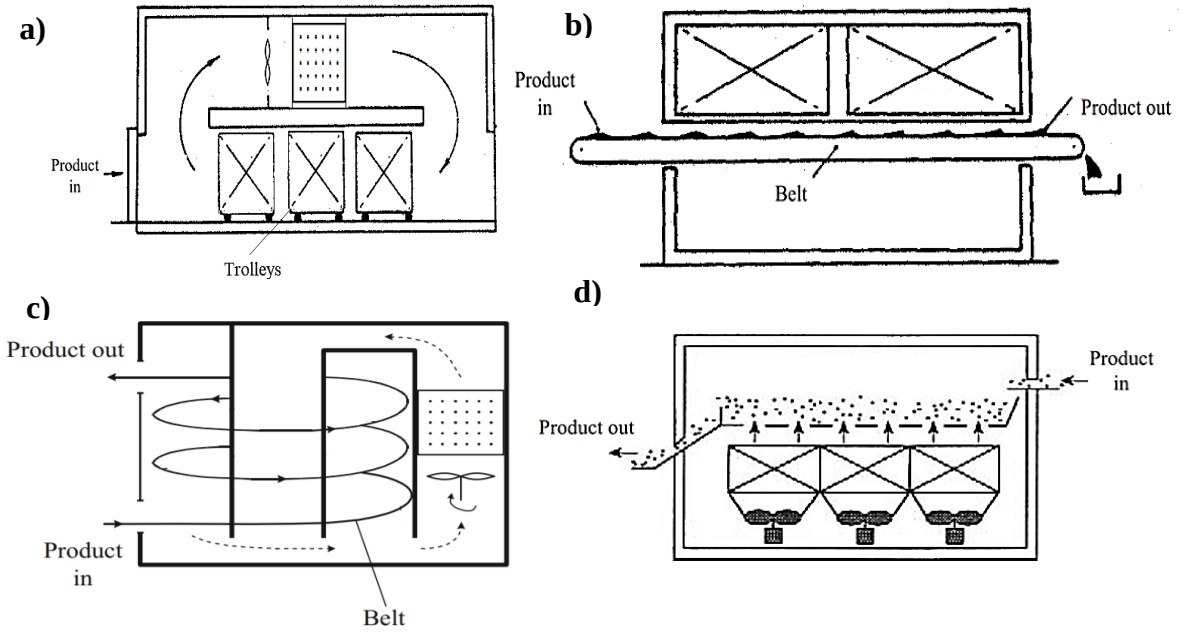

Figure I.2: Different types of air blast freezers: a) tunnel freezers, b) single belt freezer, c) spiral belt freezer, d) fluidized bed freezer.

Table I.1: Summary of air blast freezers characteristics (Adapted from [9], [10]).

Freezer type	Heat transfer coefficient ($W.m^{-2}.K^{-1}$)	Freezing time (min)	Air velocity (m/s)	Capacity (kg/h)	Product type
Tunnel (discontinuous)	<50	>180	1.5-6	1000-80000	All foods
Continuous belt freezer	<50	15-20	1.5-6	1000-20000	All foods but better for bulk items.
Spiral freezer (50-75 cm wide belt)	25-80	12-20	3-8	500-6000	Packaged or unpackaged
Fluidized bed freezer	100-160	3-4	30	1200	Small size products, 0.5 to 5 cm.

I.2. **Problem formulation**

Nearly, all the air blast freezers operate with a heat exchanger in the form of a finned tube heat exchanger. Frost formation occurs when the air is in contact with the surfaces of cold coils whose temperature is below the dew point temperature of this air and the freezing point of water.

Whatever the engineering application, this frost deposition reduces the heat transfer between the air and the outer surface of the evaporator [11], [12], decreases the airflow rate by up to 80% [13], [14], greatly reduces the refrigeration system capacity [15] and may increase its energy consumption [16]. Subsequently, the impact of this energy consumption leads to an economic impact.

To avoid these harmful consequences of frost formation, several frost management strategies and defrosting methods have been proposed and implemented [17]. Nevertheless, if these methods are not well conducted, they can penalize the efficiency of the systems used instead of improving their performance [18].

Optimizing defrost systems means adapting technologies to the type of frost formed and controlling their starting and stopping times. To do this, most researchers have focused on the formation mechanisms [19]–[21] and properties of frost [22]. Understanding the frost formation process and being able to predict the properties of the frost layer are both key elements required when proposing effective frost management solutions. The more the designers of heat

exchangers are able to predict the dynamic of frost layer growth, the more they will be able to design a system to slow frost growth as much as possible and/or minimize its impact on the energy performance of the whole unit.

An industrial deep-freezer is more sensitive to frost phenomena compared, for example, to a heat pump or a simple domestic fridge. This is due to the combination of many different factors such as: very low temperatures, numerous sources of humidity, the complex geometry of the evaporators and also many constraints that can limit the application of frost management solutions. In addition, it should be noted that food quality is another important factor that has to be considered when evaluating the harmful consequences linked to the presence of frost in an industrial agri-food freezer. Manufacturers have regulatory obligations, including that of having to keep frozen products at a temperature that does not exceed -18 °C and only small temperature fluctuations are allowed. However, important fluctuations in temperature and humidity could occur during the frosting and defrosting processes leading to the growth of microorganisms but also to a loss of product quality [23].

Finally, it should be noted that overconsumption of energy, loss of quality, and loss of productivity are not the only harmful consequences linked to the presence of frost in a food industrial freezer. In fact, frost can form on the freezer walls, on the ceiling, or on the floor and defrosting processes can sometimes cause fog formation inside the refrigerated space. And these are all factors that constitute a veritable risk to goods and people security.

Frost management is therefore a major concern for all the frozen food manufacturers. However, few works have investigated this problem in industrial freezing conditions and at the overall system level.

It is to note that in the rest of manuscript, the term freezing conditions means the industrial food deep-freezing state coupling very low air and evaporation temperatures with high air velocity.

I.3. **Research motivations and objectives**

The main objective of this thesis is to bring new knowledge about the frosting phenomenon in industrial freezing conditions that are: very low temperatures, high air humidity and velocity, and complex geometries (finned tube). This investigation allows to study the influence of frost on the performance of the evaporator. It is then essential to study the behavior of the entire system in order to quantify the effects of frost on a global scale. From this knowledge, it is

possible to limit the harmful effects described above by acting in different ways while respecting industrial constraints of productivity and food quality.

In order to reach the main goal of this thesis, the following sub-objectives are pursued:

***Development of a dynamic frost growth model on a heat exchanger operating under quick freezing conditions*:** in order to understand the kinetics of frost formation and its impact on the heat exchanger operation. This model is developed in Dymola software using the Modelica language and introduced into the basic model of the heat exchanger which already exists in the library of thermal systems (TIL) used during this thesis. The model is adapted to take into account all physical phenomena. It is then used to treat the dynamics of frosting and the behavior of the exchanger under these conditions. This tool could be helpful for energy system manufacturers to make decision in the design and control of their installations.

Modeling of an industrial ammonia freezing system operating under frosting conditions: this model is built on real data from a food industrial plant. This second objective aims at modeling each component of the system in order to create the closest configuration to that of the real one as well as all other configurations encounterable in the food industry. The model is then used to quantify all the damage caused by the frost but also to monitor and analyze the behavior of the whole system under these conditions. This kind of system-level analysis provides a lot of information. On the one hand, it provides relevant data on energy, and quality costs due to frosting. On the other hand, it helps to identify potential sources and possible ways of improvements. One of the features and originality of this work is that it takes into consideration the presence and the quality of food in the numerical model. The results also focus on the food quality degradation during frost growth and emphasize both energetic and qualitative indicators.

Recommendation and identification of different potential sources of improvement: the prediction of frost properties over time as well as the behavior of each component under frosting conditions allows the identification on several ways of improvement (fan mode, compressor mode, heat exchanger design, initial inlet product temperature, etc.) based on various constraints or industrial goals (energy performance, production time extension, food quality preservation…).

I.4. **Literature Review**

This literature review section is divided on three main sub-sections. First, a synthetic database is proposed to know how the literature deals with frost issues in industrial freezing processes. In the second sub-section, the frosting process is explained, focusing on the studies that have been carried out to examine the properties of frost and its growth under different conditions and for different applications. The third sub-section is devoted to studies related to frost thermal and hydraulic effects. The last sub-section is devoted to studies aimed at managing the problem of frost. At the end of each section, and by combining elements from the literature with the author's knowledge, the particularities of the deep-freezing process are pointed out.

I.4-1. Preliminary overview of research on industrial freezing conditions

Based on the existing literature from the 1957 to 2020, a database of around 130 papers has been generated in order to categorize the studies carried out under freezing conditions and on an industrial scale compared to those carried out under other conditions (heat pump, HVAC, Cryogenic, etc.) and at other scales (laboratory, domestic, etc.).

In the framework of the objective of this review section, the literature that reports frosting and defrosting research in any conditions or applied to any field was selected. Then, the appropriate literature was classified by year of publication. Next, the literature was classified by:

- Type of studies: experimental or numerical/ theoretical;
- Type of geometry: simple geometry (flat plate, cylinder, parallel plates, vertical plate) or complex geometry (finned-tube, microchannel, etc.);
- Range of wall temperature and air inlet temperature;
- Range of air inlet velocity;
- Fan control mode: constant airflow CAF (variable fan speed) or variable airflow VAF according to fan curve.

Despite the clear progress made with the number of theoretical and numerical studies (**Figure I.3**), experimental studies remain predominant and make up about 60% of the total studies. Different experimental configurations ranging from laboratory apparatus to industrial evaporators led to better understanding of many aspects of the phenomena involved. However, there are still some challenges and progress to be made relating to some specific measurements (frost thickness, mass, distribution) and on data acquisition [24]. The lack of numerical studies, especially in the 20^{th} century, may be explained by the complexity of the phenomena, which

are non-linear, transient and need appropriate coupling of heat and mass transfer models with a wide range of boundary conditions. With the progress achieved in numerical tools, efforts have been made in recent years to take into account the maximum physical phenomena in modeling, adopt several approaches [25] and model complex geometries.

The type of surfaces that have been studied is shared almost equally between the simple surfaces and the complex surfaces of heat exchangers. However, in the latest review [22] reporting the literature up to around 2010, the authors noted that most studies were focused on flat plate surfaces which are more basic. This shows that during the last decade the heat exchangers have received more interest.

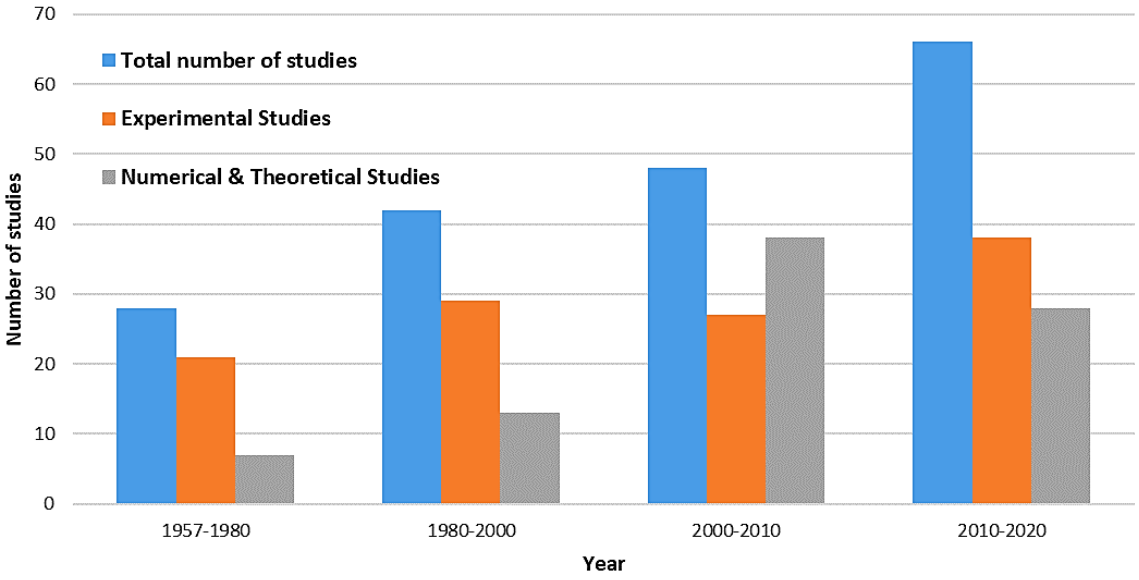

Figure I.3: Distribution of numerical and experimental works on frosting and defrosting published from 1957 to 2020.

Figure I.4 (a) and **Figure I.4 (b)** clearly point out that, in the literature, the wall temperature and the air temperature mostly range between -15 to -5 °C and 0 to 20 °C, respectively. It confirms that most of the applications studied target heat pump applications.

It should be noted that low wall temperatures are not neglected in the same way as in recent decades. Recently, frost properties, the thermo-hydraulic behavior of the heat exchanger and defrosting have been investigated at temperatures below -30 °C. However, these wall temperatures have always been coupled to high air inlet temperatures in order to enrich the input data to understand the dynamics of frost. Nevertheless, they are not representative of real food freezing conditions.

By categorizing studies by range of air velocity (**Figure I.5**), it can be seen that around 60% of the total studies focused on low velocity < 2 m/s whereas only 24% of them focused on higher air velocities (> 3 m/s) such as encountered in industrial freezers.

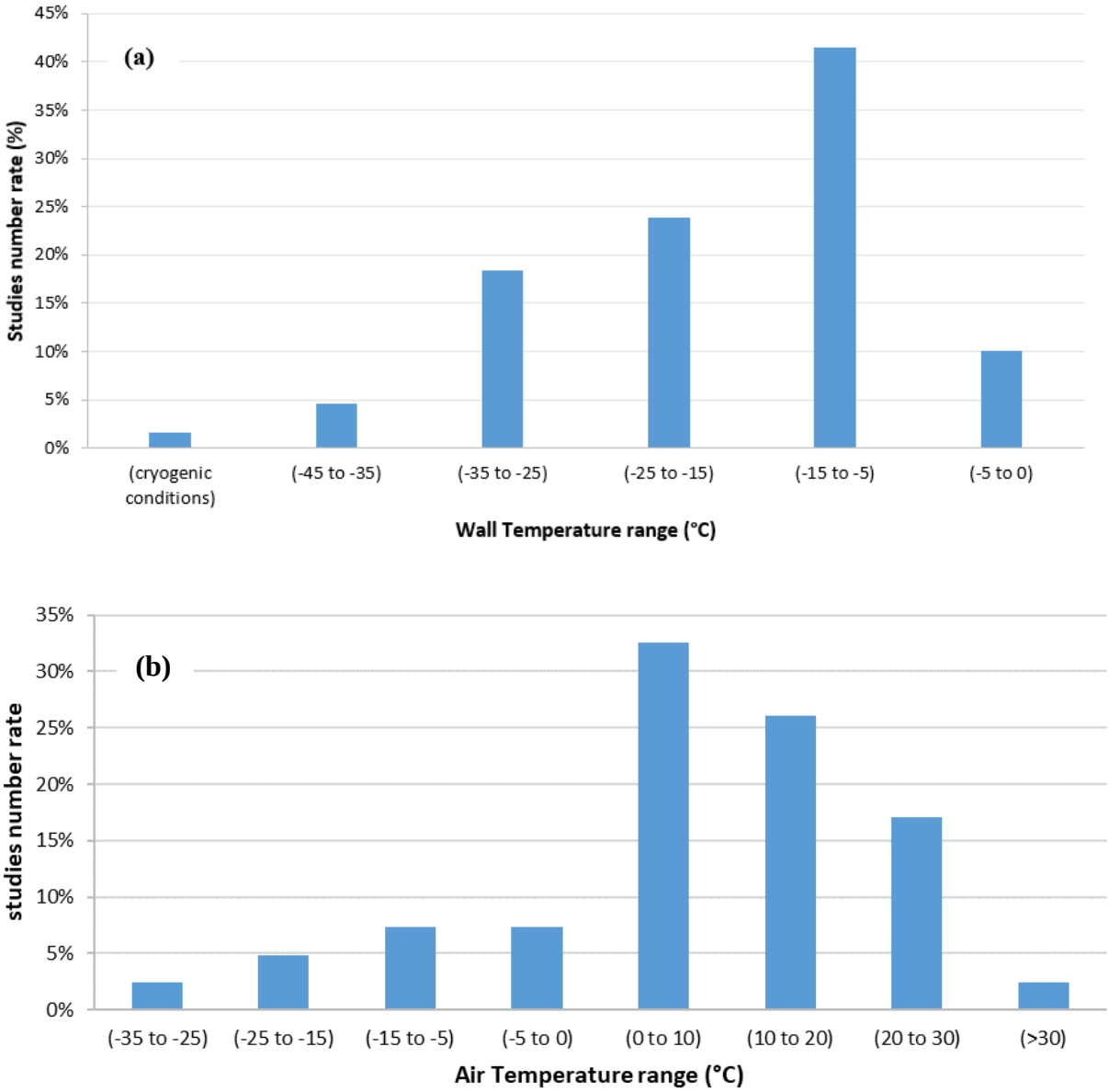

Figure I.4: Data analysis of Frosting/Defrosting studies (numerical and experimental) – (a) Wall Temperature range (b) Air Temperature range.

To better examine the presence of freezing conditions in the frosting and defrosting literature, we selected only the studies that satisfy three conditions at the same time. These are: low wall temperature (<-30 °C), low air temperature, and high air velocity (> 2 m/s). Doing this, some typical studies from the 1957 to 2020 and their operational geometries, temperature ranges, and air velocities are listed in **Table I.2**; the data from the table are illustrated in **Figure I.6.** As illustrated in **Figure I.6**, only 13% of all the research has been performed in freezing conditions,

with simple and complex geometries. Adding complex geometry as the fourth condition, only 5% of total research has investigated a whole heat exchanger in freezing conditions. Despite the major challenges involved in controlling frost during deep freezing conditions, these figures indicate that the literature is rather poor in this area, therefore encouraging investigation.

In addition, almost all industrial freezing systems are equipped with a fixed-speed motor driven fan coil unit. But, the behavior of frost and its effects on evaporator thermal hydraulic performance will not be the same when operating with a variable fan speed to maintain a constant airflow [26]. Therefore, we have classified the literature by fan control mode. More than 80% of the studies were carried out at constant airflow (variable fan speed). Nonetheless, most of the studies, especially those using models, did not consider the decrease in airflow that actually takes place in fan-supplied evaporators under frost conditions, which is one of the primary causes of cooling capacity reduction. Indeed, this condition of constant fan speed has been added to the selection criteria of industrial freezing conditions. Since to the authors knowledge, only one existing study [27] has been carried out on the large air cooling evaporator coils typically used in an industrial ammonia freezing system operating under low air and refrigerant temperature conditions with a finned tube heat exchanger and high air velocity.

However, this study does not enrich the literature with complete data on the occurrence of frost under these conditions.

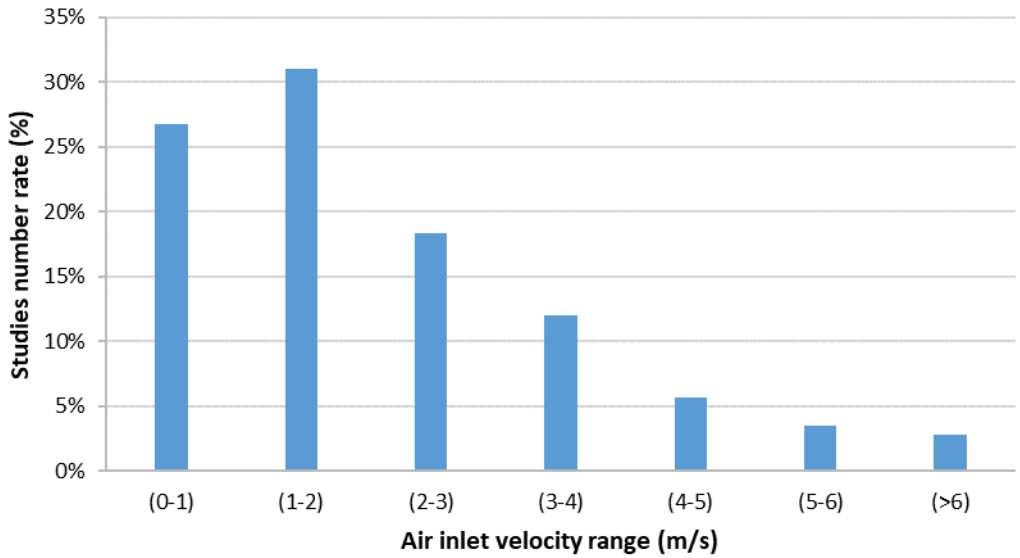

Figure I.5: Data analysis of Frosting/Defrosting studies (Numerical and Experimental) – Air velocity.

Table I.2: Experimental and numerical studies of frosting/defrosting under freezing conditions.

Year	Scholars	Approach	Geometry	T_a (°C)	T_{wall} (°C)	V_{air} (m/s)	Fan mode
1967	Lotz et al. [28]	Experimental	Finned tube	-20 to 0	-30	2.5	Constant
1989	Patin et al. [29]	Theoretical	-	-26	-30	-	-
1999	Chen et al. [30]	Numerical	Finned tube	-21 to -13	-41 to -31	4.4	Constant
1999	Mao et al. [31]	Numerical and Experimental	Flat plat	-10 to -26	-20 to -41	1 to 4	Constant
2000	Chen et al. [32]	Numerical	Flat plate	-21 to -13	-41 to -31	2	Constant
2001	Sherif et al. [33]	Experimental	Finned tube	-8.3	-40	3.81	-
2002	Verma et al. [34]	Numerical and Experimental	Finned tube	-20	-30	2.2	Constant
2004	Aljuwayhel et al. [35]	Experimental	Finned tube	-27	-34.5	3	Variable
2004	Seker et al. [36]	Numerical	Finned tube	-20	-35	3	Constant
2004	Seker et al. [37]	Experimental	Finned tube	-20	-35	3	Constant
2007	Aljuwayhel et al. [38]	Numerical	Finned tube	-27	-34.5	3	Variable
2008	Piucco et al. [39]	Numerical and Experimental	Flat plate	-20 to 30	-30 to 0	0.7 to 2	Constant
2009	Hermes et al. [40]	Experimental	Flat plate	-20 to 30	-30 to 0	0.7 to 2	Constant
2009	Cao et al. [41]	Numerical	Flat plate	-24	-39.22	1 to 4	Constant
2012	Wang et al. [42]	Numerical and Experimental	Flat plate	-8 to 19	-30 to 0	0.5 to 5	Constant
2018	Kumala et al. [43]	Experimental	Finned tube	-20	-40	-	-
2020	Badri et al. [44]	Numerical	Finned tube	-30	-35	3.6	Variable

I.4-2. Frost formation process, frost growth and frost properties

Frost formation has received varying degrees of attention over the last 50 years. A large number of experimental, theoretical and numerical investigations have been reported relative to frost formation mechanisms, frost growth and frost properties. The different stages involved are studied sequentially to understand the whole frosting process and the factors affecting this

phenomenon. Moreover, numerical models and empirical correlations have been proposed to predict frost properties in order to develop effective defrosting and anti-frosting technologies.

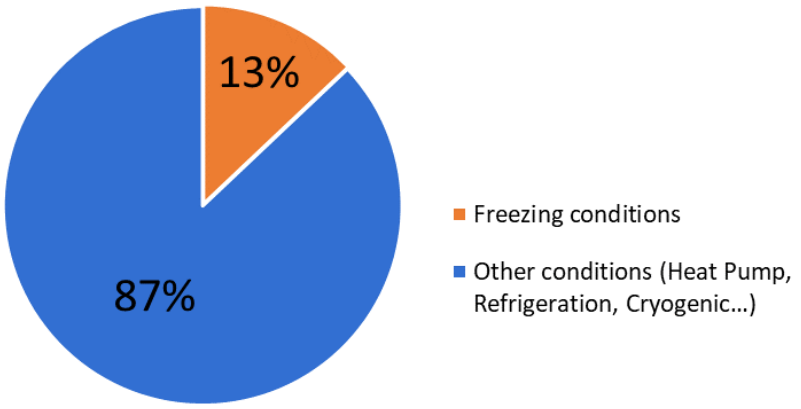

Figure I.6: Data analysis of Frosting/Defrosting studies (Numerical and Experimental) – Operating Conditions.

A. Frost formation process

Whatever the use of the heat exchanger, the two main factors that provoke frost formation on its surface are humidity and temperature. The difference resides in the transformation mechanism of the vapor contained in the air into ice crystals and the way it is deposited on the cold coils of the heat exchanger. Two studies by Hermes et al. [39], [40] investigated frost formation on a cold plate and found that two types of transformations can occur:

- Either the vapor condenses in contact with the cold wall if the surface temperature is below the dew-point but higher than the triple point of water. Then, the droplets formed can freeze if the temperature of the surface decreases to 0 °C.
- Or the vapor turns directly into ice crystals (desublimation) in the case where the temperature of the surface and the dew-point are both lower than the triple point of the water.

Brian et al. [45] discussed another mechanism of frost formation. The air water vapor may freeze in the air without any contact with a wall, thus forming a fog, before being deposited on the different cold surfaces in the freezer. These researchers explained that this phenomenon is due to the large temperature difference between the bulk air and the evaporator walls. The properties of the frost formed under these conditions are different from those of the frost formed by the two mechanisms described previously. This phenomenon will be discussed in more detail in **section I.4-2**.

Moreover, as the way frost occurs on the plate can significantly influence its growth, some researchers have focused in particular on the analysis of the aspect of the ice crystals formed as a function of the air humidity and the temperature of the cold surface. Kobayashi [46] proposed a map of the different shapes of ice crystals formed under different temperature and super-saturation degree conditions. Qu et al. [47] took this idea further by adding that the shape of crystals subsequently influences the growth rate in the early stage of frost formation.

In **Figure I.7**, a graph proposed by Wu et al. [48] shows the initial frost crystals classified into five groups according to their occurrence and shape. As mentioned by Kobayashi [46], the appearance of crystals is not identical, reinforcing the idea that there is a relationship between crystal morphologies, the temperature of the cold plate and air humidity. We highlight that, using microscopy, some authors have observed that the shape of ice crystals is primordially affected by surface temperature and less affected by relative humidity. Nevertheless, it should be noted that their experiments were carried out on surfaces ranging from -20 to 0 °C and in air at 22 °C. This means that at much lower temperatures the appearance of the crystals may be different, likewise for the effects of temperature and humidity.

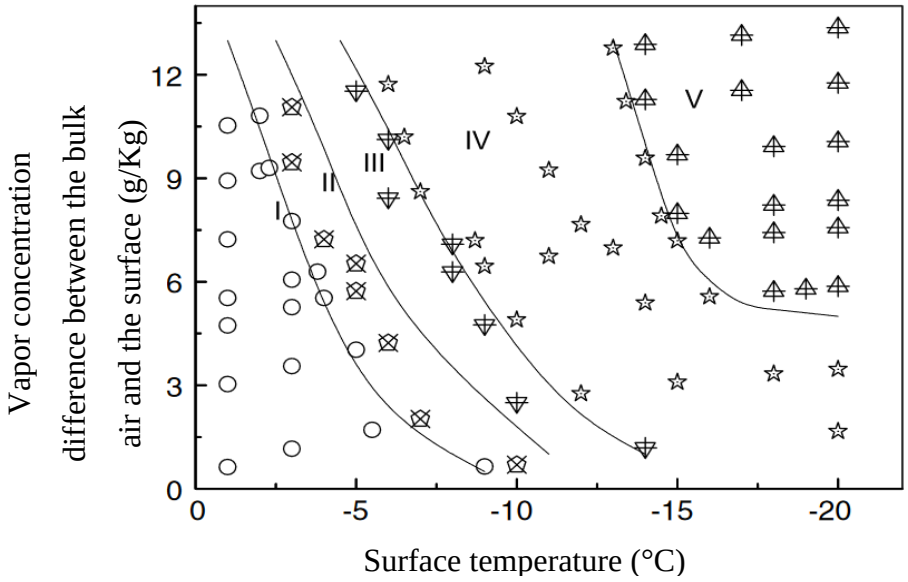

Figure I.7: Effect of surface temperature and air humidity on the shape of the earliest ice crystals; I: super-cooled water droplets, II: irregular crystals, III: flake crystals, IV: needle and pole crystals, V: feather crystals [48].

Some researchers have studied frost formation on other different geometries. The studies of Lee et al. [49] on a vertical plate, Tajima et al. [50] on a vertical plate air cooler, Cremer and Mehra [51] on a cylinder, and Han and Ro. [52] on parallel plates, have all enhanced the previous results relating to frost formation mechanisms. Moreover, these authors added that frost can be

formed even under low humidity with a dew point below 0 °C. Their results are in agreement with those of Wu et al. [48]. According to these authors [52], the location where the frost properties are measured is an important factor to take into account during studies of frost formation mechanisms in complex geometries and especially for a finned tube geometry which is more disadvantageous regarding this aspect. Frost distribution is not homogeneous and therefore measuring frost properties in one location cannot always be representative of what happening in the whole geometry.

Leoni [53] reinforced this idea and estimated that it is easier to study or visualize the frost formation process on flat plates microscopically and determine the key parameters involved in it. Other geometries were more difficult to study; this is due to several constraints, mainly the uniformity and the distribution of frost on these types of geometry as well as the difficulty of carrying out measurements on these evaporators.

B. Frost growth and properties

Frost growth is a complex process because of the characteristics of frost change depending on several environmental and technical parameters; they are also influenced by time and history during process. Nevertheless, Hayashi et al. [54] demonstrated that the process itself, independently of frost properties, can be considered as a common process that can be divided generally into three periods:

- Crystal growth period: at this stage, frost crystals form on the cold surface and, as they are generally distant from each other, they begin to develop vertically. This period can be considered as one-dimensional growth.
- Frost layer growth period: branches are generated around the top of the crystals so they interact with each other, forming a more uniform layer where the growth becomes more three-dimensional.
- Full growth of the frost layer: at this level, the crystals stop changing size and shape, the frost layer becomes flatter, then the surface begins to melt allowing the condensed water to diffuse inside the frost layer, thereby increasing its density. Then the deposition of frost begins again and the cycle; melting, freezing, deposition continues.

Several ***experimental studies*** have been performed to understand how frost dynamics vary the major parameters affecting frost growth on a heat exchanger surface; these parameters appear to be air humidity and velocity, plate temperature, the location on the heat exchanger, and the location of the heat exchanger itself. Some experimental studies have led to the proposal of

empirical relationships that can be used to predict the thickness of frost, its density and its thermal conductivity as a function of several parameters. These correlations will be discussed in the next paragraphs.

All the studies that have been conducted on flat plates [55], parallel plates and cylinders [56], microchannel [57] and finned tube heat exchangers [58], agree that the frost thickness increases as the humidity of the air increases and the temperature of the cold surface decreases. A large temperature difference between the air stream and the plate surface, and high air humidity respectively allow increasing of the mass transfer flow and raise the driving force of deposition, thus accelerating frost thickening. However, experimentally, the effect of air inlet velocity has revealed a considerable contradiction in the literature regarding the dependency of frost thickness on air velocity [59].

Based on experimental measurement of frost thickness on a cooled cylindrical tube at -25 °C, Schneider [60] found that varying the air velocity from 1.2 to 10 m/s has no effect on the frost thickness. Schneider suggested a correlation to predict the frost thickness depending on time and the temperature difference between frost surface and cooled wall excluding the air velocity. In contrast, results from Hosoda et al. [12], and Barzanoni et al. [61], showed a great dependence between the frost thickness and air velocity. According to them, increasing the air velocity increases the frost thickness.

Lee and Ro [49] experimentally examined the effect of operating conditions on the growth of frost on a vertical aluminum plate. Lee and Ro found that the effect of velocity is minor compared to that of air humidity and of cooling surface temperature on frost thickness. At -15 °C wall temperature, 15 °C air temperature, the frost thickness seems to increase slightly from 3 to 3.2 mm for Reynolds number (Re_x) ranging from 1,000 to 2,000, respectively.

Recently, Leoni et al. [53] made a test bench to propose new data on frost formation on a flat plate exposed to a humid airflow inside a closed-loop wind-tunnel. At -14.3 °C wall temperature, 12 °C air temperature, and an air relative humidity of 80 % and by varying the air velocity from 2 m/s to 4 m/s; frost seems a little bit thicker at low air velocity. In **Table I.3**, the three evaluations of the relationship between frost thickness and air velocity and their interpretations are grouped together.

Table I.3: Frost thickness and air velocity relationship interpretation in the literature.

Frost thickness and air velocity relationship	**Independent**	**Proportional**	**Inversely proportional**
Interpretation	Both total and densification mass fluxes increase with velocity, thus, the mass growth flux remains constant	A low air velocity means a small amount of vapor transferred into the frost layer from the moist air and therefore a thin frost layer	At high air velocity, the high convective exchange coefficient heat the frost surface and thus favor the diffusion of steam inside the frost layer decreasing its thickness.

O'Neal and Tree [62] explained this contradiction by showing the existence of a critical Reynolds number (Re_x) of approximately 13,000 above which frost growth on a flat plate is independent. This conclusion was confirmed experimentally by Lee et al [63]. The latter investigated the effect of varying the operating conditions on frost thickness and noticed that there is a little difference in frost thickness if the inlet air velocity is over 2 m/s ($Re_x > 1{,}000$).

In the same way, the variation of frost density has been deeply analyzed experimentally. A parametric study of the literature data of a flat plate performed by Leoni et al. [59], showed that the increase of the Reynolds number causes the densification of the frost layer. When the air velocity is high, mass and heat transfers increase, leaving less space for air in the porous layer [40]. In addition, high wall temperatures favor frost densification; the mass flow that contributes to the increase in the layer mass is higher than that contributing to the increase in thickness [64].

As for humidity, its effect on frost density remains to be clarified because some disagreements continue in the literature [53]. On the one hand, Hermes et al. [40] investigated experimentally the frost densification on a flat surface (100 mm × 100 mm) cooled at -15 °C by a thermoelectric cooling device including the aluminum plate cold side and an air source heat exchanger on the hot-side. The plate was exposed to an airflow at 22 °C that was driven by an axial fan at velocity of 0.7 m/s. Hermes et al. [40] noticed that two hours after starting the test, the frost density was 2 times higher at an air relative humidity of 80% compared to 50%. On other hand, frost growth experiments were conducted by Wang et al. [42] on a cold flat plate (40 mm × 40 mm) under various frosting conditions. By maintaining constant the air temperature at 0 °C, the plate temperature at -16 °C, and the air velocity at 5 m/s; the average frost density after one hour was

around 200, 250 and 220 kg/m^3 for air relative humidity of at 42%, 53% and 72%, respectively. This means that the frost density was higher for intermediate relative humidity.

Lee et al. [65] performed an experimental study on the effect of air temperature, air humidity, and air velocity on frost growth on a finned-tube heat exchanger. They found that increasing the air inlet relative humidity leads to a thicker frost layer with a lower frost density and thus a higher thermal resistance. Increasing the air velocity leads to a reduction in frost thermal resistance, an increase in frost thickness, and an increase in frost density. Increasing the inlet air temperature results in a reduction of frost thickness, an increase in frost density, and a decrease of thermal resistance. It should be noted that the relative humidity was not held constant during some tests. As a result, the conclusions of this parametric study were likely inconclusive. Recently, experiments were carried out by Liping et al. [66] to investigate the effect of ambient conditions on the frost growth characteristics on a single row fin-tube heat exchanger. The experiments were conducted in a psychometric room where the air temperature and relative humidity were controlled to vary between -3 °C and 0 °C and between 65% and 85%, respectively. All their results were consistent with those of Lee et al [65]. Liping et al. [66] also added that for their cases, the effect of air inlet velocity on frost thickness was very low.

It seems difficult to decide and generalize the effect of each independent parameter on the complex frost growth and densification phenomena. It depends on several competitive parameters.

Theoretical and numerical studies have been also conducted to clearly understand frost growth dynamics. Three main categories of frost models exist in the literature:

Models based on empirical correlations: They aim at predicting frost characteristics, mainly frost thickness, density and thermal conductivity [22] over time and as a function of operating conditions. However, these models are specific to a particular case and the operating conditions used for their development. They are not always applicable in other operating conditions and different contexts. An interesting recent review [22] listed the frost layer properties (thickness, density, and thermal conductivity), heat transfer and mass transfer correlations that have been investigated from 1970. Under freezer operating conditions, and according to the author's knowledge, only one correlation developed by Mao et al. [31] has been able to predict frost properties for low wall and air temperatures (ranging from -41 °C to -31 °C and from -26 °C to -10 °C, respectively), high air humidity (ranging from 65% to 96%) and large air velocity intervals (1 m/s to 4 m/s). Based on an experimental investigation of frost growth on a cold

plate, the authors survey the frost characteristics variation over a large surface (600 mm × 200 mm) using special measurement techniques. The laser beam method was used to measure the frost height and many removable disks flush mounted in the cold base plate permitted the measurement of frost mass concentration. Twenty tests were done for steady operating conditions; each were run for two hours. Depending on the cold plate temperature and the relative humidity of the supply air, Mao et al. [31] found that the frost could appear either smooth or rough. Depending on these two parameters, the authors suggested a map showing the frost surface characteristics. Doing this, they propose three groups of correlations. Ones for the rough frost surface, ones for the smooth surface, and more general correlations for both of them. In each correlation, frost characteristics were correlated as a function of five independent variables expressed as follow:

$$\boldsymbol{m''_{fr}, \delta_{fr}, \rho_{fr}, k_{fr} = A_1\ (x^*)^A(\omega)^B(T^*)^C Re_d^D F_o{}^E} \qquad \textbf{(Eq. I.1)}$$

Where x^* is the ratio of the distance from the leading edge and the inlet hydraulic diameter, ω is the inlet air humidity ratio, T^* is a cold plate temperature ratio, Re_d is the Reynolds number based on the hydraulic diameter d, F_o is Fourier number and A_1, A, B, C, D and E are constants. These correlations are available for the operating conditions that are typical of many industrial and commercial freezers. **Table I.4** summarizes the resultant correlations classified on each frost surface type.

Table I.4: Correlations of Rough and Smooth frost surface for frost properties under freezer operating conditions [31].

Frost properties	**Frost surface**	**Intercept and Exponents**					
		A_1	A	B	C	D	E
Density $\boldsymbol{\rho_{fr}}$ (kg/m^3)	Smooth	1.334×10^4	-0.048	0.506	1.371	-0.435	0.318
	Rough	1.601×10^{-1}	-0.056	-0.011	0.845	0.463	0.217
	Both	0.955×10^3	-0.053	0.317	1.130	-0.279	0.328
Thickness $\boldsymbol{\delta_{fr}}$ (m)	Smooth	1.908×10^{-8}	-0.102	0.123	-2.034	1.054	0.885
	Rough	9.183×10^{-5}	-0.085	0.400	-1.712	0.449	0.699

	Both	1.989×10^{-8}	-0.092	0.203	-1.971	1.220	0.663
Mass concentration $\boldsymbol{m''_{fr}}$ (kg/m^2)	Smooth	2.748×10^{-4}	-0.151	0.635	-0.645	0.612	1.209
	Rough	1.462×10^{-5}	-0.140	0.389	-0.867	0.913	0.917
	Both	1.917×10^{-5}	-0.146	0.524	-0.836	0.943	0.993
Thermal conductivity $\boldsymbol{k_{fr}}$ (W/m.K)	Smooth	0.266×10	-0.043	0.444	1.204	-0.400	0.246
	Rough	1.633×10^{-3}	-0.048	0.004	0.737	0.357	0.180
	Both	0.2752×10^{2}	-0.046	0.283	0.984	-0.275	0.273

Computational Fluid Dynamics CFD based models have been developed mainly to accurately predict detailed phenomena like the frost layer structure and the distribution of absolute humidity inside the frost layer [67]–[71]. These models can be used to predict and simulate the macroscopic behavior of the frost layer. Computational fluid dynamics method could be classified intro three categories. The first type does not take into account the airflow side, focusing only on frost. The heat and mass transfer from the air to the frost region are then calculated using empirical correlations assuming either the humid air near to the frost surface was saturated [63], [72] or supersaturated [73], [74].

The second group uses models based on Eulerian multi-phase representation and they considered two phases: the primary one is gas (air side), and secondary one is ice. Such dual phases had been widely used recently. Many researchers have successfully calculated the frost properties by solving governing equations in both sides and by using matching conditions to balance the energy and mass flows between the domains. Lee et al. [75] developed a CFD based model including partial differential equations for the boundary layer in order to consider the airflow variation during frost formation. Their model was successfully validated against experimental data conducted on a cold plate at temperature of -15 °C with laminar and turbulent flow [71], [76]. Lenic et al. [77] developed a transient two-dimensional model defining governing equations of air, frost sub-domain and the air-frost interface. The developed model was validated by experimental measurements carried out on a flat plate at a temperature of -19.5 °C and for different inlet air temperatures and relative humidity in the range 19-23 °C and 37-60%, respectively. Thereafter, numerical analyses have been performed and enabled the prediction of the exchanged heat flux degradation in a heat exchanger under the frost growth

conditions [78]. Recently, a CFD based three dimensional model has been developed [79] including the fin, the two airflow passages (over and under the fin), and an inlet and outlet section in the computational region. Implementing the model in FLUENT®, the numerical results show the frost distribution on a finned tube heat exchanger, the temperature distribution and the airflow pressure drop. The simulation conditions were -5 °C as an initial wall temperature, and 2 °C, 80% and 1 m/s as air inlet temperature, relative humidity and velocity, respectively. After 50 min of frosting, the frost appeared to be thicker and denser on the windward side of the heat exchanger and the pressure drop was practically doubled.

In contrast to these approaches, the third category of models uses the same Eulerian method but solves the governing equations in a single domain [80]. Kim et al. [69] used CFD to propose a new water vapor mass transfer rate by modifying Sauter mean diameter (defined as the ratio of the frost surface area and the volume of the frost layer) and validated the model against experimental data of Lee et al. [75]. Compared to existing models, a model was provided by Kim et al. [69] where the two assumptions related to initial frost thickness and density were eliminated. Cui et al. [68] proposed frosting mass transfer model based on the theory of nucleation and they focus not only on the frost behavior but also on the macroscopic description of the initial period of frost formation on a cold plate. Doing this, Cui et al. [67] improved this model by taking into consideration the influence of surface structure and they simulate the performance of finned tube heat exchanger under frost conditions.

In fact, under freezing conditions where the surface temperature is very low, the frost formed is highly porous. It means that two quantities of water vapor diffused inside the frost layer should be considered. The first one diffuse from the frost layer surface. The second one penetrates directly from the airflow through the spaces occupied by air inside the frost layer. However, as illustrated in **Figure I.8**, in CFD based model, the air volume inside the frost layer

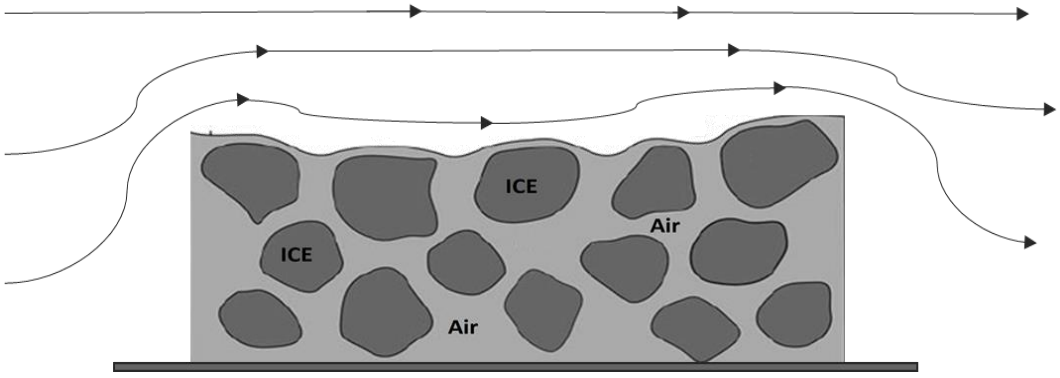

Figure I.8: Airflow in a CFD Simulation when a highly porous frost is formed, adapted from [81].

could be recognized as frost and the airflow into these spaces may be blocked. Such limitations have been reported in detail by Lee et al. [81], pointing out that CFD approach is still restricted to the analysis of these kind of local phenomena. Moreover, the CFD based models require a long time since a huge number of complex calculations is processed. Their application for large size industrial geometry is still not up to date.

Finally, the main approach is to develop models based on heat and mass diffusion through the frost layer considered as a porous medium [63], [72], [73], [82], [83]. These models are a good compromise between the physical phenomena taken into account and their simplicity of use for simulation. All the models based on heat and mass diffusion through the frost layer use the same set of basic equations. However, in addition to this basic set, the authors considered many different assumptions. In order to make the numerical modeling more tractable, the physical models in the literature adopt the same assumption that the water vapor transported onto the frost surface from the air stream consists of two parts. Part of this water vapor directly diffuses into the frost layer and solidifies the frost, while the remainder deposits on the frost surface and increases the frost thickness.

Since the frost growth period is of primary interest, especially for a system scale analysis, quasi-steady state models are more favorable and more widely used than fully transient models. Admittedly, fully transient models of frost are very interesting since they can take into account the early stage of frost formation and the spatial variation in temperature and density within the frost layer. However, fully transient models are too computationally expensive; also, the early stage of frost formation is thought to be of secondary interest, especially in a dynamic system modeling approach [25]. **Figure I.9** shows a diagram of all the zones and phenomena considered in the frost models. Three zones are considered: the air-stream with convective heat and mass transfer, the frost layer with heat and mass diffusion, and the interface between the two zones at the frost surface.

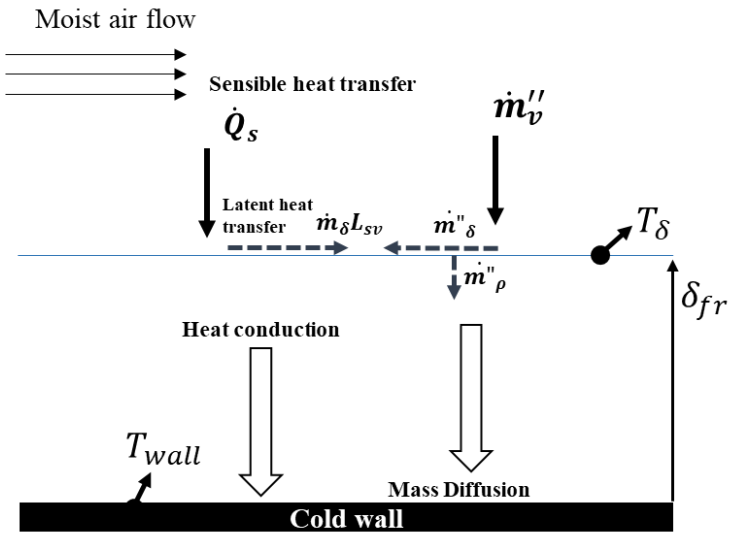

Figure I.9: Transport phenomena in a porous frost layer.

Indeed, in the quasi-steady model of frost accumulation, frost growth is handled by different approaches regarding:

- The water vapor diffusion inside the frost layer. Either to assume that the water vapor desublimation rate is constant within the frost layer [84]–[87], i.e. frost has a flat density profile in the perpendicular direction, so the porosity of the frost layer is uniform within the frost layer, or to consider it as proportional to the water vapor density [63], [70], [88];
- The water vapor saturation at the air-frost interface [64], [73];
- The frost thermal conductivity. This frost property is calculated by empirical correlations proposed in the literature. Most of them correlate the thermal conductivity to the frost density but predict a large discrepancy in thermal conductivity especially for low densities [89];
- And the initial conditions (initial frost density and thickness) [72].

All these approaches have been analyzed and compared to experimental results by Nemer et al [89]. Thereafter, and through simplification, the temperature distribution within the frost layer can be determined analytically; also, frost thickness and density at each time step are determined. Since these models do not take into consideration the nucleation process, the equations require initial conditions of frost density and frost thickness. These conditions must be chosen carefully because they have had major impacts on many results in the literature [89]. Incidentally, $\delta_{fr,ini} = 10^{-6}\ m$ and $\rho_{fr,ini} = 30\ kg/m^3$ is the most basic and common values adopted in the literature.

Most of these modeling studies aimed to examine the effect of frost on the evaporator and not the dependence of frost growth on operating conditions. The few models used in these parametric studies have found roughly the same trends as the experimental ones described below and they have also found the same contradictions [36], [90].

C. Industrial freezing specificity

When examining frosting, the main problem in an industrial freezer is to identify how much humidity there is inside it. In other words, it is difficult to identify the moisture sources and the humidity that they lead to. These particularities make this kind of industrial application specific in comparison to heat pump or domestic refrigeration, for example.

The interest of knowing the sources of humidity in an industrial freezer lies in the need to control the level of undesirable humidity that is then transformed in frost.

The main common source of moisture is products, especially when they are not packaged. In such cases, freezing induces water loss up to 6% according to the product and the freezing process [91]. The loss of water from food during the freezing process occurs because the vapor pressure of water (or ice) at the surface of food is greater than the vapor pressure of water in the air [92]. So, the water molecules migrate from the product to the coldest surface in the freezer, i.e., evaporator coils [93]. This phenomenon can be explained by the driving force expressed in terms of pressure (**Figure I.10**), where $P_{ice/water\ food} > P_{air H_2O}(v) > P_{refrigeration\ coils}$ [94].

Product mass loss variation with time during freezing can be determined from the integral of the water vapor flux at the product surface over time [95]. The water vaporization flux (evaporation or sublimation) at the product surface ($\dot{m}''_{vap}$) is expressed by:

$$\dot{m}''_{vap} = h_m(C_{vap-eq} - C_{vap-sur}) \qquad \textbf{(Eq.I.2)}$$

where h_m is the external mass transfer coefficient. C_{vap-eq} is the water vapor concentration in equilibrium with the product surface. $C_{vap-sur}$ is the water vapor concentration in the surrounding gas (air).

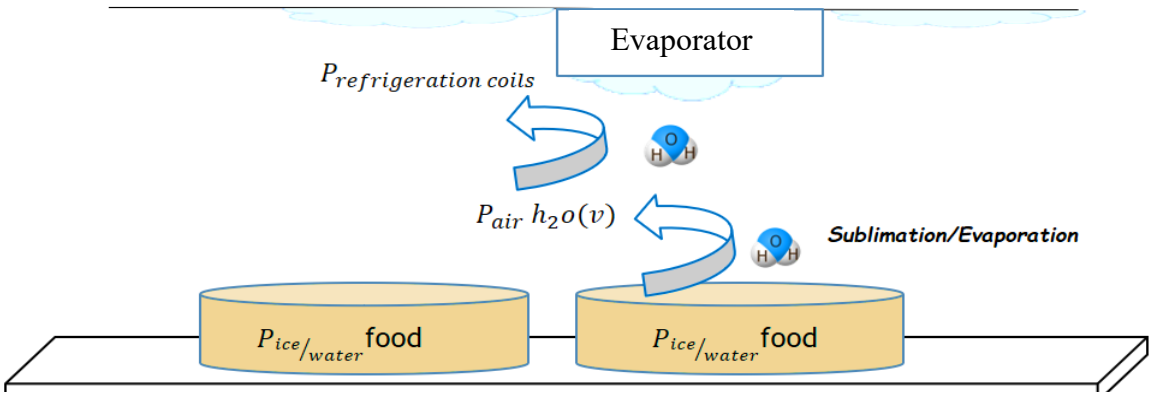

Figure I.10: Illustration of mass transfer in an industrial freezer.

Let us focus on a tunnel freezer: food products enter at a high temperature and thus a high vapor pressure at the surface, thus a large vapor pressure gradient will lead to mass loss. Since the freezing process is continuous, equilibrium inside will never be reached. Many authors [96], [97] have highlighted other factors promoting the dehydration of frozen products such as air velocity and temperature, freezing rate and product shape (the more spherical the product, the higher the evaporation rate from its surface [98]). However, they confirmed that the difference

between the pressure of water vapor or ice on the surface of the products and the surrounding air is a major cause of mass loss, which allows the vapor to escape into the air and then condense on the refrigeration coils.

Other researchers have discussed the effect of average temperature in a domestic fridge, the amplitude and frequency of temperature fluctuations on product mass loss [99]–[101], without neglecting the effect of shape, size [102] and packaging [103], and the freezing technique [104]. All these parameters exert a great influence on the mass transfer at the solid/fluid interface, which can be an important source of frost formation.

In addition, the freezing facility design has also an effect on the moisture content inside the freezer. In the air-blast tunnel, opening of doors/barriers and pressure equalizer set-ups are among the major sources of moisture. **Figure I.11**, inspired by [105], explains that in active/dynamic freezers one principal source of moisture load comes from openings as products are moved into and out of freezers. For example, in the case of an outside temperature (dock area) of 4 °C at 100 % relative humidity (RH), the partial pressure of the water vapor is 0.9135 kPa whereas it is only 0.0345 kPa inside a freezer at -30 °C at 90% RH. This pressure difference will bring the external moisture inside the freezer. This phenomenon is exacerbated when the internal temperature is lower (-40 °C) and the air infiltrating the freezer is higher. In such circumstances, the situation will become more critical.

Furthermore, the internal ventilation airflow pattern plays an important role in this disequilibrium, which makes it almost impossible to balance the pressures.

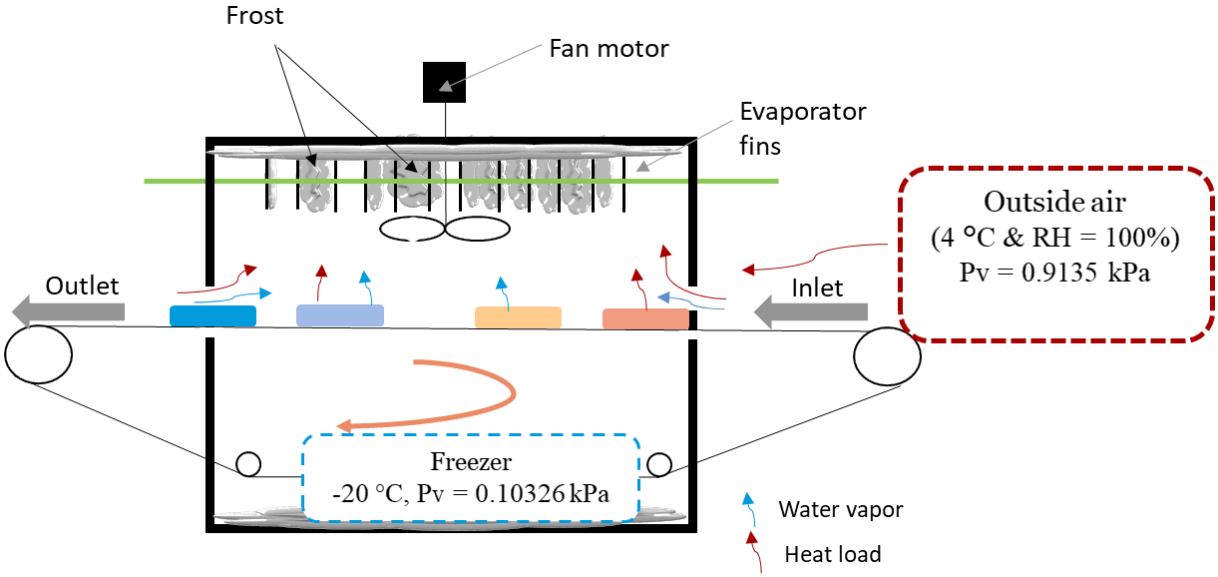

Figure I.11: Schematic of freezer air infiltration.

In the case of industrial cold warehouses, it is necessary to regularly open and close doors to move products and even if efforts are made to reduce heat and vapor transferred from the bulk air to the refrigerated space (strip doors, air curtains, fast sliding doors, etc.), they are still insufficient to prevent completely the air infiltrations.

Moreover, people entering an industrial freezing facility can also be considered as sources of humidity, especially in storage freezer, though it is relatively easy to limit these interventions to a minimum.

Finally, frost formation can be partially avoided or at least reduced by identifying humidity sources, removing the moisture at its source before entering the refrigerated space, designing sealed freezers, controlling temperature and humidity conditions. Consequently, such actions decrease unproductive periods necessary to defrost evaporators, and remove ice from conveyors, floors and walls.

Another specificity characterizing industrial deep freezing conditions is the occurrence of a type of frost called unfavorable frost. Indeed, frost is never favorable for a heat exchanger but compared to another type of frost, the concept of "favorable" and "unfavorable" can be proposed. Smith, 1989-1992 [106], [107] was the first to propose this concept by characterizing unfavorable frost as being less dense, more insulating, and having a greater impact on coil performance.

To better understand Smith's theory, let us consider an air-cooling process. When hot air passes through a cold coil, two elementary transfer parts describe the overall transfer: sensible heat and latent heat transfer.

According to **Figure I.12**, the total rate of heat transfer can be expressed by:

$$\dot{Q}_{total} = \dot{m}_{air} c_{air} (T_E - T_S) + \dot{m}_{air} L_{sv} (\omega_E - \omega_s) \quad \textbf{(Eq.I.3)}$$

$$\dot{Q}_{total} = \dot{Q}_s + \dot{Q}_L \quad \textbf{(Eq.I.4)}$$

Where $\dot{m}_{air}$ is the mass flow rate of the dry air, c_{air} is the specific heat capacity of the dry air.

The heat transfer rate can also be expressed in terms of the sensible heat load and the sensible heat ratio SHR:

$$\dot{Q}_{total} = \frac{\dot{Q}_s}{SHR} \qquad \textbf{(Eq.I.5)}$$

In general, the psychometric function of this heat transfer (**Figure I.12**) is approximatively a straight line connecting the conditions of the inlet air to the saturation conditions on the surface at the apparatus dew point (ADP) temperature (T_{adp}). As a result, the slope of this line is related to the SHR ratio. Indeed, Smith's theory says that unfavorable frost occurs when this line crosses the saturation line of the psychometric diagram.

This situation of crossing the saturation line and then producing an unfavorable frost happens when the sensible heat coefficient SHR is too low, the humidity of the incoming air is too high, and there is a considerable temperature difference between the refrigerant and the air. This may happen in particular in industrial freezing equipment where the temperature difference between the freezer and the anteroom is greater than in the air-conditioning application. Also, the temperature of the freezer is lower than those encountered in heat pump applications [33].

Reindl et al. [108] used a psychometric chart to show a typical situation of what happens in

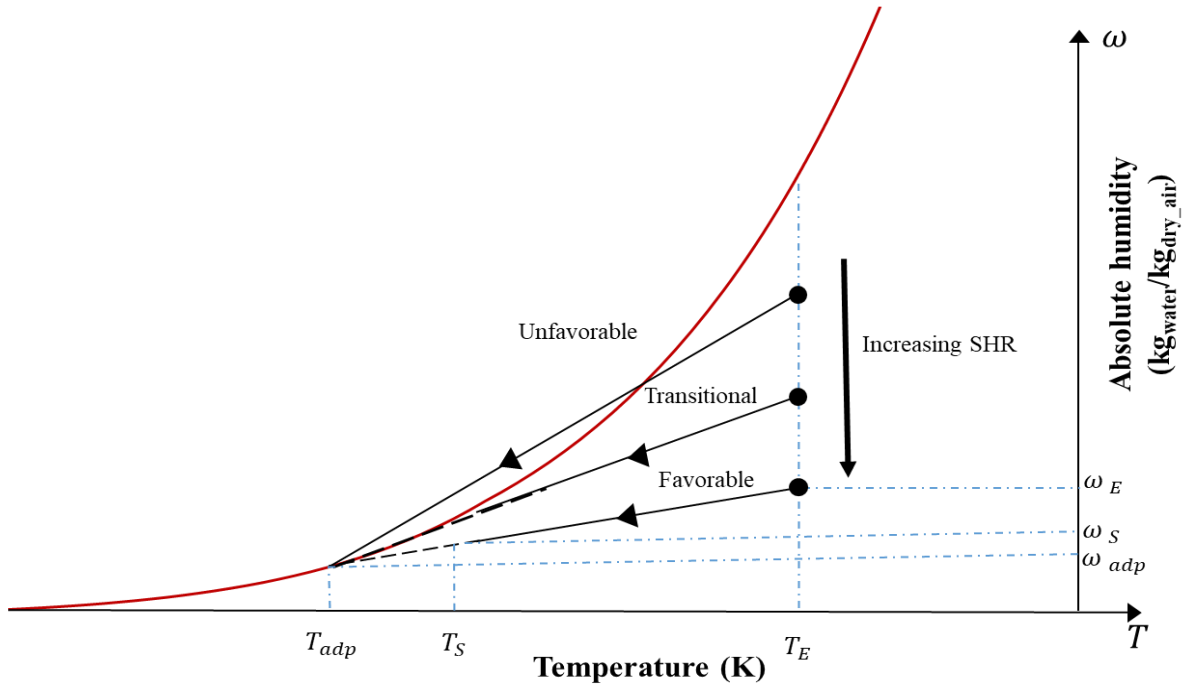

Figure I.12: Psychrometric diagram - Air heat and mass transfer through coil - favorable and unfavorable frost theory.

industrial freezers when air infiltrates into to a refrigerated space at a lower temperature. In **Figure I.13**, we differentiate three cases of an inlet air at 10 °C which mixes with air from the

refrigerated space at -12 °C before being brought to the coil conditions represented by the apparatus dew-point temperature (ADP) at -23 °C.

- Case 1: illustrates the formation of an unfavorable frost that reflects the case of an evaporator which is located closely to the doors and does not give enough time to the inlet air to be mixed with the freezer air;
- Case 2: the process line is close to the saturation curve because of the small humidity value of the inlet air;
- Case 3: illustrates the formation of a favorable frost because the air entering the coil is very close to the freezer condition.

To validate this unfavorable and favorable frost theory, Sherif et al. [33] performed a test on a liquid overfeed finned-tube evaporator. The experiment was performed at a cold coil temperature of -40 °C and started with a predetermined air humidity and SHR ratio, then by injecting a known amount of water vapor, the sensible heat ratio SHR decreased until the cooling process line crossed the saturation curve (**Figure I.12**).

When the crossing occurs, the frost formation is a combination of two processes: a process in which ice crystals is formed suspended in the air (created airborne crystals deposit on neighboring surfaces), and a process similar to the normal (i.e. favorable) frost formation

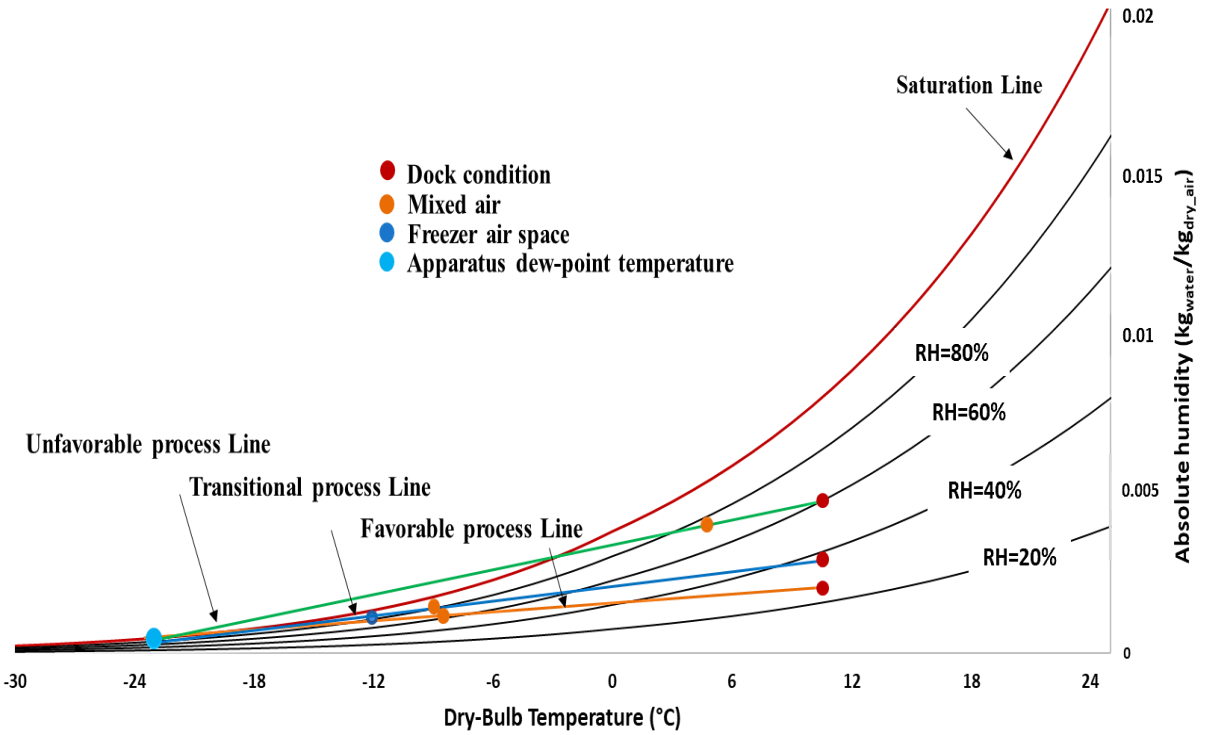

Figure I.13: Unfavorable and favorable frosting conditions on a psychrometric chart [108].

discussed previously. In addition, the authors confirmed that unfavorable frost can be considered more insulating and less favorable from a heat transfer point of view.

I.4-3. Frost Effects

Like frost growth, the frost effect has been investigated experimentally and theoretically in the literature. Several studies have been oriented towards evaluating the performance of air heat exchangers in order to understand their thermal and hydrodynamic behavior under frosting conditions. However, most of these studies only focused on the phenomena occurring at the heat exchanger level. The entire system behavior under frosting conditions has received relatively modest attention, especially regarding modeling.

Deng et al. [109] studied a wide range of industrial air coolers, and evaluated the overall heat transfer coefficient U and an energy transfer coefficient E, indicating the performance of heat exchangers under frosting conditions. **Figure I.14** shows that at an evaporation temperature of -10 °C and an air velocity of 3 m/s, an initial increase of the heat transfer coefficient occurs to an increase in surface roughness with the appearance of the first ice crystals, but it is still difficult to introduce this phenomenon into theoretical models. Then, as the frost continues to grow, air circulation in the air cooler is restricted and the overall transfer coefficient decreases. The authors also noticed that small fin spacing leads to a fast drop of the overall heat transfer and energy transfer coefficients and a rapid increase in electric power consumption. In their conditions, less than 4 mm of frost thickness led to a 50% drop in energy performance.

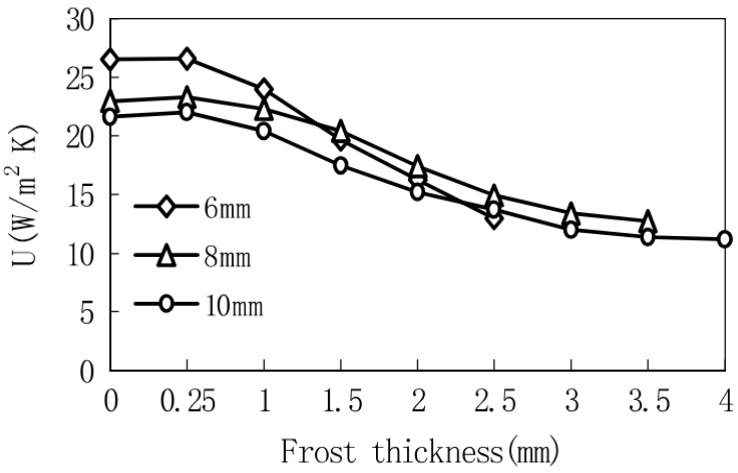

Figure I.14: Variation of overall heat transfer coefficient with frost thickness for different fin spacing (Tevap=-10 °C, Vair =3 m/s) [109].

An experimental and theoretical study of a large-scale industrial evaporator coil as frost grew on the surfaces was conducted [38], [110]. The evaporator was used to reach a space

temperature of -29 °C (evaporation temperature -34.4 °C). From this investigation, Aljuwayhel et al. [38], [110] concluded that the mass flow rate through the evaporator coil and the evaporator cooling capacity both decreased as frost accumulated on the surface.

In 2006, Xia et al. [111] evaluated the thermal-hydraulic impact of frost, defrost and refrost on five different sizes of louvered-fin flat tube heat exchangers. They showed that in all cases, frost formation induced, in two hours, a reduction of the global heat transfer coefficient and an increase of the air pressure drop, up to 50% and 80% respectively. These authors developed a thermo-hydraulic model to estimate the performance of this type of louvered exchangers. This model showed a good agreement in terms of heat transfer coefficient but not in air pressure drop, where the discrepancies were close to 52%.

Chen et al. [31], [112] developed a numerical model where the frost was treated as a transient one-dimensional porous medium. The numerical model was validated using the experimental data on a heat exchanger. The authors showed that the effect of frost is more significant on increasing the airflow pressure drop than decreasing the heat rate exchanged. The simulations were performed for surface temperatures lower than -35 °C, air temperatures lower than -15 °C and air relative humidity up to nearly 100%. The presence of frost decreases the airflow but it also leads to its maldistribution, which can reduce the performance of the evaporator by nearly 35% [13].

Tso et al, [88] revealed that an uneven wall and air temperature distribution inside a finned tube heat exchangers causes variations of the frost growth rate and densification along the coil; on the leading edge the frost thickness is greater than on the rear. In their study, a model to determine the frost distribution and dynamic behavior of an air cooler under frost conditions was developed and confirmed the previous conclusions regarding the impact of frost on heat transfer and pressure drop.

Wagner [113] conducted experimental investigations on a finned tube heat exchanger under frosting conditions and found that the airflow pressure drop across the heat exchanger is the most critical parameter influenced by frost growth. The sharp increase in pressure drop translates into an airflow decrease if this parameter is not controlled to be maintained constant.

Nonetheless, most of the models available in the literature do not consider the airflow reduction that actually takes place in fan-supplied evaporator coils operating under frost conditions, which is one of the main causes of cooling capacity reduction. Most of the models were validated using experimental data collected under constant airflow conditions. One of the only studies

taking into account the fan airflow reduction was conducted by Da Silva et al. [114]. A mathematical model was developed to analyze the influence of operational parameters on the evaporator's thermo-hydraulic performance. Experimental results collected under variable airflow conditions were used to validate the model and showed good agreement with the experimental data. It was observed that the thermal resistance due to flow blockage is the main cause for cooling capacity reduction.

Since the effects of frost accumulation are not only limited to the evaporator level, some few researches have been interested by the investigation of frost on the whole system performance. These research have shown that, under frosting conditions, the COP of a refrigeration system could be reduced by more than 15% within 40 min [53], [115].

In summary, all the previous researchers agree about the harmful effects of frost accumulation. However, related researches in this area still need further elaborating in the future, primarily on the effect of frosting on energy consumption and the overall system performance.

A. Industrial freezing specificity

Following the same approach of unfavorable frost, O'Hagan [116] investigated frost formation in conditions close to those used in industry (high inlet humidity, low SHR, and high air-refrigerant temperature difference) in order to evaluate the specific thermo-hydraulic effect of this kind of frost. The authors developed a test bench which allowed them to first confirm Smith's theory and then measure coil performance under frosting conditions. The evaluation of coil performance was done by comparing the airflow rate ($\dot{V}$) and the sensible capacity rating (UA) under frosting conditions with $\dot{V}_0$ and UA_0 under dry operating conditions.

Figure I.15 shows several results of different SHR values taken in descending order from 0.84 to 0.54 numbered from 1 to 15. The airflow drop and coil performance degradation were greater at low SHR, which is consistent with the results observed by a number of other researchers. High relative humidity and/or a very low coil temperature (low SHR) lead to a faster decline in performance over time [82], [117].

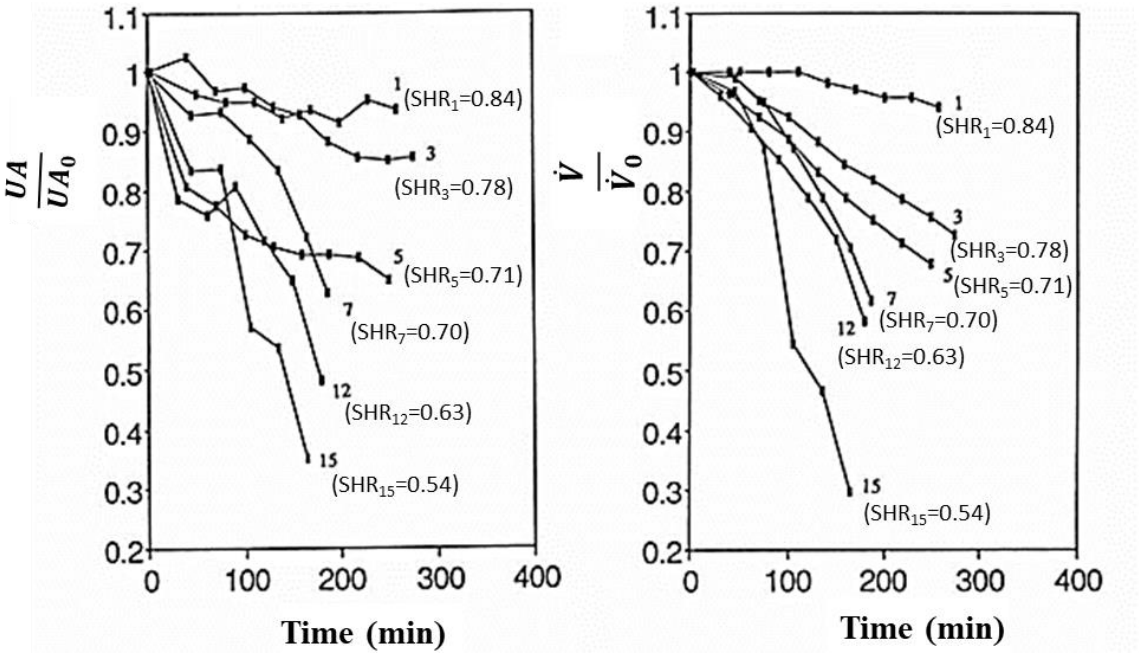

Figure I.15: Coil performance and airflow rates in frosting conditions as a function of time, adapted from [116].

Furthermore, for the same amount of frost deposited, the airflow and coil performance drop were greater at low SHR, as illustrated in **Figure I.16**. This is also consistent with Smith's theory in the fact that low SHR conditions result in less dense and less conductive frost, called ''unfavorable'' and which would both block the airflow and reduce heat transfer more rapidly.

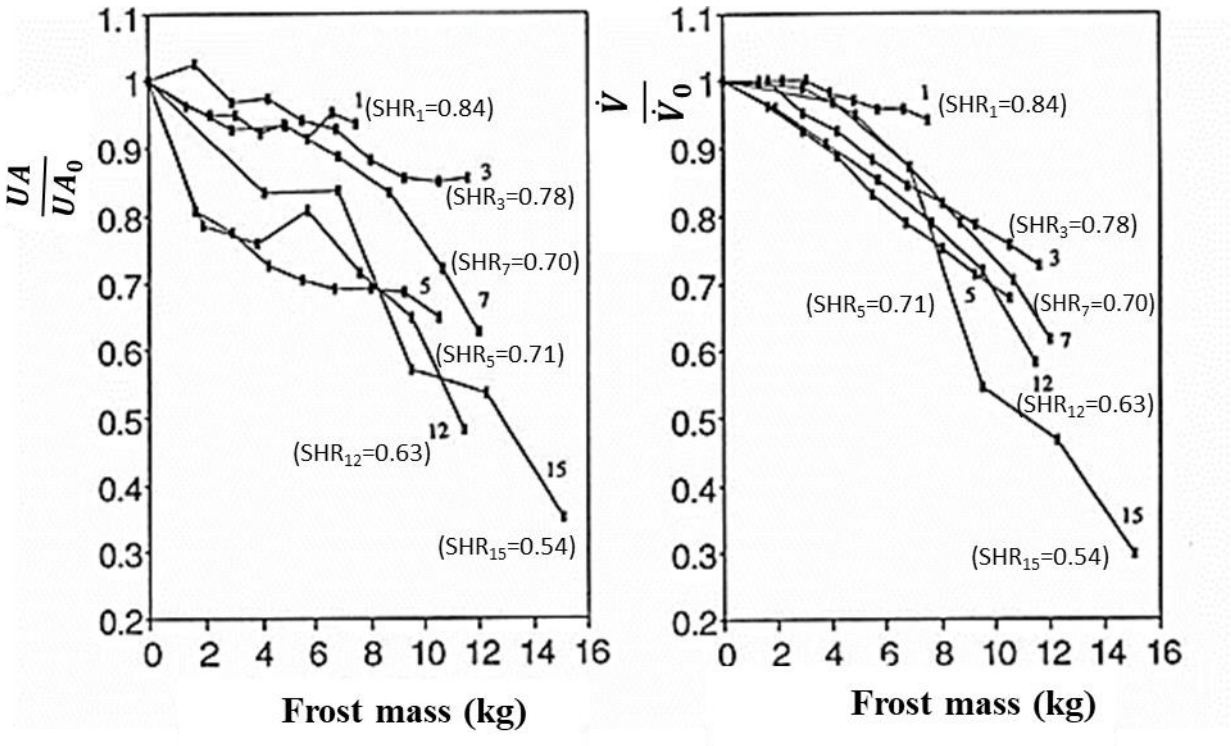

Figure I.16: Coil performance and airflow rates in frosting conditions as a function of frost mass, adapted from [116].

In summary, and as shown in **Figure I.17**, in industrial conditions another mechanism of frost formation in the air may appear along with frost formed classically, resulting in a less dense frost, a snow fog, thus quickly degrading the system's performance. This conclusion is consistent with Brian's study [45] discussed in **section I.4-2**.

Moreover, the presence of frost, as explained in the frost formation mechanism in **section I.4-2**, creates a state of non-equilibrium pressure inside the freezer, so that moisture always migrates from products to the air and then to the coldest wall in the freezer [93]. This transfer process may be responsible for cold injuries to products and quality losses.

In addition, frost formation often requires the freezing production line to stop for periods of defrosting which decreases the competitiveness of large continuous production lines. Furthermore, the frosting, defrosting and refrosting cycle can lead to temperature fluctuations [118], [119] and to a slowdown of the production line, thereby affecting the products that will be either under or over frozen, so affecting their overall quality, texture and flavor, and ultimately the company inventory [118].

Frost on the floor and refrigerator surfaces can cause slippery surfaces dangerous for staff, while lumps of frost on the evaporator or on the roof may enter food products [23].

Figure I.17: Unfavorable frost forming due to the presence of supersaturated air or/and a high coil temperature difference.

I.4-4. Frost management techniques

In industry, the management of the freezing process must be well planned in order to keep the food at an optimal temperature, so as to maintain its quality and ensure food safety, prevent waste and economic losses.

In the literature, many frost management techniques have been employed to tackle frost problems. We can classify these remedies into three main categories: the choice of defrosting system design, frost formation retardation and defrosting optimization;

Recently, two reviews have been published [22], [120], focusing on the development of defrosting techniques and frost retarding methods applicable for heating, ventilation, air-conditioning and refrigeration systems from 1950 to 2017. The purpose of this section is to complete these great researches and put the frost management methods in an industrial freezing application. An analytical study allows drawing meaningful conclusions on the possibility of applying or adapting one or more of these techniques to industrial freezers characterized by low temperatures, complex geometries, large sizes and many operating constraints (e.g. continuity of production and product quality).

As for defrosting, a variety of methods are used to remove frost including the compressor shutdown defrosting, thermoelectric heater defrosting, hot water spraying and hot gas defrosting [121]. However, the most widely-used defrosting technique in industry is hot gas defrost (HGD). The HGD technique consists in injecting the hot gas coming from the compressor discharge into the evaporator tubes, or by inversing the flow in the machine so the evaporator becomes a condenser. This last option which is limited in the case of a single evaporator system. Few attempts in experimental or modeling studies [122], [123] have been made to optimize the hot gas defrosting process either by minimizing the energy consumed during the process, minimizing defrosting time, or to predict the time and energy required to melt a frost layer.

The total heat input during a hot gas process is not easily quantifiable because the hot gas is not totally condensed and the quality of the two-phase leaving mixture depends significantly on the amount of frost and condensed water adhered to the coil at any instant. The energy that is extracted from the defrosting hot gas is used in many different ways: heating the evaporator coil surfaces, melting the frost, evaporating condensed water, and direct transfer to the environment. Moreover, the energy impacts associated with HGD technique depend mainly on the temperature of the refrigerant supplied for the hot gas defrost process and the defrost duration time. Higher refrigerant temperature results in short defrost periods but greater parasitic heating loads to the space. However, lower refrigerant gas temperature results in lower rate of sensible and latent gains but longer defrosting period is required to melt the accumulated frost. Because of this complexity, there have been few attempts to investigate the amount of thermal energy required for defrosting, to estimate the time required to complete defrost cycle

or to understand the effect of changing some input parameters (e.g. hot gas temperature). According to Neiderer [124], only 15-20% of the total energy supplied for a typical defrosting is actually used to melt the frost. Niederer evaluated a defrost process to remove 11.6 kg of frost from a coil over a 35 min defrosting period. For this coil, Niederer found that 4330 kJ were used to remove the frost whereas 28043 kJ of heat was required accomplish the defrost cycle. The results of Niederer were numerically confirmed by Hoffenbecker et al. [122]. Cole [125] notes that the energy required to melt 9.1 kg of frost from a heat exchanger weighting 669.6 kg was 4783 kJ using R22 in a hot has bypass defrost system. In this case, 24% of the total energy supplied were used to heat the metal in the evaporator. Since this metal has a large thermal capacity and must be cooled back to the evaporator's normal operating conditions at the end of the defrosting cycle, this energy represents an additional cooling load on the freezing system.

The defrost processes of an evaporator of a cold storage freezer were analyzed by Dopazo et al. [123]. The refrigerant used is R507 and the defrost process started for an air freezer temperature measured at -15 °C, an air relative humidity at 70% and a temperature on the cold surface at -28 °C. By collecting experimental data to feed a defrost model, they obtained similar trends. The energy used to melt the accumulated frost represented 29% of the total energy supplied by the refrigerant.

On an industrial ammonia evaporator [27], it has been shown that the evaporator coil must pass through several different stages (that generally last 65 min) in order to accomplish the hot gas defrost cycle (pump-down stage, hot gas stage, bleed stage). At each stage the refrigeration system has a specific behavior that must be included in the defrosting efficiency analysis and also in the numerical models. In general, hot gas defrost still represents a complex transient process which continue to pose further challenges in both modeling and optimization.

Surface treatment is one of the solutions that has received the most attention, and the performances of surfaces have been evaluated under frosting and defrosting conditions. Researchers have been interested in surface treatment for two reasons: to improve defrosting performance by facilitating frost layer removal and water drainage, and to delay frost formation. Three types of surfaces have been proposed in the literature; hydrophilic, hydrophobic and slippery surfaces. These three types have shown good retardation and drainage efficiency [126]. Wang et al. [127] Reported that after 80 min of frosting, the energy consumption for defrosting were 258.8, 301.7 and 244.7 kJ for the hydrophilic, bare and hydrophobic heat exchangers, respectively. The frost layer directly detached from the hydrophobic finned tube heat exchanger at the beginning of the HGD process, thereby reducing the defrosting time by 27.2% and the

mass of residual water by 48.7% compared to a bare finned tube heat exchanger. Recently, slippery surfaces have shown the excellent drainage property for the melted water during defrosting process, compared to bare, hydrophilic and hydrophobic surfaces [128]. Since these slippery surfaces are fabricated by injecting oils onto the surface structures, the oil of the surface helps to easily slide the condensed water delaying the frost formation and minimizing the defrost retained water. However, at low temperatures the efficiencies of these type of surfaces are negligible [128],123]. Under low temperature conditions, the rate of phase change is greater than the rate of drainage and the development of drops on cold surfaces. In other words, the water vapor is rapidly transformed into ice before it can be condensed and then drained from, or slide off, the cold surface.

One well-known advanced method in frost management is the application of an electric field. Using and increasing an electric field results in decreasing the frost growth rate, but raising the voltage to a critical point can lead to a negative effect [130]. This technique seems to be advantageous in frost delay and removal, but at low temperatures the electric field may lose this frost reduction effect.

Joppolo et al. [131] conducted several experiments measuring frost mass, air-side pressure drop and cooling capacity for different applied voltages, air velocities and evaporation temperatures on a finned-tube heat exchanger. The results showed that the electric field reduces frost mass and air-side pressure drop whereas it increases cooling capacity. Running 3 h under frosting conditions, the application of the electric field (10 kV) led to a significant energy saving by about 11.5% due to the lower frost mass accumulated (lower defrosting energy consumption),

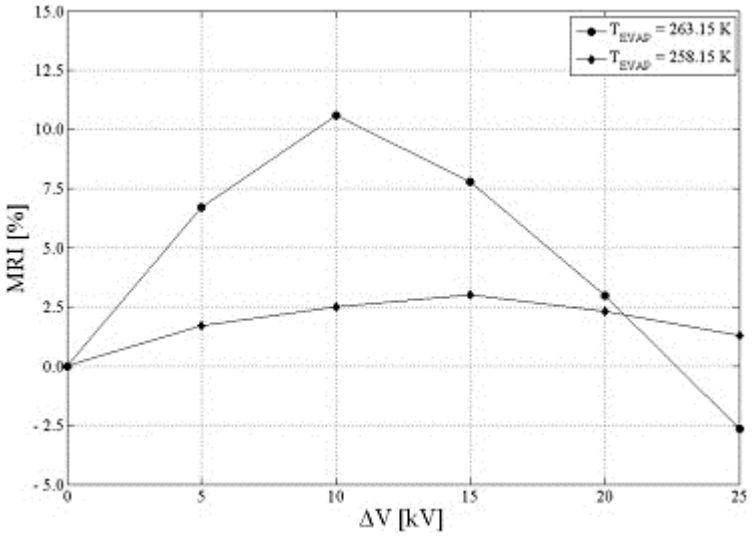

Figure I.18: Frost mass reduction versus applied voltage and evaporation temperature (T_{air} = 0 °C, RH = 80%, V_{air} = 3 m/s, t = 10,800 s) [131].

lower air pressure drop (lower fan energy consumption), and higher evaporator capacity. The energy used to create the electric field has therefore a negligible effect on the overall energy consumption. As shown in **Figure I.18**, there is a high dependence of the frost mass reduction index (MRI) to the applied voltage. As the applied voltage increases, the MRI increases up to maximum and then decreases, even reaching negative values. This means that more frost could be accumulated on the evaporator surface compared to the situation without electric field. It also to note that the MRI is greatly reduced at low evaporation temperature. The electric field is insufficient to oppose the greater driving force of frost formation and the greater chemical potential of the phase change that results from the low evaporation temperature.

Another unusual method was proposed by Wang et al [132]. They placed an ultrasonic vibration system on a tube-fin to eliminate frost from fins but it proved ineffective when the evaporator was fully obstructed. However, there were other limitations, in particular power consumption.

Wu et al. [20] performed frost formation experiments on several complex finned surfaces in cold surface temperatures up to -19 °C and found that heat exchanger geometries had a great effect on frost layer morphology and frost distribution. Also, the influence of fin orientation showed that more frost forms on horizontal fins than on vertical ones. Xia et al. [111] conducted an impact assessment test for frosting and defrosting on louvered-fin, flat-tube heat exchangers but with different geometrical parameters. This study showed that fin depth and pitch have an effect on sequential frost-defrost cycles. The wedge formed by adjacent fins tends to retain water droplets during a defrost process. These droplets freeze during subsequent re-frosting cycles, causing a considerable effect on pressure drop and heat transfer but also on frost morphology. Lee and Kim [133] performed experimental tests of the effects of fin pitch and arrangement on heat exchanger performance under frosting conditions and found that the frost layer is thinner and denser when decreasing fin pitch. The higher air velocity of air flowing between the smaller fin spacing causes higher frost surface temperatures. Therefore, the gradients of temperature and water vapor in the frost layer become higher, and more water vapor is diffused into the frost layer. The authors proposed to determine operating conditions using the maximum allowable blockage ratio for each fin spacing. Da Silva et al. [134] also showed that the closer the fins are, the more significant the frost problem is. That means that a higher fin density leads to faster frost blocking and shorter running time [135]. It is certain that increasing the fin spacing increases the operating time but it also decreases the cooling capacity due to the small heat transfer area [65]. Confronted with this problem of maintaining both optimal normal operating and frosting -defrosting performances, Kim and Lee [136] tested three

fin pitches and found that 16 FPI – fins per inch – which is equal to 630 fins per meter - showed the best thermal performance even during re-frosting cycles, compared to 14 and 18 FPI.

Furthermore, other frost management techniques were proposed via defrosting control strategies, by controlling air pressure difference, refrigerant superheat degree [137], or by measuring and detecting frost formation [138]–[140]. But so far, it has not been possible to generalize most of the studies performed and come up with a strong conclusion. Many proposals have been limited by the conditions in which they were tested.

A. Industrial freezing specificity

As pointed out previously, several frost management solutions have been proposed, but few of them were tested under closed industrial conditions.

In brief, most companies use hot gas defrost, especially in large installations, whereas electric defrosting is used mainly in small installations.

Coating or surface treatment does not seem to be very effective at low temperatures and high humidity. Slippery surfaces had the best characteristics during frosting and defrosting but their efficiency decreases at a temperature of -10 °C and it is sure they can be adapted to a temperature as low as -40 °C. Thus, hydrophobic surfaces require further tests in industrial conditions.

The vibration system does not allow the complete removal of frost but the most important practical limitation in the food industry is mainly the size of the evaporator and its resulting high energy consumption, not to speak of machine fatigue.

The application of an electrical voltage seems to have a lower effect on frost formation at low temperatures than at higher ones. This aspect requires more research and effort in this field.

In the previous sections (**I.4-2 and I.4-3**), a specific frost formation mechanism and consequently a specific type of less dense and more unfavorable frost was determined as a particularity that can occur in industrial freezers. Regarding this, O'Hagan [116] proposed two solutions; if the operation is expected to be very long under low SHR conditions, an evaporator design with large or variable fin spacing must be provided to reduce defrost frequency. If these low SHR conditions occur only for short periods, the performance drop should not be a concern because it is recovered later. The recovery may correspond to some melting and consolidation of low density unfavorable frost into a higher density frost (more favorable) when switching to a higher SHR operating conditions.

If product moisture loss is foreseeable at the beginning of the freezing process followed by a decrease in loss-rate during the cooling cycle, the industrial company must choose the optimal defrost timing in the middle of the cycle when moving from a low SHR to a higher one, to prevent the machine from operating for a long time with low performance.

Since product moisture loss is considered as a major source of water vapor in industrial freezers, its control is of the greatest practical interest. At the freezer inlet, the food surface has a higher temperature than the circulating air, thus the surface water vapor pressure is also higher than that of the air. This difference between the water vapor pressure on the food surface and that in the surrounding atmosphere is the driving force for dehydration and it is greater as the product is initially at a higher temperature. In **Figure I.19**, it can be seen that precooling the products from 40 °C to 20 °C before being introducing inside a freezer at -40 °C can reduce the driving force of evaporation by more than 60% when assuming the product water activity A_w (the ratio

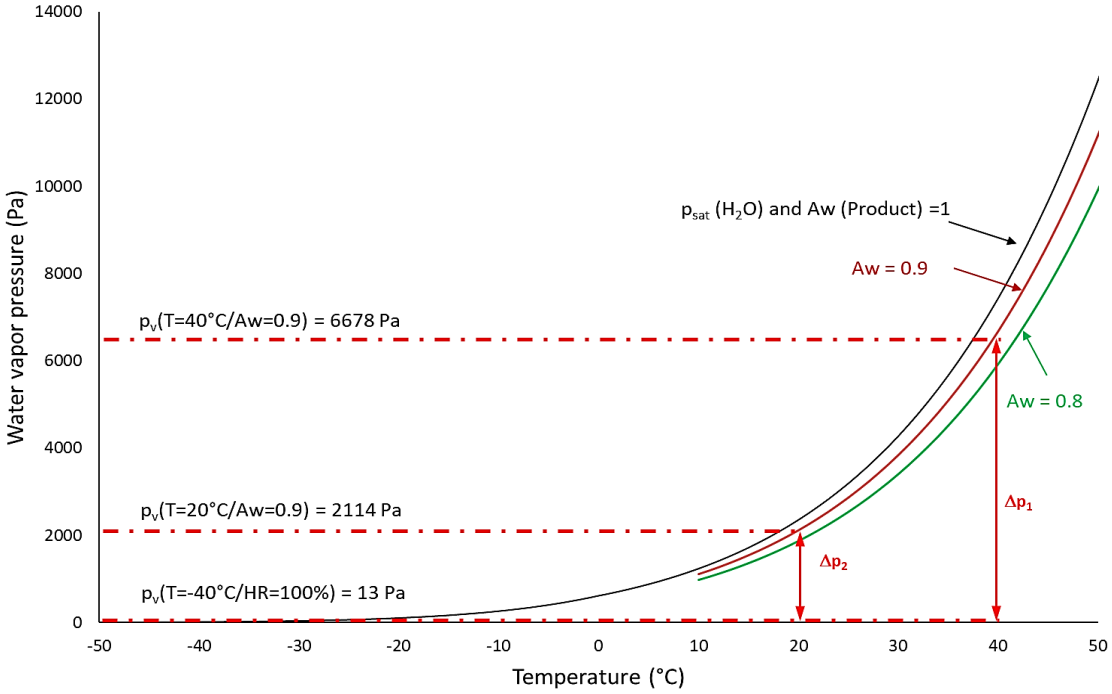

Figure I.19: Dehydration losses during freezing versus the inlet product temperature.

of the water vapor pressure of the food to the water vapor pressure of pure water under the same temperature) equal to 0.9. Therefore, product pre-cooling could be considered among the solutions, which mitigate water migration.

Cleland [141] also proposed practical solutions for industry: the evaporator should be logically placed and installed away from doors so that the inlet air has time to mix with the bulk air inside the freezer. The author claimed that it is difficult to avoid unfavorable frost formation that it why it is always preferable to have a larger fin spacing to avoid production interruption period.

In contrast, Chen [142] showed that this solution of large fin spacing causes an overconsumption of 25% which must not be overlooked in an industrial site. A critical SHR can also be determined based on an inlet air temperature or surface temperature to select the right parameters against unfavorable frost.

Another alternative that could be adopted is air inlet and dock area dehumidification [143]–[146] but this is still limited regarding its price. Physical solutions are also adopted by industry such as the use of curtains at the entry / exit of the freezer to limit air infiltrations, but they have not demonstrated great efficiency in limiting this effect. In addition, they may also constitute an obstacle that limits product movements and possible hygienic problems may occur when there is direct contact between the curtains and products. Moreover, air curtains were also tested and gave satisfactory results only when the pressure imbalance was low [147].

I.5. **Summary and conclusion**

Despite the improvements made to refrigeration, freezing and deep-freezing systems, depending on the temperature and hygrometry of the air outside or inside, respectively, frosting may occur when moist air comes into contact with a cold surface whose temperature is below dew point. This frost has a negative effect on the installation energy performance but also possibly on the quality of the products frozen.

This literature review has covered all the aspects related to this phenomenon by placing it in the context of industrial freezing conditions, since the agri-food industry is characterized in particular by many constraints, specificities and technical difficulties and the possible emergence of other challenges that have to be solved.

First of all, in addition to the two traditional mechanisms of the condensation cycle of the water vapor contained in the air, then freezing or direct desublimation, industrial freezing conditions can lead to a third frost formation mechanism. Ice crystals may be formed in the air before being deposited on the evaporator and freezer surfaces. The kind of frost layer formed in these conditions of very low temperature and medium to high humidity is less dense and more unfavorable compared to the frost formed in refrigeration or heat pump applications.

To determine how frost can influence a heat exchanger’s behavior, it is first necessary to determine its key characteristics: thickness, mass, density, morphology, and its distribution on the evaporator. These parameters are still difficult to manage or to estimate because the frost layer is always evolving in time, and it is complicated to determine the nature of frost since

several of heat and mass diffusion phenomena are in competition, especially during frost growth phase. All these parameters vary depending on the environmental, technical and operational conditions.

While research has shown great progress, significant challenges remain associated with accurately predicting frosting and defrosting processes under wide ranges of conditions. The equations governing such behavior remain insoluble by analytical methods. However, numerical approaches have given the most promising results, but they do not yet cover all the physical and technical aspects of a real system.

The determination of frost characteristics allows estimating the effect of frost growth on heat exchanger performance. In summary, frost on the evaporator reduces cooling capacity by increasing the air pressure drop, reducing airflow rates through the evaporator, and reducing heat transfer since the frost layer acts as an insulator.

Most of the models available in the literature were developed at a very small scale to obtain deeper understanding of the frost growth process. On a larger level models allow investigating the frosting process on an evaporator. Nonetheless, most of these models do not consider the reduction of airflow that actually takes place in fixed-speed fan-supplied evaporator coils, which is one of the major causes of cooling capacity reduction. Moreover, it is also necessary to develop a model based on a systemic approach to understand the behavior of each component of the freezing system under frosting conditions and to quantify the effects of frost at this global scale. Such a predictive model would permit analyzing different solutions and controlling frost development while conforming to industrial constraints of productivity and quality.

To optimize cooling systems working under frosting conditions, several strategies have been suggested to prevent the formation of frost or to eliminate frost after its formation but few solutions can be generalized or adapted to the different conditions. Very low temperatures and large installations still present challenges regarding the problem of frost management in agri-food industry.

It is obviously recommended to limit as much as possible the sources of humidity that can occur in an industrial freezer. These sources are product moisture losses, freezer doors openings and infiltrations. Air curtains and pressure equilibrium systems may be used to limit infiltrations. The products should preferably be precooled before being introduced in the freezer.

A frost delay strategy must be effective at low temperatures and must not lose this efficiency after several frosting-defrosting cycles. To achieve this, the hydrophobic surface seems to be of

great interest for future research but no general conclusion can be drawn because of the great diversity of experimental conditions in the literature.

Defrosting sequences should be less frequent to avoid production stoppages. They must be as short as possible, not consume much energy and not allow a large transfer of moisture or heat inside the freezer. Although there is no general method or strategy for any condition, the control of defrost sequences nonetheless definitely plays an important role in quantifying the efficiency of a defrosting system.

Evaporator geometry adjustment was also shown to have a considerable effect on the amount and occurrence of frost and it is considered one of the principal optimization strategies recommended. However, this solution can only be adopted during the first phase of design and conception because it is always complicated to carry out this kind of intervention later.

Numerical modeling is highly recommended for the investigation of this type of application for which experiments are more complicated. A dynamic model based on a systemic approach may be the best approach to make further optimizations. These optimizations may be defined by setting different objectives, which could be either productivity ones or energetic optimization ones, among others.

According to this review section, we conclude that several efforts have been made to overcome this problem of frost management. Most of the studies showed satisfactory results that are restricted to a limited range of application or propose technologies that are impractical under low-temperature conditions.

Finally, the food industry is always looking for refrigeration machines that are more efficient economically and energetically but that are also adapted to its technical difficulties and operating conditions, hence the need for advanced numerical models. The present thesis attempts, therefore, to fill this gap by adopting both local (frost aspects on the evaporator) and system-level numerical approaches.

CHAPTER II

Frost modeling for a system approach

CHAPTER II: Frost modeling for a system approach

The above literature shows that the ever-increasing complexity of evaluating the energy cost due to frosting phenomena on a refrigeration system has led to the emergence of system-level modeling. This high-level investigation approach is adopted in the FOODEFREEZE project, funded by ADEME, with the aim to address several issues linked to frosting process in term of energy and food quality. The present thesis work consists mainly on numerical modeling and simulation of a real industrial food freezing system. This numerical study is enhanced by many data obtained from an experimental campaign conducted by ONIRIS, CETIAT and GEA Refrigeration in a French company that produce frozen pizzas. Numerical modeling could be a good way for exploring a wide range of optimization choices by jointly addressing energy/food quality constraints.

II.1. Freezing system description

The studied freezing system and its P-h diagram are shown in Figure II.1. It consists in an ammoniac dual stage compression system dedicated to ensure refrigeration needs at two temperature levels (-40 °C and -10 °C).

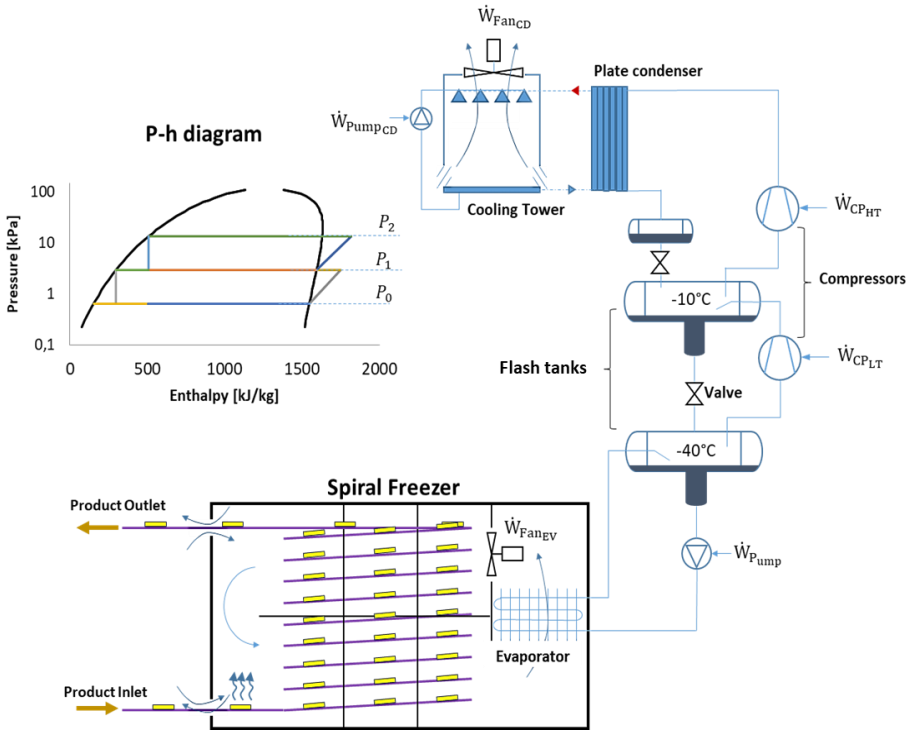

Figure II.1: Schematic of the freezing system & P-h diagram.

The LP screw compressor sucks the vapor from the low temperature flash tank at pressure P_0 (Low pressure). Then, it discharges this vapor into an intermediate flash tank at pressure P_1 (Medium pressure). The HP screw compressor sucks the vapor from this tank and discharges it at pressure P_2 (High pressure). After condensation in a plate condenser, the ammonia is expanded from P_2 to P_1, and the liquid-vapor mixture is introduced into the intermediate tank. The latter feeds a plate heat exchanger in order to cool a glycol water solution distributed to processes and positive cold storage rooms.

The ammonia is expanded from P_1 to P_0 and the liquid-vapor mixture is introduced into the tank at temperature around -40 °C. This tank supplies the freezers and the negative cold storage rooms thanks to recirculating pumps.

It is necessary to specify that the distribution of ammonia from flash tanks to other elements than the freezer have not been considered in this study.

The freezer which is the modeling object is a spiral freezer operating with an overfeed finned tube evaporator and having a cooling capacity of about 500 kW assured by 4 parallel heat exchangers. In order to simplify the model and reduce the simulation running time, it was chosen to model only one freezer's evaporator. It means that the modeled freezer would have ¼ of the cooling capacity. Considering this, all the data that will be presented further concerns a food freezer of approximately 126 kW as nominal cooling capacity.

Table II.1 summarizes all the system data and operating conditions. Thereafter, each component will be individually presented and modeled.

Table II.1: Freezing system data and operating conditions.

Evaporator geometry	Finned tube
Evaporator coil type	Controlled pressure receiver liquid overfeeds
Evaporator circuiting type	Parallel
Evaporator fin pitch	Digressive pitch 24-12-8 mm
Nominal capacity	126 kW
Refrigerant	Ammonia
Evaporation Temperature	-40 °C
Evaporator air inlet temperature (nominal)	-35 °C
Number of fans	1
Nominal airflow rate	76,000 m^3/h
Nominal air velocity at the front area (m/s)	4.32

Vapor-Liquid separator capacity (Low pressure)	6 m^3
Vapor-Liquid separator capacity (Medium pressure)	3 m^3
Condenser Type	Ammonia/water
Condenser water cooler system	Cooling tower

II.2. **System modeling architecture and procedure**

The frost process and the overall system is modelled in Modelica, which is an equation-based, object-oriented modelling language [148]. The model equations detailed in the following sections are directly implemented and solved in Dymola environment version 2020x. Since the Modelica language is an acausal language, those equations are expressed in a neutral form without consideration of computational order or even need to give a procedure to solve them. Dymola uses its internal algorithm for solving differential/algebraic equations. In this thesis, the DASSL algorithm [149] was selected to solve all the presented equations. The convergence criterion is satisfied when the computed local error is less than the given tolerance. The latter is chosen as 0.001.

Unlike the traditional modeling procedures, one of the primary advantages of using Modelica is that HVAC engineers and researchers can focus on improving the dynamic models, while being relieved of the challenges from selecting and implementing up-to-date solvers. On the other hand, Modelica has already proved great capability for simulating multi-physical systems and has been proven to be suitable for the modeling of large and complex thermodynamics systems [104], [150]–[153].

The objects of Modelica language adopt the concept of class or component, which corresponds to a single element or sub-system part. Therefore, as illustrated in **Figure II.2**, the actual freezing system studied in this thesis can be separated into small components. Each component has its physical attributes. Once all single components are defined, the relationship among these components is determined to model the final behavior of the entire system.

Many Modelica-based open and commercial libraries have been developed for the modeling of heat pump, refrigeration, cooling and automotive air conditioning systems [154]–[156]. Recently, TLK Thermo company [156] developed a new commercial library called TIL. This latter is nearly similar to the other Modelica libraries. The main difference is the pressure states number. TIL library assigns to each volume of two-phase fluids a pressure state. The time derivative of the pressure is unified among the same pressure level instead of calculating the

time derivative of the pressure in each element when solving the balances equations. As a consequence, the simulations are faster and more reliable. In this thesis, the components' models are adapted from TIL and building libraries [154] coupled with self-developed models.

Using TIL library:

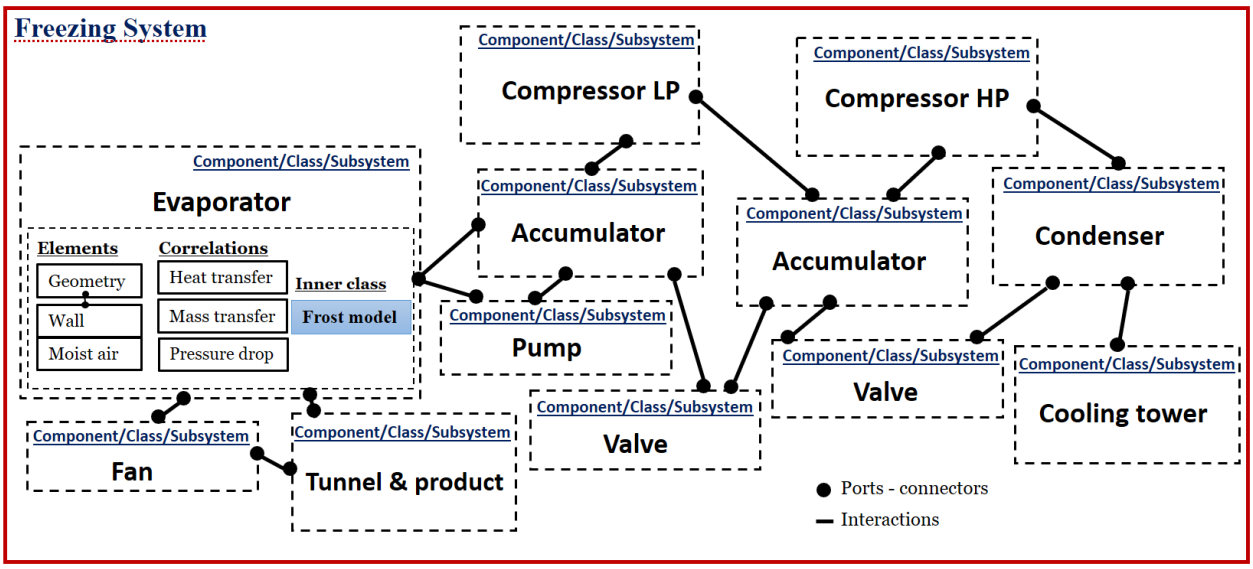

Figure II.2: Freezing system modeling architecture.

- The evaporator and condenser models were chosen from the *heat exchangers* package. The models are generally composed using cells (finite volume elements) to represent the two fluid flows and the separating wall resulting in a sandwich structure. A record geometry is adapted in order to describe the actual geometric parameters and material types. Then, internal functions compute the external and internal surfaces as well as the external and internal cross-sectional areas. These outputs are transmitted to the air, wall and fluid element in order to solve heat transfer, mass transfer, pressure drop, and fin efficiency correlations.
- The moist air and wall elements of the evaporator model take into consideration the frost formation defined as *inner class*. The existed TIL library frost model has been used to predict the performance of a R404A blast freezer. This frost model considers a constant frost density of about 128 kg/m^3. This assumption allows to predict adequate trends but not to investigate correctly the frost properties neither the frost effect on the thermo-hydraulic performance of the freezer [44]. As consequence, *a frost model, which takes into account both physical phenomena of frost deposition and moisture diffusion inside the frost layer, was developed using inheritance properties of Modelica language*.

- The separators models were chosen from the TIL library Accumulator package. Their dynamic model is described by Strupp et al. [157] and Bockholt et al. [158]. The model will be defined in **chapter 3**.
- The expansion valves models were selected from *Valves* package. Orifice valve model based on expansion coefficient is adopted.
- The fan model was selected from *Fans* package; A second order fan defined by quadratic characteristics and consideration of power losses is coupled to the evaporator. More details will be further presented in **section III.2**.

Elements and components ports are created in order to identify the interaction possibilities between the different components of the modeled system. In the present system model, gas, liquid, two-phase fluid and heat ports are used in order to transmit pressure, enthalpy, mass flow rate and heat flux.

Based on VDI heat atlas database [159] the moist air properties are calculated while the ammonia properties are based on Refprop10.0 [160]. These two mediums are defined in a component called *SIM (system information manager)* that stores all information related to their properties and also computes numerical information like the total refrigerant mass and total inner volume which are important system properties.

Using Building library:

- A model of a cooling tower with water pump having an ideally controlled mass flow rate as input signal is selected from building library. This cooling tower is based on Approach temperature defined as the difference between the cold water temperature leaving the tower and the ambient wet bulb temperatures. This model is chosen in order to simplify the freezing system model since the cooling tower is considered for second interest in the whole analysis.

Based on Self-development:

- A screw compressor model using manufacturer data is developed on TIL library. The model is almost based on the same three evaluation parameters initially proposed by Föresterling [161] and used to describe the mass flow rate, the driving power and the discharge temperature: volumetric efficiency and the isentropic efficiency.
- A dynamic model of frost formation on a flat plate is developed using Modelica language and simulated on Dymola environment. Thereafter, the model is coupled to TIL library where it is considered as a sub-model in the *heat exchanger* package.

II.3. **Development and validation of a frost model adapted to a system approach**

Since the present study focuses on a system-level simulation, this section aims to develop a suitable frost model that takes as much as possible the physical phenomena but without any secondary details and computational complexity. The literature review showed that the only available empirical correlation able to predict frost properties under freezing conditions is not suitable to finned tube geometry. Moreover, the CFD based models seemed to be inconvenient with this type of industrial application. On one hand, they describe the microscopic aspects of frost formation which are not very interesting for a system approach. On the other hand, they may need a huge calculation time when applied to this size of evaporators. Therefore, a quasi-steady state modeling of frost accumulation is adopted, considering the frost layer as a one-dimension porous medium subject to heat and mass transfer.

II.3-1. Main concept and assumptions

In frost formation process, moist air passes over a cold surface with a temperature below the freezing point of water and the dew point of the air. This forced convection heat transfer mode is driven by the gradient of temperature between the air stream and the frost surface. It is accompanied by mass transfer because in the meantime, a water vapor concentration gradient causes a water vapor flux from the bulk flow to the cryo-surface. Part of this total flux freezes at the surface increasing the thickness of the frost layer and releasing a latent heat while the remainder part diffuses inside the frost layer increasing its density. Finally, both sensible and latent heat are transferred to the cold wall by conduction. In this thesis, the frost model proposed is based on a detailed physical description of all the phenomena described above. It should be noted that both vapor diffusivity inside the frost layer and frost thermal conductivity are determined using literature correlations. Moreover, the following assumptions are adopted:

- The frosting process is assumed to be a quasi-steady-state;
- Heat and mass transfer from the air-frost interface to the cooling plate are one-dimensional processes;
- The frost distribution is uniform on the entire control volume and the frost layer is characterized by average properties;
- The thermal conductivity of frost depends only on the frost density;
- The amount of water-vapor absorbed in the frost layer is proportional to the water-vapor density in the frost layer;

- The convection and radiation heat transfer modes inside the frost layer are neglected;
- The perfect gas law is applied for the water vapor, and local thermodynamic conditions prevail throughout the frost layer;
- An analogy between heat and mass transfer on the interface of frost and air is applied;
- The pressure of the airflow and the inner-frost pressure are assumed uniform.
- In each control volume, the frost thickness and density are assumed to be the same for the tube and the fin.

The overall water vapor mass flux received by the frost layer is divided into the growth and the densification mass fluxes. As consequent, the water vapor mass balance can be written as:

$$\dot{m}_v'' = \frac{d}{dt}\int_{x=0}^{x=\delta_{fr}} \rho_{fr}\, dx = \frac{d}{dt}\left(\bar{\rho}_{fr}\delta_{fr}\right) \qquad \textbf{(Eq.II.1)}$$

$$\dot{m}_v'' = \bar{\rho}_{fr}\frac{d\delta_{fr}}{dt} + \delta_{fr}\frac{d\bar{\rho}_{fr}}{dt} \qquad \textbf{(Eq.II.2)}$$

Where ρ_{fr} is the local density of the frost layer, $\bar{\rho}_{fr}$ and δ_{fr} are the average density and thickness of the frost layer, respectively. $\bar{\rho}_{fr}\frac{d\delta_{fr}}{dt} = \dot{m}_\delta''$ is the densification rate and $\delta_{fr}\frac{d\bar{\rho}_{fr}}{dt} = \dot{m}_\rho''$ is the thickening or the growth rate. The main goal of this physical model is to define each quantity of $\dot{m}_\delta''$ and $\dot{m}_\rho''$. For this purpose, the balances equations are divided in several parts ranging from the frost-air interface and cascading down to the cold plate at x=0 (**Figure II.3**).

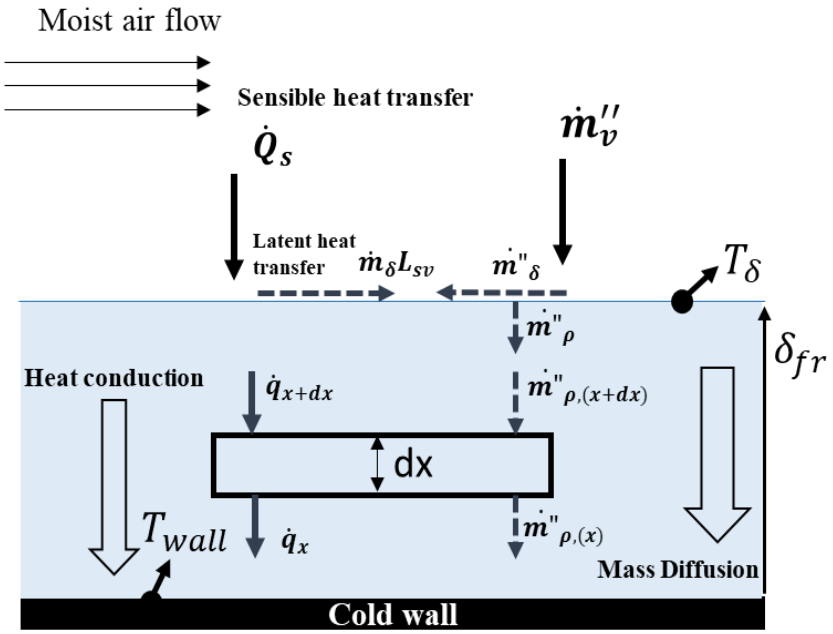

Figure II.3: Heat and mass transfer on frost surface and inside frost layer.

II.3-2. At frost/air interface

On the frost surface, both sensible and latent heat transfer occurs simultaneously.

The sensible heat flux is expressed as:

$$\dot{Q}_s'' = \alpha_a \times (T_{a,in} - T_\delta) \quad \textbf{(Eq.II.3)}$$

Where T_δ is the frost surface temperature, α_a is the convective heat transfer coefficient.

The frost surface is exposed to a total water vapor mass flux determined by:

$$\dot{m}_v'' = \alpha_m \times (\omega_{a,in} - \omega_{\delta,sat}) \quad \textbf{(Eq.II.4)}$$

Where: $\omega_{\delta,sat}$ is the saturated humidity ratio of the moist air at the frost surface and α_m is the mass transfer coefficient computed via α_a applying Lewis analogy.

At frost/air interface, only the latent heat corresponding to the increase of frost thickness is considered. The latent heat flux is given by:

$$\dot{Q}_L'' = \dot{m}_\delta'' \times L_{SV} \quad \textbf{(Eq.II.5)}$$

Where: L_{SV} is the heat of sublimation.

II.3-3. Inside the frost layer

To model the transfers in the frost layer, both mass and energy balances are applied to a finite volume of dx thickness:

A. Mass transfer:

The water-vapor diffusion through a porous frost layer is due to the Brownian motion. Assuming that this phenomenon occurs only in a direction normal to the cold plate, the diffusion flux could be calculated according to Fick's law as:

$$\dot{m}_\rho'' = -D_{eff} \left.\frac{d\rho_v}{dx}\right|_{x=\delta_{fr}} \quad \textbf{(Eq.II.6)}$$

where: D_{eff} is the effective diffusion coefficient.

The mass conservation in the finite volume of frost layer leads to express the frost density variation as:

$$\frac{\partial \rho_{fr}}{\partial t} = D_{eff} \frac{\partial^2 \rho_v}{\partial x^2} \quad \textbf{(Eq.II.7)}$$

B. Energy transfer:

The energy balance upon the finite volume states that

$$\frac{\partial}{\partial x}\left(k_{fr} \frac{\partial T_{fr}}{\partial x}\right) - L_{SV} \frac{\partial \dot{m}''_{\rho}}{\partial x} = \frac{\partial}{\partial t}(\rho_{fr} C_{p,fr} T_{fr}) \quad \textbf{(Eq.II.8)}$$

Considering that the frost layer is in quasi-steady state, the term representing the thermal storage of the frost ($\frac{\partial(\rho_{fr} C_{p,fr} T_{fr})}{\partial t} = 0$) will be neglected in the present model.

The equation **(Eq.II.8)** could be simplified as:

$$k_{fr} \frac{\partial^2 T_{fr}}{\partial x^2} = L_{SV} \frac{\partial \dot{m}''_{\rho}}{\partial x} \quad \textbf{(Eq.II.9)}$$

C. Water vapor density:

The water vapor density could be determined by applying the assumption that the amount of water vapor absorbed by the frost control volume is proportional to the water-vapor density in the control volume. Its expression could be presented as follows:

$$D_{eff} \frac{\partial^2 \rho_v}{\partial x^2} = \alpha_{ab} \rho_v \quad \textbf{(Eq.II.10)}$$

Where: α_{ab} is an absorption coefficient determined solving equation and using the following boundary conditions:

At x=0

$$\rho_v = \rho_{v,sat}(T_{wall})$$

$$\frac{\partial \rho_v}{\partial x} = 0 \quad \textbf{(Eq.II.11)}$$

At x=δ_f

$$\rho_v = \rho_{v,sat}(T_{\delta}).$$

The two conditions of vapor density at frost and wall surface are obtained using the local thermodynamic equilibrium. While, the $\frac{\partial \rho_v}{\partial x} = 0$ is the condition supposed that the cold wall is an impermeable surface.

Following this approach, and by applying the ideal gas law, one can find the distribution of water vapor density within the frost layer and the absorption coefficient as follows:

$$\boldsymbol{\rho_v(x) = \rho_{v,sat}(T_{wall}) \times \cosh(\varphi x)} \quad \textbf{(Eq.II.12)}$$

$$\boldsymbol{\alpha_{ab}=D_{eff}[(\frac{1}{\delta_f}\cosh^{-1}(\frac{T_{wall}\times p_{v,sat}(T_\delta)}{T_\delta \times p_{v,sat}(T_{wall})}))]^2} \quad \textbf{(Eq.II.13)}$$

where: $\varphi = \sqrt{\frac{\alpha_{ab}}{D_{eff}}}$

D. Temperature distribution within the frost layer:

Substituting **(Eq.II.6)** into **(Eq.II.9)** yields

$$\boldsymbol{k_{fr}\frac{\partial^2 T_{fr}}{\partial x^2} = -L_{SV}\frac{\partial^2 \rho_v}{\partial x^2}} \quad \textbf{(Eq.II.14)}$$

(Eq.II.10) allows **(Eq.II.14)** to be rewritten as

$$\boldsymbol{\frac{\partial^2 T_{fr}}{\partial x^2} = -\frac{\alpha_{ab}L_{SV}}{k_{fr}}\rho_v(x)} \quad \textbf{(Eq.II.15)}$$

The frost distribution temperature could be found solving the equation **(Eq.II.9)** subjected to the boundary conditions given as following

$$\begin{array}{ll} \textbf{At x=0} & \boldsymbol{T_{fr} = T_{wall}} \\ \textbf{At } \boldsymbol{x=\delta_f} & \boldsymbol{k_{fr}\frac{\partial T_{fr}}{\partial x} = \dot{q}''_s + \dot{q}''_\delta} \end{array} \quad \textbf{(Eq.II.16)}$$

Solving **(Eq.II.9)** yields the temperature distribution within the frost layer $T_{fr}(x)$. Thereafter, the frost surface temperature at $x = \delta_{fr}$ could be calculated.

To be able to develop those analytical solutions, the frost thermal conductivity k_{fr} and the effective mass diffusivity D_{eff} are computed as function of average frost density.

II.3-4. Correlations and initial conditions

A. Diffusion coefficient:

The effective diffusion coefficient (also referred to as the apparent diffusion coefficient) in a porous medium is different from the free or the binary diffusion coefficient *D*. This is because, the diffusion in porous media is modified due to many factors: The available cross section for diffusion (porosity), the tortuosity of the porous frost structure and the complexity of streamlines, phase transitions, the variation of pore diameters and others. As consequence, the effective diffusion coefficient is expressed mathematically by multiplying the molecular water vapor diffusivity in moist air *D* by a diffusion resistor factor μ:

$$\boldsymbol{D_{eff} = \mu D} \qquad \textbf{(Eq.II.17)}$$

Several attempts focus on the identification of the diffusion resistance factor in equation **(Eq.II.17)** but no direct measurements have been done due to the complexity of the process. This factor is defined via the porosity and tortuosity as follows:

$$\boldsymbol{D_{eff} = D\frac{\varepsilon}{\tau}} \qquad \textbf{(Eq.II.18)}$$

where: ε and τ are the average frost porosity and tortuosity, respectively. The frost porosity could be expressed as:

$$\boldsymbol{\varepsilon = 1 - \frac{\overline{\rho}_{fr}}{\rho_{ice}}} \qquad \textbf{(Eq.II.19)}$$

The tortuosity is computed using the empirical relationship proposed by Auracher [162]. Auracher has combined theoretical studies of frost structure with some careful measurements of diffusion in capillary tubes under frosting conditions and he proposed the following expression:

$$\boldsymbol{D_{eff} = D \times \frac{1 - \varepsilon_{ice}}{1 - C_0 \varepsilon_{ice}}} \qquad \textbf{(Eq.II.20)}$$

where: C_0 is a coefficient empirically determined to be 0.58. ε_{ice} is the average ice volume fraction in the frost layer ($\varepsilon_{ice} = 1 - \varepsilon$).

To compute the binary coefficient diffusion *D*, Incropera & De witt. [163] detailed that it is proportional to $P^{-1}T^{\alpha}$ where the pressure can be assumed to be the atmospheric pressure. It results that:

$$\boldsymbol{D = A.T^{\Upsilon}} \qquad \textbf{(Eq.II.21)}$$

Table II.2 reported the coefficient A and ϒ found in literature and reviewed by Hadid et al. [164] These empirical coefficients and some other additional ones were the subject of an analyze made by Nemer et al [89]. They found that all these empirical correlations predict very similar results and this for a wide range around frosting conditions. In this study, Auracher's correlation is adopted.

Table II.2: Empirical coefficients of the diffusion coefficient equation.

References	**A**	ϒ
Eckert and Drake [165]	9.756×10^{-9}	1.81
Auracher [162]	1.432×10^{-9}	1.72
Incropera & De witt [163]	5.054×10^{-9}	1.5
Hedh [166]	1.176×10^{-9}	1.75

B. Frost thermal conductivity:

Different correlations for frost thermal conductivity are proposed in the literature. However, for most of these correlations, the validity interval is limited to heat pump conditions. In this study, the correlation provided by Lee and al. [63] is adopted since its application condition depends only on frost density ($\rho_{fr} < 500\ kg/m^3$). This correlation has been developed under low wall temperature (-20 °C) and high air velocity (4 m/s). It has been also used under freezing condition and showed good prediction compared to experimental results [27]. The thermal conductivity of frost layer only varies with average frost density as:

$$\boldsymbol{k_{fr} = 0.132 + 3.1310^{-4}\overline{\rho}_{fr} + 1.6\times10^{-7}\overline{\rho}_{fr}{}^{2}} \qquad \textbf{(Eq.II.22)}$$

C. Frost growth and densification:

Following the equations **(Eq.II.6)** and **(Eq.II.12)**, the amount of vapor diffused inside the frost layer is determined by integration.

$$\boldsymbol{\dot{m}''_{\rho} = \int_{x=0}^{x=\delta_{fr}} \alpha_{ab}\rho_{v}(x)dx} \qquad \textbf{(Eq.II.23)}$$

Following the 1st order forwarded difference integration, the average density for the next time step is obtained from

$$\bar{\rho}_{fr_{t+\Delta t}} = \bar{\rho}_{fr_t} + \frac{\dot{m}''_{\rho}}{\delta_{fr}} \Delta t \qquad \textbf{(Eq.II.24)}$$

Substituting $\dot{m}''_{\rho}$ in equation **(Eq.II.1)**, the frost thickness in each step could be found as:

$$\delta_{fr_{t+\Delta t}} = \delta_{fr_t} + \frac{\dot{m}''_{v} - \dot{m}''_{\rho}}{\bar{\rho}_{fr_t}} \Delta t \qquad \textbf{(Eq.II.25)}$$

D. Initial conditions:

As stated in previous section, the early stage of frost formation is not modeled. Instead, equations **(Eq.II.24)** and **(Eq.II.25)** require initial conditions for the frost thickness and for the frost density. Moreover, it is worthwhile to mention that the frosting models are strongly dependent upon the initial condition of the frost layer including the frost thickness and density. Many authors use arbitrary low values based on Jones and Parker investigation [72] where they have recommended frost thickness as about 10^{-6} m and initial frost densities within the range of 8-48 kg.m^{-3}. Jones and Parker have mentioned that the results are not affected by these initial values. Some authors chose initial conditions based on experimental data [63]. This method is more precise but not practical for simulation tools since it would require experimentation for each simulation case. To overcome this aspect, some authors [40], [167] use empirical correlations from literature to predict initial frost density with respect to frost surface temperature. However, the disadvantage of this approach is that the accuracy of such empirical correlations for the frost density is strongly restricted by the experimental conditions and might not be guaranteed over the ranges of extrapolative use.

Sensitivity analysis have been conducted by Nemer [89] to determine the value of initial frost layer thickness and density such that it does not impose a substantial impact on the simulation. The results shows that for this kind of model presented in this thesis, the simulation results are less sensitive to the initial frost thickness values and they are almost constant for different initial frost densities within the advised range by Jones and Parker [72]. Thereafter, the initial conditions are assumed as:

$$\bar{\rho}_{fr_{t=0}} = 30 \ kg/m^3 \qquad \textbf{(Eq.II.26)}$$

$$\delta_{fr_{t=0}} = 10^{-6}\, m$$

II.3-5. Frost model Validation

This section deals with the validation of the frost model discussed above. The validation has been performed first using experimental data from the literature for a flat plate under five different conditions. The main purpose is to verify the reliability of the model within a wide range of experimental operating conditions including those typically encountered in industrial freezers. Thereafter, the validation has been carried on a complex geometry with the aim to check the coupling of the heat exchanger-frost models, notably in TIL library.

A. Validation on a simple plate:

The model presented in the previous section is plotted and compared with frosting data from Sahin [168] and this for three different physical situations summarized in **Table II.3**. The experimental study of Sahin [168] was conducted on a cold aluminum plate having a size of $50.6 \times 30.4 \times 1.27$ cm^3. The average value of heat transfer coefficient for forced convection on a flat plate, defined in **(Eq.II.3)**, is evaluated based on a simple correlation of Nusselt number for laminar boundary layer Re $<5\times10^5$ [169].

$$Nu = 0.664 \times Re^{\frac{1}{2}} \times Pr^{\frac{1}{3}} \qquad \textbf{(Eq.II.27)}$$

Based on Lewis analogy [170], and assuming that Lewis number is equal to 1, the mass transfer coefficient α_m, defined in **(Eq.II.4)** is determined as follow:

$$\alpha_m = \frac{\alpha_a}{Le^{\left(\frac{2}{3}\right)} \times Cp_a} \qquad \textbf{(Eq.II.28)}$$

Table II.3: Experimental Conditions used for frost validation.

Experimental conditions	T_a (°C)	T_{wall} (°C)	ω_a (kg/kg)	V_a (m/s)
Case 1A	13	-25	0.0039	2.12
Case 2A	13	-9	0.0069	2.18
Case 3A	13	-15	0.0069	2.18

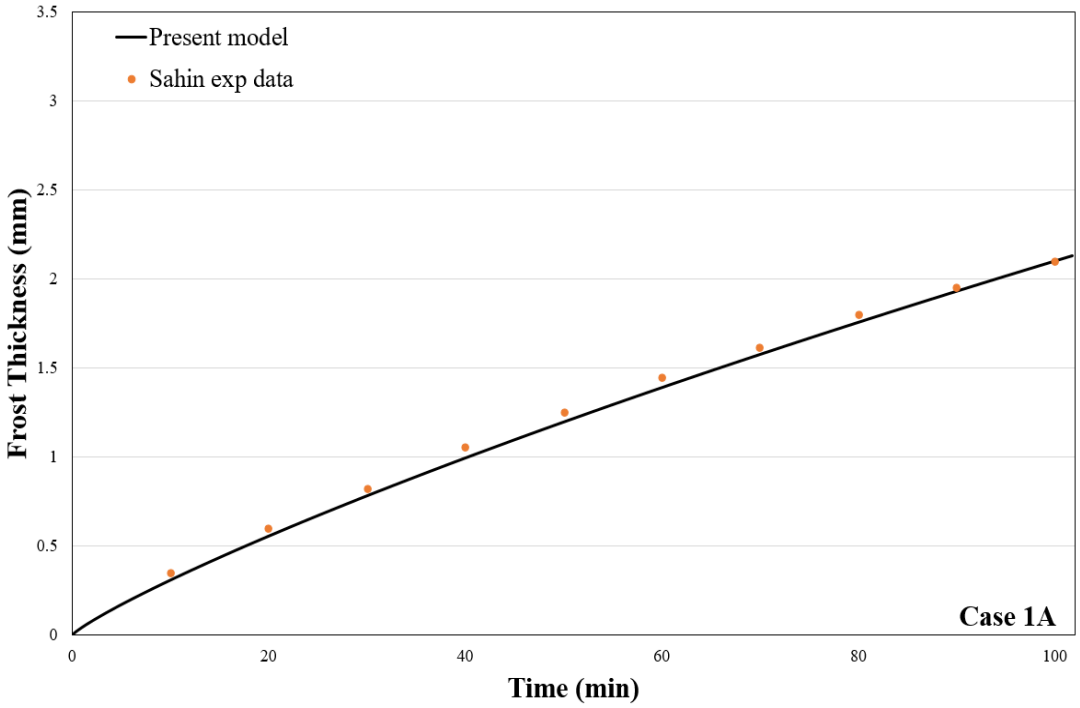

Figure II.4: Experimental and numerical frost thickness at T_{wall} = -25 °C, T_a = 13 °C, ω_a= 0.0039 kg/kg, V_a = 2.12 m/s – Case 1A.

Figure II.4, **Figure II.5** and **Figure II.6** show the comparison between experimental data. The present frost growth model agrees well with the experimental data of Sahin and it presents high accuracy in the prediction of frost thickness for the three cases.

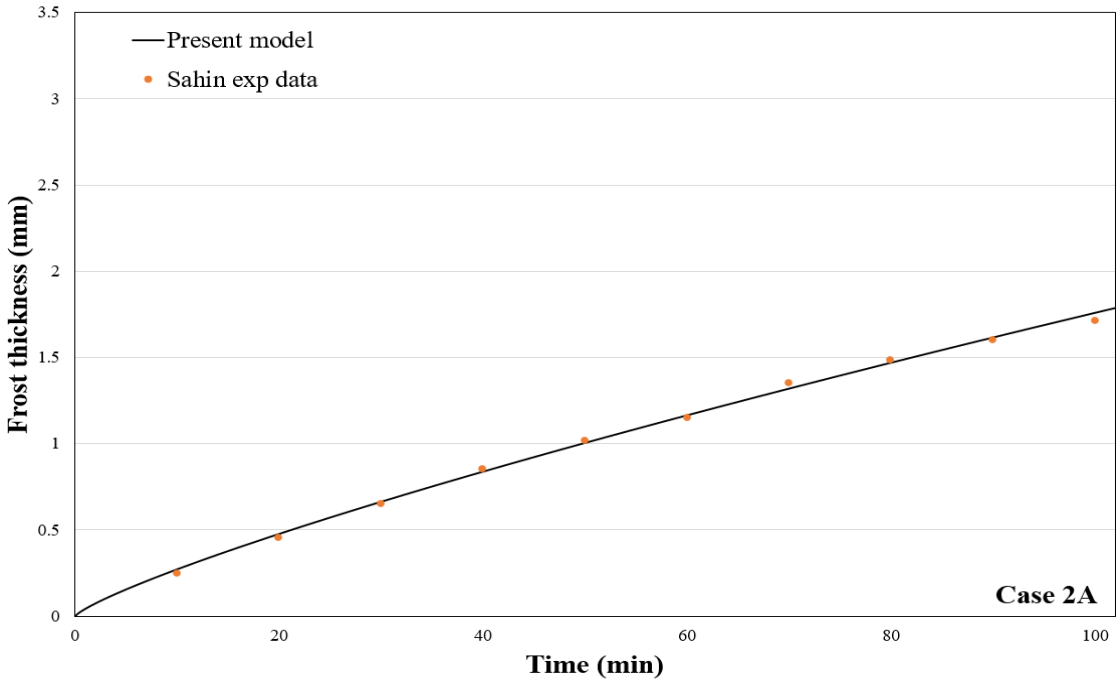

Figure II.5. Experimental and numerical frost thickness at T_{wall} = -9 °C, T_a = 13 °C,ω_a= 0.0069 kg/kg, V_a = 2.18 m/s – Case 2A.

The root mean square error (RMSE) for the results obtained from the model with the experimental data for the three cases is around 6.2%. It is computed based on equation **(Eq. II.29)**.

$$RMSE = \sqrt{\frac{\sum_{i=1}^{n}(\hat{\delta}_{fr,i} - \delta_{fr,i})^2}{n}} \times 100 \qquad \textbf{(Eq. II.29)}$$

where, n is the number of values. $\hat{\delta}_{fr,i}$, and $\delta_{fr,i}$ represents the i^{th} experimental and numerical values of frost thickness, respectively.

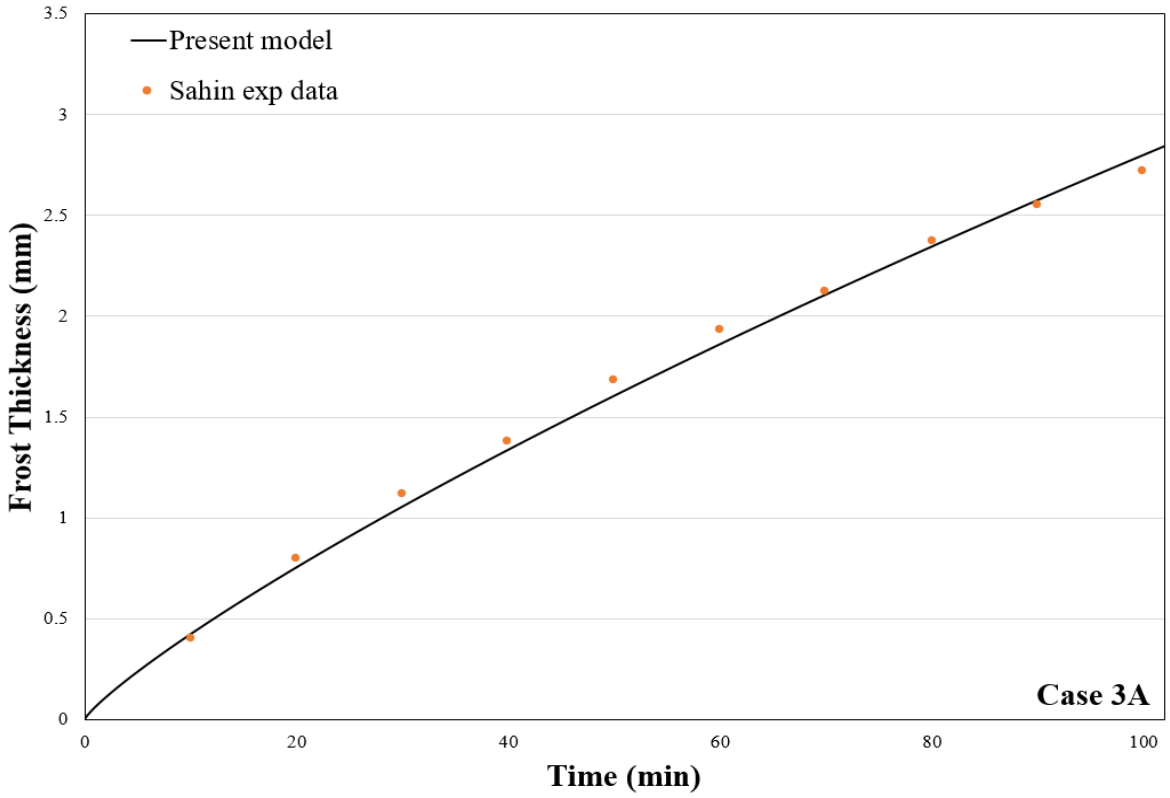

Figure II.6: Experimental and numerical frost thickness at T_{wall} = -15 °C, T_a =13 °C, ω_a = 0.0069 kg/kg, V_a = 2.18 m/s – Case 3A.

Regarding the evolution trends between the three cases, it appears that the model considers well the impact of air conditions and cold wall on the dynamic process of frost formation. As seen in **Figure II.4**, the frost thickness evolution is a little bit higher than in the case 2A represented in **Figure II.5**. This is due to high difference in wall temperature and air relative humidity between the two cases. While the air temperature was maintained constant, the wall temperature increases from -25 °C to -9 °C. As consequence, the higher gradient of temperature between the air stream and frost surface in case 1A leads to higher heat and mass transfer. This means that the frost growth in case 1A must be higher. However, an increase in the air relative humidity

from around 45% to 75% between case 1A and case 2A, respectively, will have the opposite effect. The influence of air relative humidity is easily understandable because, at the same air temperature, a higher relative humidity means higher quantity of water in the air and then higher quantity of water vapor freezes on the plate surface.

The influence of wall surface temperature on frost thickness formation could be deduced by comparing the evolution in **Figure II.5** and **Figure II.6**. For these two cases, the other parameters are kept constant. Experimental data provided by Sahin and the numerical simulation confirm that the lower the surface temperature, the thicker the frost layer. The results show that at 100 min, the frost thickness is 30% higher as the wall decreased by 6 K from -9 °C to -15 °C.

As can be observed in **Figure II.7**, the total mass flux transferred to the frost surface is 1.5 times higher in case 2A than case 1A. This means that the total mass flux from the air to the frost surface is highly sensitive to the inlet air relative humidity than wall temperature. The densification mass flux represents initially 18% and 26% of the total mass flux in case 1A and case 2A, respectively. This is due to the mass diffusion coefficient that decreases with low wall temperature. It means that lower temperature promotes water vapor desublimation at the frost surface. It can be also noticed that in case 2A the densification rate is decreasing over time following the growth rate trend. However, in case 1A, the rate of densification tends to increase

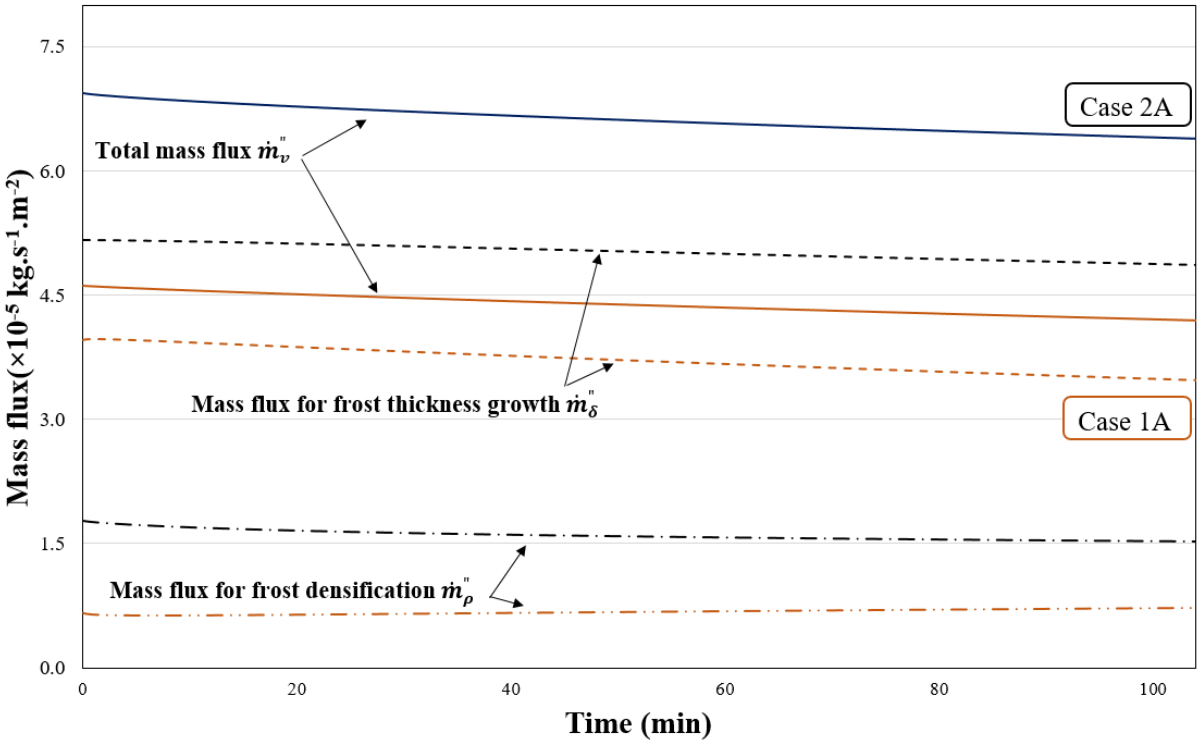

Figure II.7: Temporal variation of mass flux in case 1A and case 2A.

slightly over time. This is due to the surface temperature of frost that rises rapidly with the high thermal resistance of frost layer, thus, increasing the temperature difference between the cooling plate and the frost layer surface.

To clearly identify the impact of low wall temperature on frost properties, **Figure II.8** depicts the frost density for case 2A and case 3A, respectively. One can observe that within 100

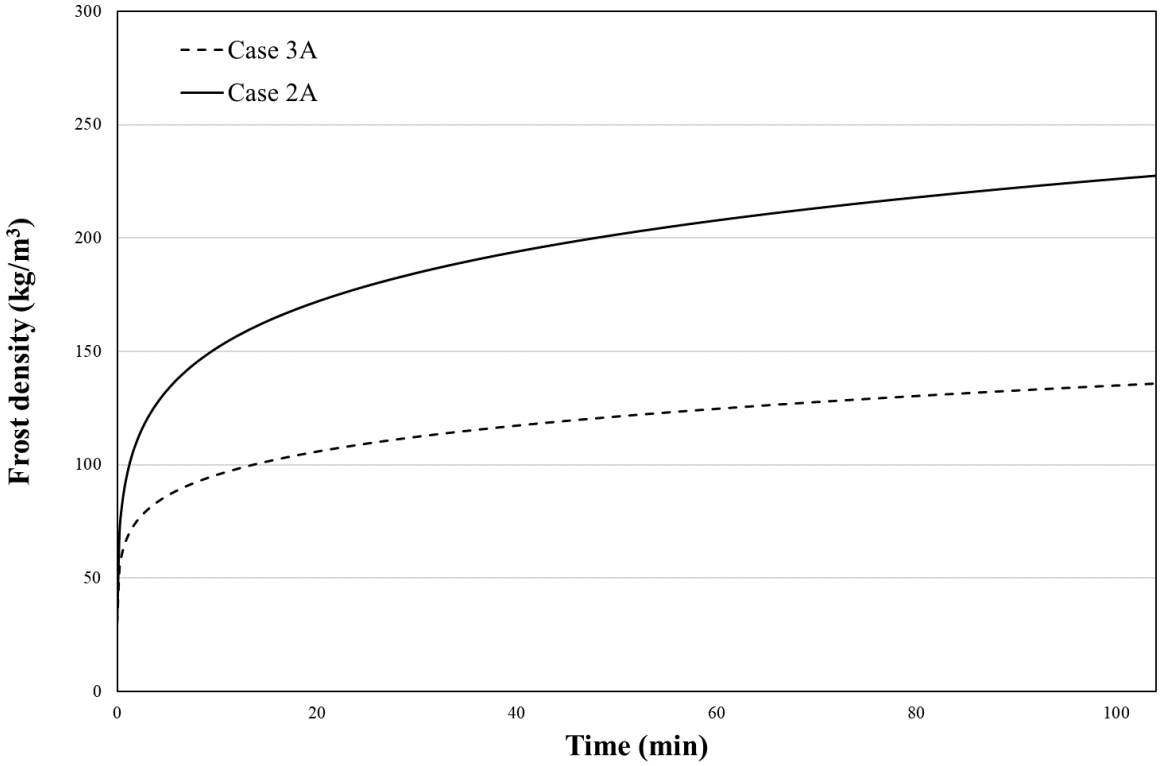

Figure II.8: Frost density versus time in case 2A and case 3A.

minutes, the frost density reaches around 230 kg/m^3 in case 2A against only 135 kg/m^3 in case 3A. When decreasing the wall temperature while keeping the other parameters constant, the mass flux leading to the thickness growth rises. These observations are consistent with previous reports [75], [171].

As it was already discussed in the previous chapter, the frost behavior and the frosting process are not the same in all applications and operating conditions. So, it is difficult to judge the accuracy of the present model under industrial freezing conditions. Largely for this reason, a second validation is involved using experimental data from the literature. At the author's knowledge, only one available study in the open literature has been performed on a simple plate in order to measure and predict the frost characteristics under operating conditions that are typical of many commercial freezers. In this study, Mao used a specific experimental airflow

loop, as shown in **Figure II.9**. The experimental methodology is described in Mao et al. [31] and briefly summarized next.

The airflow supplied from a cold environmental chamber 1 cooled to about -40 °C is mixed with air from the second test chamber cooled at about 0 °C and then passed over the test section. This latter is a cold base plate sized 600×2800 mm². The test conditions used for the experiments are reported in **Table I.1**. Twenty test conditions were used to develop 480 data samples for frost thickness, frost mass concentration, and heat flux through the cold plate. Each of these variables was measured directly as function of time and position. And both frost thickness and mass concentration were given at three equal times intervals.

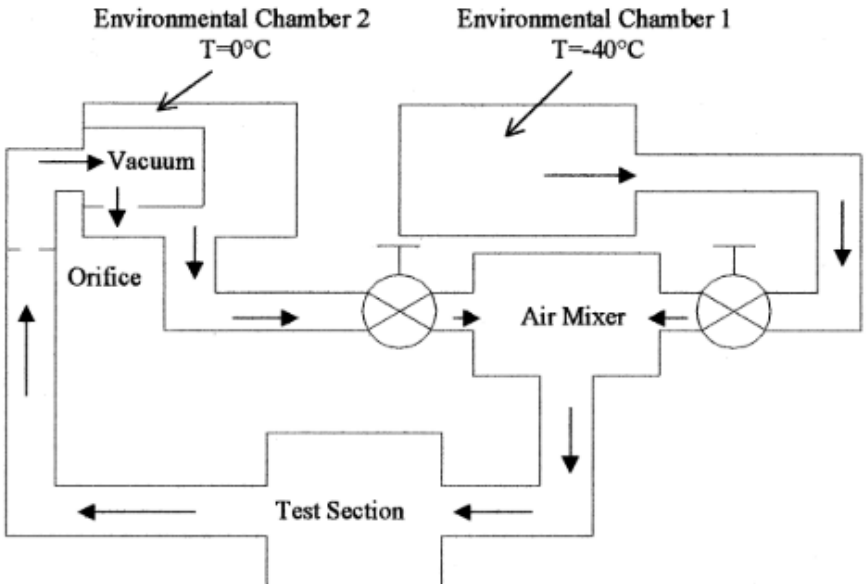

Figure II.9: Experimental setup, Mao et al. [31].

For validation, two cases were chosen from experimental data given by Mao. This choice is based on the closest industrial freezing conditions as reported in

Table II.4. In **Table II.5**, the simulation results at corresponding time intervals are represented. It is to note that, since the present model predicts average frost characteristics on the plate surface, the values reported by Mao in each position at the plate surface were averaged for each instant t.

Table II.4: Experimental operating conditions used for validation, from Mao et al. [31].

Experimental Conditions	**T_a (°C)**	**T_{wall} (°C)**	**ω_a(kg/kg)**	**Re**
Case 1B	-21.8	-40	4.9×10^{-4}	8,195

Case 2B	-24.3	-39.5	3.8×10^{-4}	13,112

As shown in **Table II.5**, simulation results match experimental values fairly well with a tolerable relative error rate that goes up to 8%. This means that this model is adequate for the industrial freezing conditions.

Table II.5: Experimental and numerical results for frost characteristics under freezing conditions, using data from Mao et al. [31].

	Time (s)	δ_{fr} **(mm)**	$\delta_{fr,predict}$ **(mm)**	**Relative error**	ρ_{fr} **(kg/m^3)**	$\rho_{fr,predict}$ **(kg/m^3)**	**Relative error**
Case 1B	1,800	0.74	0.71	4%	47.96	49.05	2%
	3,600	1.05	0.96	8%	48.64	51.53	5%
	5,400	1.35	1.24	8%	53.57	53.39	<1%
Case 2B	1,800	0.48	0.47	2%	68.90	65.70	4%
	3,600	0.71	0.67	5%	68.78	71.71	4%
	5,400	0.89	0.85	4%	75.21	72.64	3%

The experimental and numerical results confirm the evolution trends of the frost characteristics and the nature of frost that can be encountered in such industrial freezing application. At very low air and wall temperatures, at high air velocity and relative air humidity, frost has a low density and could therefore have a greater thermal resistive effect than that encountered in other applications, in particular heat pumps. The mass flux of densification in both case 1B and case 2B does not exceed 12% of the total mass flux. However, experimental and numerical studies in the literature have reported that the densification flux may represent more than 40% of the total mass flux, and therefore the frost density may vary from 150 to 300 kg/m^3 after one hour of frosting under heat pump conditions [59], [172].

It should be clarified that this present model may be much better in frost growth predictions in freezers than heat pump or air conditioning systems. In the latter, and after a few hours of operation, the frost formed imposes a thermal resistance that increases frost surface temperature. If this temperature exceeds 0 °C, the frost on the surface begins to melt. A part of this condensate will diffuse inside and increase the frost layer density. The other part may drain off especially if the surface is vertical (gravity effect). This type of phenomenon is not yet taken

into consideration in the available frost models in the literature knowing that it often happens in heat pump conditions. However, under freezing conditions, and due to the low temperatures, this phenomenon of frost surface heating-melting-condensate diffusion, is strongly unachievable.

B. Validation on a finned tube heat exchanger:

The finned tube heat exchanger, in TIL library, is modeled by a finite volume approach. Each flow is discretized on a large number of finite volume elements called cells containing mass, energy and momentum balance equations. When connecting the finite volume elements, the flow configuration is an option to design different types of heat exchangers. In fact, the air connections allow having parallel, counter, and cross-flow heat exchanger configuration. **Figure II.10**, shows an example of the structure of a counter flow heat exchanger.

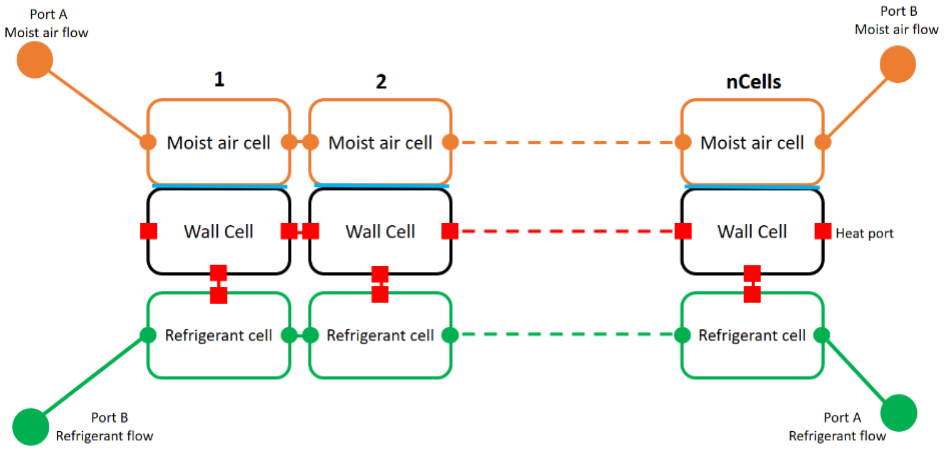

Figure II.10: Cells basic element for the finned tube heat exchanger.

In our case, three types of cells are combined: a refrigerant cell, a wall cell, and a moist air cell.

Note that the moist air cell and the wall cell are merged in one cell called the moist air cell that considers condensation and evaporation, using a dynamic mass and energy balance of a water film.

- *Refrigerant element*

Equations of energy **(Eq. II.30)** and mass conservations **(Eq. II.31)** are integrated in the refrigerant volume element. The conservation of momentum is not used because the pressure losses in the channels are negligible.

$$V \times \left(\rho \frac{\partial h}{\partial t} - \frac{\partial P}{\partial t}\right) = \dot{m}_{In,ref} h_{In,ref} + \dot{m}_{Out,ref} h_{Out,ref} + \dot{Q}_{ref} \qquad \textbf{(Eq. II.30)}$$

$$\boldsymbol{V \times \left(\frac{\partial \rho}{\partial t}\right) = \dot{m}_{In} + \dot{m}_{out}} \qquad \textbf{(Eq. II.31)}$$

Where $\dot{m}_{In}$ and $\dot{m}_{out}$ are the inlet and outlet mass flow rate, respectively. $h_{In,ref}$ and $h_{Out,ref}$ are the inlet and outlet refrigerant specific enthalpy, respectively. $\dot{Q}_{ref}$ is the refrigerant heat transfer rate.

- *Air element*

(Eq. II.32), **(Eq. II.33)** and **(Eq. II.34)** are respectively equation of energy, mass and momentum conservation on the air side.

$$\boldsymbol{\dot{Q}_a + \dot{m}_{In,a} h_{In,a} + \dot{m}_{Out,a} h_{Out,a} = 0} \qquad \textbf{(Eq. II.32)}$$

$$\boldsymbol{\dot{m}_{In,a} h_{In,a} + \dot{m}_{Out,a} h_{Out,a} - \dot{m}_v = 0} \qquad \textbf{(Eq. II.33)}$$

$$\boldsymbol{p_{In,a} - p_{Out,a} = \Delta p} \qquad \textbf{(Eq. II.34)}$$

Where $p_{In,a}$ and $p_{Out,a}$ are the inlet and outlet air pressure, respectively. Δp is the air side pressure drop.

In the energy and momentum equation of refrigerant and moist air wall cell; heat transfer and pressure drop models are needed to compute the heat flow rate and the friction pressure drop.

The heat flow rate $\dot{Q}$ is calculated from:

$$\boldsymbol{\dot{Q} = \alpha A (T_{cell} - T)} \qquad \textbf{(Eq. II.35)}$$

Where α is the heat transfer coefficient, A is the cell heat transfer area, T represents the frost surface temperature for the air side and the heat port temperature for the refrigerant side, and T_{cell} is the temperature in the control volume (cell).

The pressure drop Δp is calculated from:

$$\boldsymbol{\Delta p = \zeta \left(\frac{\rho}{2}\right) V^2} \qquad \textbf{(Eq. II.36)}$$

where ζ is friction factor, ρ is the medium density, and V is the medium velocity.

On the refrigerant side a heat transfer and pressure drop models are determined in order to compute α and ζ, respectively.

On the air side, both heat transfer and pressure drop models are determined then an effective heat transfer coefficient is derived from α_a in order to avoid the calculation of a mean temperature.

The effective heat transfer coefficient is computed as follows:

$$\boldsymbol{\alpha_{A,eff} = \dot{m}_a C_{p,a}\left(1 - e^{-\frac{\alpha_a \times (A_t + \eta_f A_f)}{\dot{m}_a C_{p,a}}}\right)} \qquad \textbf{(Eq. II.37)}$$

Where A_t is the external area of tube surfaces and A_f is the external area of fin surface and η_f is the fin efficiency.

Then the sensible flux defined in equation **(Eq.II.3)** for a plat plate is computed for a finned tube heat exchanger as:

$$\dot{Q}_s'' = \frac{\dot{m}_a C_{p,a}\left(1 - e^{\frac{-\alpha_a (A_t + \eta_f A_f)}{\dot{m}_a C_{p,a}}}\right)}{A_t + A_f}\left(T_{a,in} - T_\delta\right) \qquad \textbf{(Eq.II.38)}$$

And the mass flux of water vapor transported from the air stream to the frost surface is determined via:

$$\dot{m}''_v = \frac{\dot{m}_a\left(1 - e^{\frac{-\alpha_a (A_t + \eta_f A_f)}{\dot{m}_a C_{p,a}}}\right)}{A_t + A_f}\left(\omega_{a,in} - \omega_{\delta,sat}\right) \qquad \textbf{(Eq. II.39)}$$

The total heat flux is then calculated as follows:

$$\dot{Q}_a'' = \dot{Q}_s'' + \dot{m}''_v L_{sv} \qquad \textbf{(Eq. II.40)}$$

Regarding the wall cell, a thermal capacity of a solid mass is calculated based on material and geometry data.

The determination of the frost characteristics over time is made following the same calculation process as with the flat plate. In each time interval, the frost thickness and frost density are determined. Then, the insulating effect on the fins caused by the additional thermal heat resistance of the frost R_{fr} is taken into consideration in the balance equations. In addition, the frost effect on convective heat transfer coefficient, on airflow velocity and on pressure drop is

taken into consideration by generating a cross sectional area (S) and heat transfer area (A) variation factors as outputs. These outputs are forwarded to the heat and pressure drop models.

The cross section area reduction factor, for each control volume, is computed as follow:

$$\boldsymbol{F_{cross} = 1 - \frac{V_{fr}}{V_{c,a}}} \qquad \textbf{(Eq. II.41)}$$

where V_{fr} is the frost volume computed as the ratio of the mass and density of the frost layer, and $V_{c,a}$ is the air cell volume.

The cell volume in the air side is computed as:

$$\boldsymbol{V_{c,a} = V_{f,T} \times Void} \qquad \textbf{(Eq. II.42)}$$

where $V_{f,T}$ is the total finned volume computed as the total volume of the heat exchanger (Height × Width × Depth) and Void is the void ratio illustrated in **Figure II.11** and computed as:

$$\boldsymbol{Void = 1 - \frac{\delta_f}{P_f} - \frac{\pi {d_{ext}}^2 \times (P_f - \delta_f)}{4 S_L S_T \times P_f}} \qquad \textbf{(Eq. II.43)}$$

$$\boldsymbol{Void = \frac{(P_f - \delta_f) S_L S_T - \frac{\pi}{4} {d_{ext}}^2 \times (P_f - \delta_f)}{S_L S_T \times P_f}} \qquad \textbf{(Eq. II.44)}$$

where d_{ext} is the external diameter of tubes, P_f and δ_f are the fin pitch and fin thickness, respectively. S_L and S_T are the transversal and longitudinal spacing between two adjacent tubes, respectively.

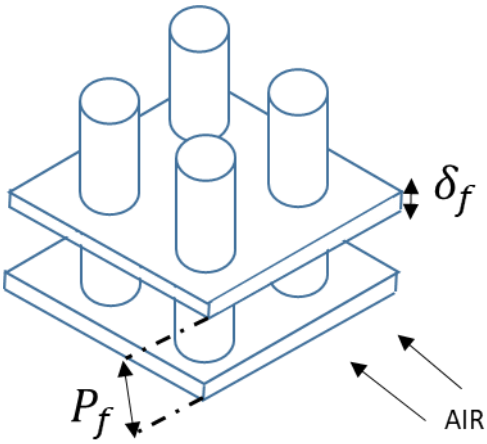

Figure II.11: Schematic representation of the void ratio of a finned tube heat exchanger.

The first two terms in the right side of the **(Eq. II.43)** represent the volume between two fins. The third term is the volume of the tube portion limited by two fins. Subtracting the two terms, we find the free volume where the air could flow, and thus the free volume ratio **(Eq. II.44)**. The denominator reflects the total volume between two fins (solid and fluid). Once the cross section area variation factor is determined, the heat transfer area variation factor can be deduced as follow:

$$A_{Heat} = \sqrt{A_{cross}} \qquad \textbf{(Eq. II.45)}$$

The flow cross-sectional area is formulated by a simplified view of a portion of the heat exchanger as a triangle and the corresponding heat transfer area is determined using the similarity theorem of triangles, as suggested by Westhäuser et al. [173] As shown in **Figure II.12**.

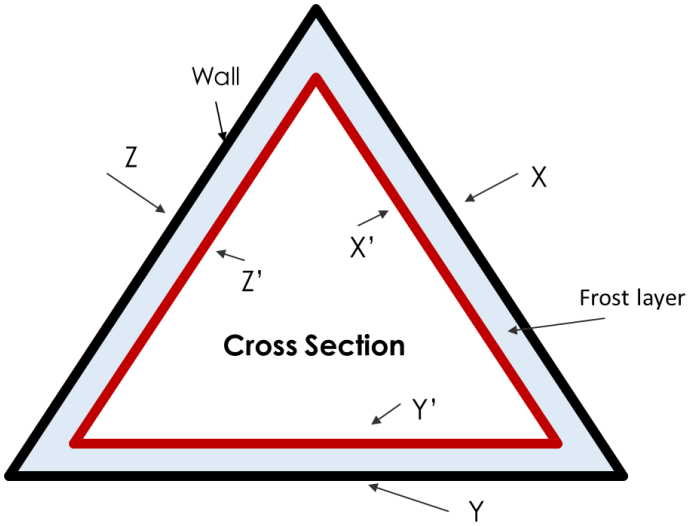

Figure II.12: Simplified front view of a frosted finned tube heat exchanger.

$$\frac{X}{X'} = \frac{Y}{Y'} = \frac{Z}{Z'} = k \qquad \textbf{(Eq. II.46)}$$

And

$$\frac{A_{cross}}{A_{cross,red}} = k^2 \qquad \textbf{(Eq. II.47)}$$

To accomplish the validation of the frost model in complex geometry, the experimental data used are those reported by Padhmanabhan et al. [174] The latter have conducted laboratory frosting tests on a small 300×300 mm one-row finned tube coil, which geometry is given in

Table II.6. The test facility consisted of a closed loop wind tunnel where the air temperature and humidity were maintained. A refrigeration loop was used to provide cold glycol (50/50) on the test coil. A centrifugal fan was used to circulate air and maintain the airflow constant during frost growth.

Table II.6: Finned tube heat exchanger geometric data used for frost model validation [174].

Geometric parameter	Value
Finned length (mm)	305
Coil height (mm)	305
Coil depth (mm)	22.1
Fin density (fins/m)	630
Fin thickness (mm)	0.1
Tube pitch (mm)	25.4
Number of rows	1
Number of tubes/row	12
Number of circuits	12
Internal tube diameter (mm)	10.06
Tube thickness (mm)	0.3

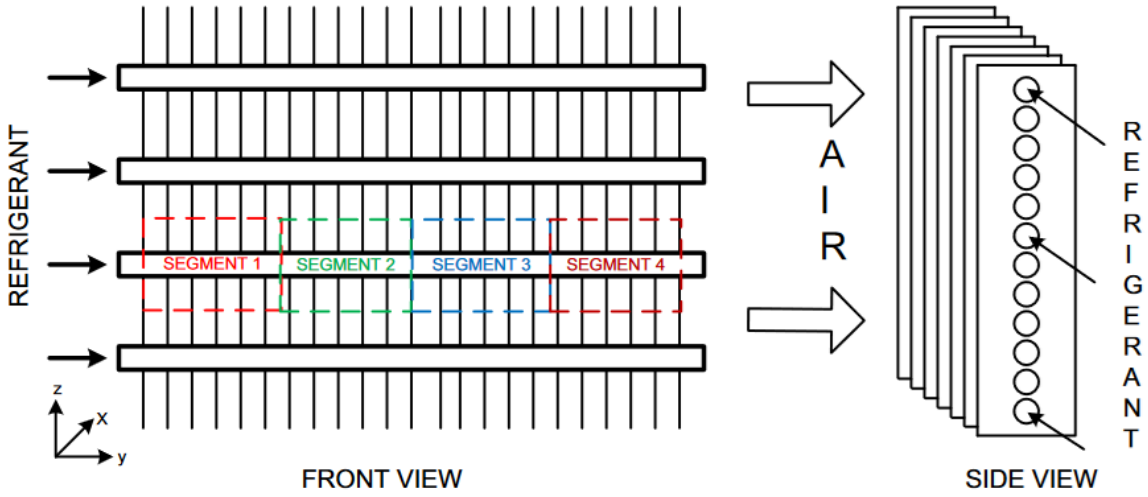

Figure II.13: Schematic view of the discretization for the finned tube heat exchanger reported by. Padhmanabhan et al. [174].

The authors have developed a segments-by-segments heat exchanger model and thus measured the frost thickness for each segment of a tube, as shown in **Figure II.13**. Since, this kind of discretization could not be adopted by the present model, the reported values by Padhmanabhan et al. [174] have been averaged.

To complete the model, we have selected the heat transfer and pressure drop correlations. For the refrigerant side, the pressure drop is assumed to be zero, and the internal heat transfer coefficient is calculated using the correlation provided by Shah and London [175]. For air side, we have selected the heat transfer and pressure drop correlations based on the work of von Haaf [176] that were also used by Tegethoff [177] and Schmidt [178].

The Haaf correlation is designed for geometries with both staggered and aligned tubes. The geometry is characterized by the use of an equivalent hydraulic diameter (d_h) equivalent and the distance of the tubes. The correlation is developed with moist air and allows the determination of Nusselt number as follow:

$$\boldsymbol{Nu = 0.31 Pr^{0.333} Re^{0.625} \times \left(\frac{d_h}{S_L}\right)^{1/3}} \qquad \textbf{(Eq. II.48)}$$

And the friction factor ξ used for the pressure drop correlation is computed as follow:

$$\boldsymbol{\xi = 10.5 Re^{-1/3} \times \left(\frac{d_h}{\rho}\right)^{0.6}} \qquad \textbf{(Eq. II.49)}$$

Then the total pressure drop is calculated using the following relation:

$$\boldsymbol{dP_T = N_s \times \xi \times \frac{S_L}{d_h} \times \frac{\rho}{2} \times V_a{}^2} \qquad \textbf{(Eq. II.50)}$$

where V_a is the average velocity of the gas and N_s is the number of serial tubes.

Non isothermal fins are considered by a fin efficiency calculated by Schmidt model [178] considering the geometry and the heat transfer coefficient obtained from the heat transfer model. Under the conditions of a rectangular plate fin, the following expression is given by Schmidt:

$$\boldsymbol{\eta_f = \frac{\tanh(X)}{X}} \qquad \textbf{(Eq. II.51)}$$

η is the fin efficiency, X is given by:

$$\boldsymbol{X = H_{eff} \sqrt{\frac{2\alpha_a}{k_f \delta_f}}} \qquad \textbf{(Eq. II.52)}$$

[1]where H_{eff} is the effective fin height computed by:

$$\boldsymbol{H_{eff} = 0.5\, d_{ext}(r-1)(1+0.35\ln(r))} \qquad \textbf{(Eq. II.53)}$$

r is a dimensionless diameter ratio computed by:

$$\boldsymbol{r = \frac{1.27 S_T}{d_{ext}} \sqrt{((0.25 + (\frac{S_L}{S_T})^2)^{0.5} - 0.3)}} \qquad \textbf{(Eq. II.54)}$$

For wet conditions, correction factor was introduced by Sharqawy [179][1].

$$\textbf{Correction factor} = (1 + (\frac{dP}{dT} \times \frac{1}{P}) \times 0.622 \times \frac{h_v - h_l}{C_a})^{\frac{1}{2}} \qquad \textbf{(Eq. II.55)}$$

where $\frac{dP}{dT}$ is the rate of increase in vapor pressure per unit increase in temperature given by the Clausius Clapeyron equation:

$$\boldsymbol{\frac{dP}{dT} = \frac{h_v - h_l}{(v_v - v_l).T}} \qquad \textbf{(Eq. II.56)}$$

Where P is the saturation vapor pressure, $h_v - h_l$ is the latent heat of evaporation, and $v_v\ and\ v_l$ are the specific volumes at temperature T of the vapor and liquid phases, respectively.

The fin efficiency in wet conditions becomes:

$$\boldsymbol{\eta_f = \frac{\tanh\,(X \times \text{correction factor})}{X \times \text{correction factor}}} \qquad \textbf{(Eq. II.57)}$$

In our case the correction factor is equal to 1 since there is not water film formed. However, the fin efficiency in **(Eq. II.44)** can be modified by incorporating the thermal resistance of the frost layer in the air side heat transfer coefficient, as suggested by Sanders [180].

[1] The use of Sharquawi's model (liquid-vapor) for frosting seems questionable but these elements are reported in order to be transparent with the presented results. This term did not prevent the validation of the model.

The fin parameter X defined in dry conditions is modified as follows:

$$X = H_{eff}\sqrt{\frac{2\alpha_o}{k_f \delta_f}} \qquad \textbf{(Eq. II.58)}$$

Where:

$$\alpha_o = \left(\frac{1}{\alpha_a} + \frac{\delta_{fr}}{k_{fr}}\right)^{-1} \qquad \textbf{(Eq. II.59)}$$

This modification of the fin parameter X was also suggested and used by Kondepudi et al. [181].

Finally, for simulation, the heat exchanger coil has been discretized on only one cell on each flow side.

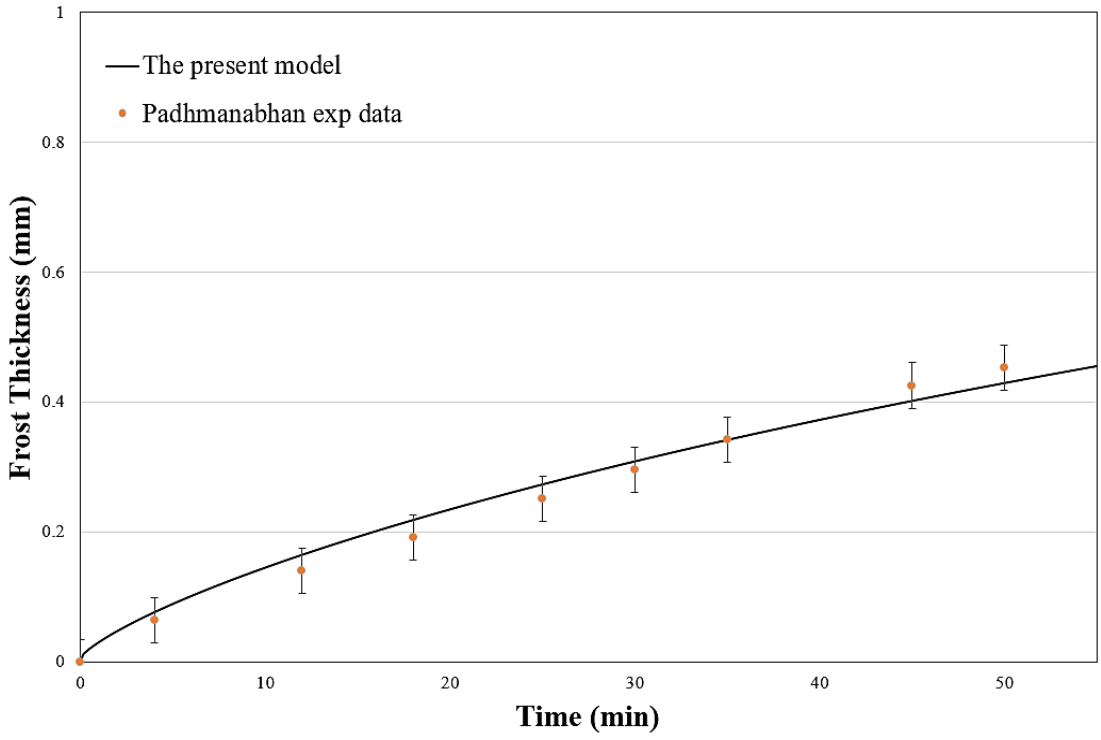

Figure II.14: Measured and simulated frost thickness at V_a = 0.96 m/s, T_{ref} = -22.8 °C, RH = 82%, T_a = 1.7 °C.

As shown in **Figure II.14**, comparisons of the model with experiments shows good agreement. This means that the frost sub-model developed in the present chapter, and the frost properties outputs forwarded to the heat exchanger sub-model are appropriately connected.

II.4. **Summary:**

The frost numerical model based on energy and mass conservation equations detailed in this chapter is implemented using Modelica langage and Dymola software on Thermal Systems Library. Although the frosting process is a transient one, the model is quasi-steady; that is, the process is divided into time steps and within each step, the process is assumed to be at steady-state.

The model is first validated using experimental data from the literature reported for a frost layer formed on cold flat plate and those under both heat pump and freezing conditions.

Thereafter, the model is introduced on a heat exchanger model. The whole model is then considered by Modelica language as two sub-models: frosting sub-model and a heat exchanger sub-model. Data of correlations of fin efficiency, air and refrigerant heat transfer coefficient and pressure drop according to heat exchanger were defined. The model takes all of the evaporator coil geometries and the inlet air and refrigerant thermal properties as the required user input. Then it calculates all the physical and thermal properties of the air and refrigerant at each control volume of the evaporator coil. The frost properties (e.g., frost thickness, thermal conductivity and density) at the end of each time step are used as an input for the next time step.

The simulation results show that the present model is suitable for most conditions and geometries and could therefore be introduced into an evaporator model of an industrial freezer.

CHAPTER III

Numerical and experimental study of an industrial freezer under frosting conditions

CHAPTER III: Numerical and experimental study of an industrial freezer under frosting conditions

III.1. Evaporator model

The evaporator of the freezing system is an overfeed coil that refers to the practice of delivering a greater rate of liquid refrigerant to the evaporator than the rate that actually evaporates. Liquid overfeed is common in such large-scale industrial freezing systems. The major benefit of this liquid recirculation is the improvement of the heat transfer coefficient in the evaporator. In fact, in the case of dry expansion systems, a part of the heat exchanger area can be affected by dryout conditions and a further tube length is dedicated to the superheating of the vapor. Both dryout and superheating regions are characterized by low values of the heat transfer coefficients compared with the heat transfer coefficient than can be achieved during boiling. The improvement of evaporator heat transfer capabilities by liquid overfeeding is due to the absence of dryout phenomena, no need of superheating and higher refrigerant velocity inside the tubes. Moreover, feeding the evaporator with liquid only can also improve the refrigerant distribution. However, there are also some disadvantages in such a practice: large quantity of the refrigerant in the system, and the additional power required for the refrigerant pumps. The externally driven mechanical pump is used to provide the necessary liquid recirculation effect so that the ammonia exits the evaporator with a low vapor quality. In this case, the overfeed ratio, defined as the mass ratio of the liquid pumped to the evaporator to the amount of vaporized liquid in the evaporator, is equal to 4. The outlet ammonia vapor quality is around 25%.

The freezer evaporator modeled is a circular tube parallel cross flow heat exchanger. The plain fin has a thickness of 0.2 mm and the fin density is progressive in the direction of airflow. The evaporator is 3,000 mm length, 1,620 mm wide and 925 mm deep. As shown in **Figure III.1**, the ammonia refrigerant supplies 2 parallel circuits of NH_3. Each circuit is composed of 8 serial tubes and 28 parallel tubes (8 passes and 28 rows). The evaporator has therefore 56 parallel hydraulic flows. To model this geometry, we used the finned tube heat exchanger model of TIL library previously described in **chapter II** with the same correlation at the air side. For the refrigerant side, a constant heat transfer coefficient of 2000 $W.m^{-2}.K^{-1}$ is assumed since it has been shown that the heat transfer coefficient is almost constant at the refrigerant mass fluxes lower than 120 $kg.m^{-2}.s^{-1}$ and vapor quality lower than 30%. It is to note that the heat exchanger geometry of TIL library doesn't take into consideration this sort of tube arrangements and

progressive fin pitch of the present evaporator. For this reason, the freezer evaporator geometry was decomposed into 11 serial evaporators modeled by the TIL heat exchanger.

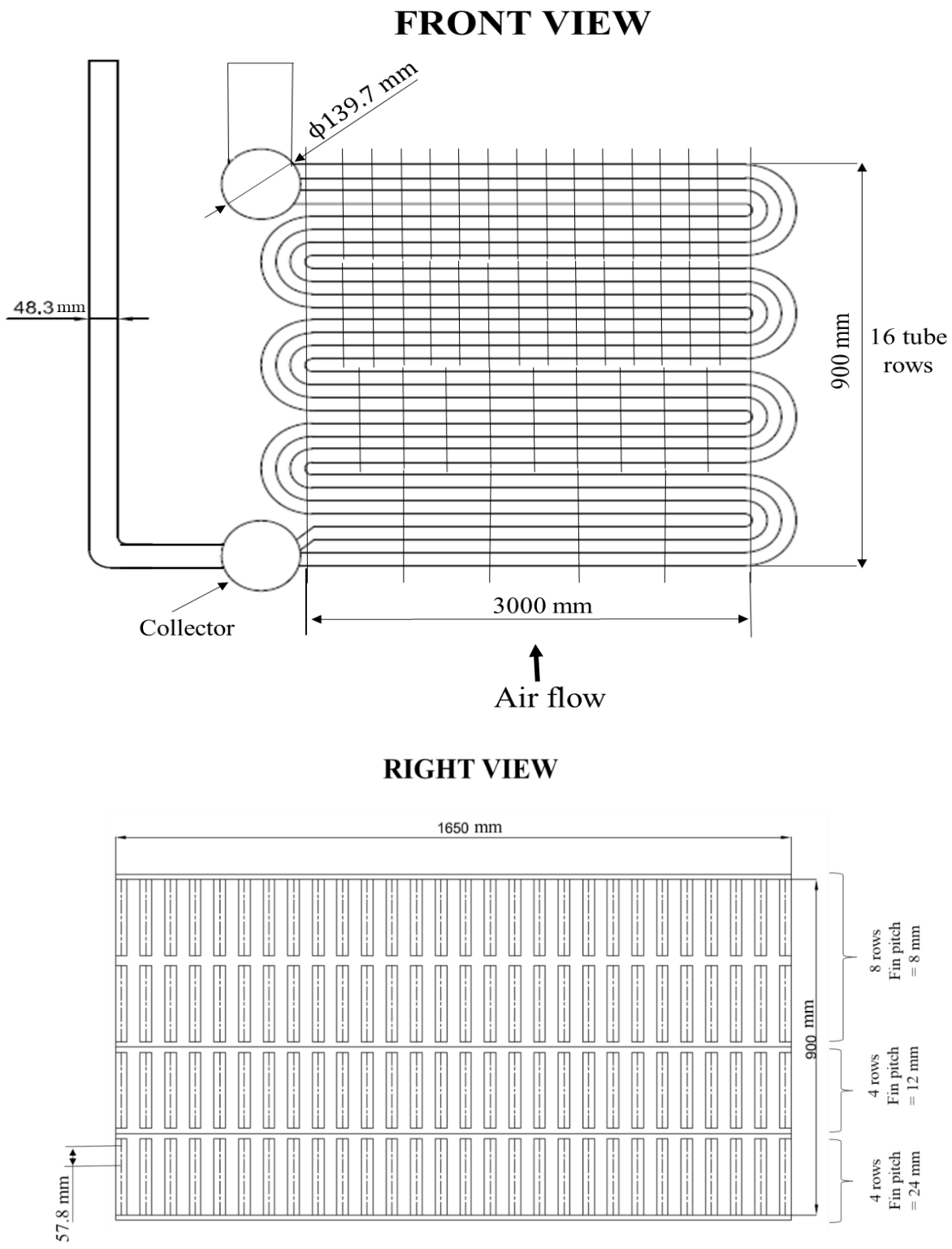

Figure III.1: Schematic presentation of evaporator geometry of the freezing system.

III.2. **Fan model**

The fan evaporator is modeled by a second order model existing in the TIL library. This choice is justified by the fact that this model takes into account the change in volume flow rate of the fan based on a characteristic curve of the manufacturer. The characteristic curve of the fan mainly defined by a pressure drop, a nominal speed and a nominal volume flow and other parameters. Then, the actual fan operation point is found using the affinity laws. In our case, the fan used is the Woods® axial fan 48J ½, made with an 20° pitch angle, turning at a fixed 50 Hz frequency and has a maximal fin efficiency of 82%. The characteristic curve is defined by the following equations:

For $\dot{V} < \dot{V}_{tr}$:

$$\boldsymbol{\Delta p = C_2 \dot{V}^2 + C_1 \dot{V} + \Delta p_0} \qquad \textbf{(Eq. III.1)}$$

For $\dot{V} > \dot{V}_{tr}$:

$$\boldsymbol{\Delta p = (\dot{V} - \dot{V}_{tr})(2 C_2 \dot{V}_{tr} + C_1) + \dot{V}_t (C_2 \dot{V}_{tr} + C_1) + \Delta p_0} \qquad \textbf{(Eq. III.2)}$$

Where Δp is the static pressure drop, $\dot{V}$ is the air volume flow rate, and $\dot{V}_{tr}$, C_1, C_2 and Δp_0 are constant parameters defined to fit the real constructor characteristic curve. **Table III.1** summarizes all the parameters used to define the evaporator fan:

Table III.1: Evaporator fan parameters.

Parameters	**Value**
Nominal pressure drops (Pa)	250
Nominal air volume flow rate (m^3/s)	21.16
Initial fan efficiency (%)	61
$\boldsymbol{\dot{V}_{tr}}$ **(m^3/s)**	13.11
$\boldsymbol{C_1}$	11.72
$\boldsymbol{C_2}$	-1.14
$\boldsymbol{\Delta p_0}$	516

The hydraulic power transmitted to the air is computed as:

$$\boldsymbol{\dot{W}_{hyd} = \Delta p \times \dot{V}} \qquad \textbf{(Eq. III.3)}$$

The shaft power is therefore computed using the fan efficiency:

$$\dot{W}_{shaft} = \frac{\dot{W}_{hyd}}{\eta_{fan}} \qquad \textbf{(Eq. III.4)}$$

The fan efficiency is determined considering electrical, aerodynamic and mechanical losses defined as function of the air volume flow rate and empirical coefficients.

To compute the exist air properties, the following energy balance equation is applied:

$$h_{a,s} = h_{a,e} + \frac{\dot{W}_{shaft}}{\dot{m}_a} \qquad \textbf{(Eq. III.5)}$$

where $h_{a,e}$ and $h_{a,s}$ are the inlet and exist air specific enthalpy, respectively.

It is to note that depending on the type of fan, centrifugal or axial, the fan curve could be different. As shown in **Figure III.2**, the characteristic curve of a centrifugal fan starts from zero flow and increases until reach a maximal. Then, it decreases when the flow continues to increase. However, for an axial fan, we could have first the same type of evolution but at very low flow, there is a zone called instability zone.

Since it is complex to express this effect by the quadratic and linear function combined in the actual model, the fan curve characteristic developed were similar to the constructor curve only on the operating zone. Beyond that, the simulation has been programmed to stop at this critical point which represents the minimum airflow (maximal fan pressure).

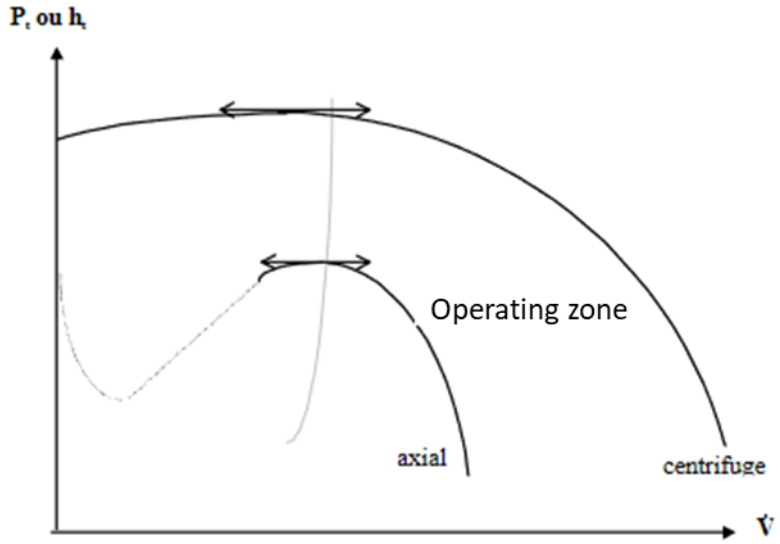

Figure III.2: Axial and centrifuge fan operating zones

III.3. **Compressor model**

For this industrial ammonia systems, the compressor type used is a screw compressor with a fixed speed and variable capacity. The capacity is regulated using a slide valve. As illustrated in **Figure III.3**, when the slide valve is opened, a portion of the gas inside the compressor is vented back to the suction port. This provides regulation down to 10% of full capacity. This type of regulation is easy but it affects the compressor efficiency.

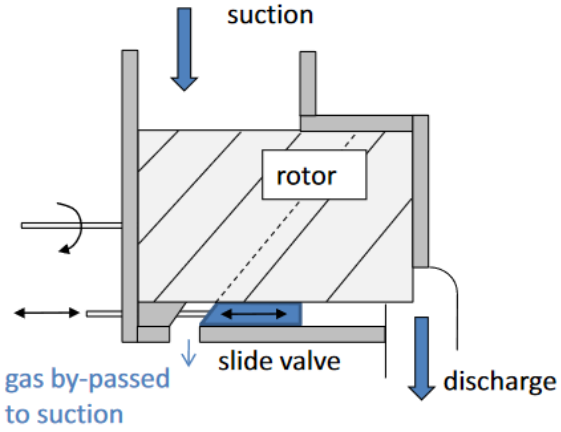

Figure III.3: Screw compressor with slide valve.

To model this type of compressor, a model inspired from Liu et al. [182] is developed. It consists of predicting the compressor volumetric efficiency as function of pressure ratio and other variables detailed in equation **(Eq. III.6**).

$$\eta_v = a\tau^{\frac{1}{k}}\tau^{-1} + (b + c\tau^{-1})\tau^{\frac{1}{2k}}\sqrt{2v_1(p_2 - p_1)} \qquad \textbf{(Eq. III.6)}$$

where, τ is the ratio of the discharging pressure and the suction pressure, k is the polytropic index, and a b and c are coefficients obtained through constructor data regression.

Since the relation between the slide position and the swept volume is not linear (**Figure III.4**), a correcting factor is used to predict the volumetric efficiency for part-load conditions. Therefore, the volumetric efficiency can be calculated with equation **(Eq. III.7**).

$$\eta_v = \eta_{v\,100\%} f(S_{vp}) \qquad \textbf{(Eq. III.7)}$$

where, $\eta_{v\,100\%}$ is the full load volumetric efficiency, $f(S_{vp})$ is a correcting polynomial of degree 5 expressed as function of valve slide position. It is determined to fit with measured data. This factor is expressed by polynomial equation of degree 5 according to the constructor data. Doing this, the sucked vapor mass flow rate is deduced.

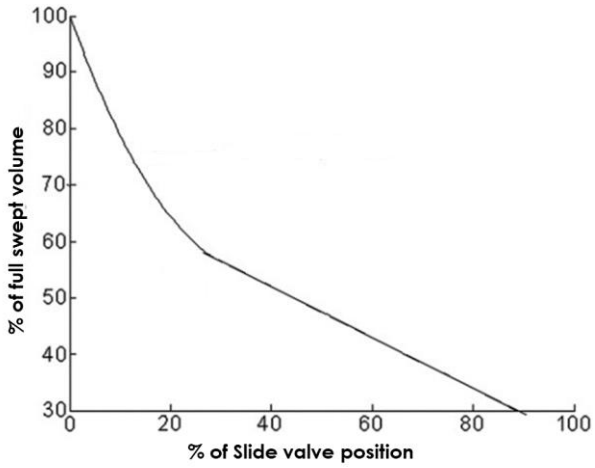

Figure III.4: Example of relationship of slide valve position and swept volume.

To calculate the power transferred to the ammonia during compression, the following equation is used:

$$\dot{W}_c = \frac{p_1 \dot{V}_1}{k-1}\left[{V_i}^{k-1} + \frac{\tau}{V_i}(k-1) - k\right] \qquad \textbf{(Eq. III.8)}$$

where, $\dot{V}_1$ is the sucked vapor volume flow rate and V_i is the built-in volumetric ratio or volume index fixed at 3.6 for both high and low pressure compressors. It refers to the ratio of suction volume divided by discharge volume. Finally, a deviation between the compressor shaft power and the power transferred to the ammonia is taken into consideration. This deviation arises from oil-gas heat transfer and from friction losses. The full-load capacity of the oil cooler is given by the manufacturer. For part-load conditions, a valve slide position function is regressed with constructor data to fit shaft power data given by the constructor for each slide valve position. And by applying the energy balance equation expressed in equation **(Eq. III.9**), a fitted polynomial of degree 2 is found expressing the capacity of the oil-cooler ($\dot{Q}_{oil}$) as function of valve slide position. **Figure III.5** and **Figure III.6** show the part-load shaft power comparison between the model and the manufacturer data, for HP and LP compressor, respectively. From the figures, it can be seen that the most of the error between the predicted and the tested are within 2%.

$$\dot{W}_c + \dot{W}_{shaft} + \dot{Q}_{oil} = 0 \qquad \textbf{(Eq. III.9)}$$

where the oil-cooler capacity at part-load conditions is computed as follows:

$$\dot{Q}_{oil} = a_1 + a_2 S_{vp} + a_3 {S_{vp}}^2 \qquad \textbf{(Eq.III.10)}$$

Where a_1, a_2 and a_3 are constant coefficients calculated using the manufacturer data.

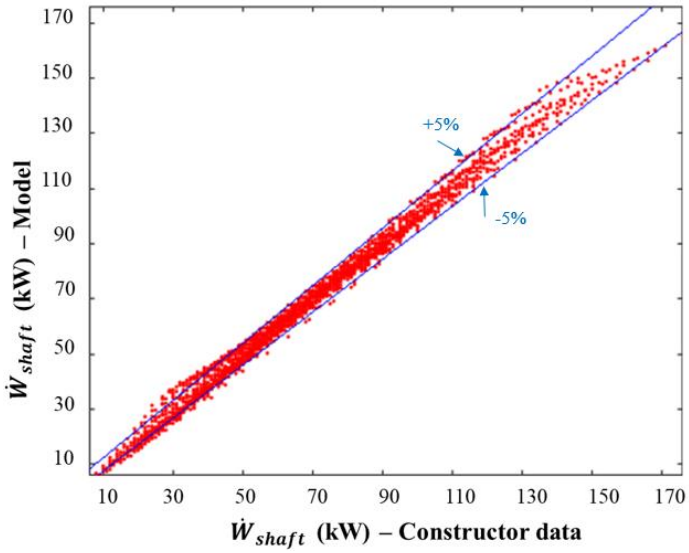

Figure III.5: Comparison between compressor shaft power between the model and constructor data for HP Compressor.

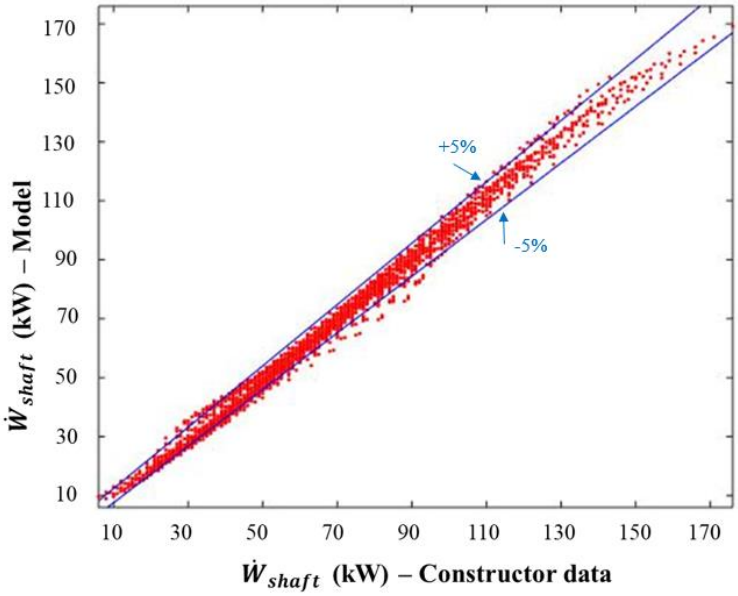

Figure III.6: Comparison between compressor shaft power between the model and constructor data for LP Compressor.

The key design and input model parameters of the LP and HP compressors are listed in **Table III.2**.

Table III.2: Key parameters for the LP and HP compressors.

Parameters	**LP Compressor**	**HP Compressor**
Speed (Hz)	50	50
Swept volume (m^3/h)	639	237
Volume index V_i	3.6	3.6
Polytropic index *k*	1.31	1.31
Condensation temperature range (°C)	[-20, 20]	[27, 45]
Evaporation temperature range (°C)	[-50, -34]	[-20, -4]
Coefficients a, b, and c	$-3, -3\times10^{-5}, -2\times10^{-2}$	$-4\times10^{-1}, -6\times10^{-6}, -1\times10^{-3}$
Coefficients of $f(S_{vp})$	$-1\times10^{-1}, 5\times10^{-1}$, -3, 15, -28	-1, 3, -11, 22, -20, 7
a_1, a_2, a_3	7, 17, 7	$9, 7\times10^{-1}$, 47

III.4. **Tank model**

The separator model used is the TIL tank model. The separator is considered as one control volume and modeled considering a separation of the refrigerant at the inlet port into a liquid and a gas phase. The outlet conditions for the gas and liquid are calculated estimating an ideal separation. The separator model bases on an ideally mixed volume, whose enthalpy and density variation are calculated by a transient energy and mass balance expressed given in **(Eq.III.11**) and **(Eq.III.12)**, respectively.

$$\boldsymbol{V \times \left(\rho \frac{\partial h}{\partial t} - \frac{\partial p}{\partial t}\right) = \dot{m}_{In}(h_{IN} - h) + \dot{m}_{Out}(h_{Out} - h)} \qquad \textbf{(Eq.III.11)}$$

$$\boldsymbol{V \times \left(\frac{\partial \rho}{\partial t}\right) = \dot{m}_{In} + \dot{m}_{Out}} \qquad \textbf{(Eq.III.12)}$$

(Eq.III.11) describes the time derivative of density within the accumulator. Note that the time derivative of pressure is provided as an input to the model. The outlet enthalpy depends on the quality of the entering fluid, the specific enthalpy in the accumulation and the filing level.

The filling level of the separator is derived from the enthalpy of the volume, considering the specific enthalpy *h* and density ρ of the mixture, the liquid phase and the vapor phase, following the equation below:

$$FL = \frac{V_l}{V} = \frac{\rho}{\rho_l}(1 - q) = \left(\frac{\rho}{\rho_l}\right)\left(\frac{h_v - h}{h_v - h_l}\right) \quad \textbf{(Eq.III.13)}$$

where, *FL* is the filing level, *V* is the tank volume fixed by the authors. It is equal to 6 m^3 and 3 m^3, for low pressure and medium pressure tank, respectively. V_l is the liquid volume. ρ, ρ_l are the mixture and liquid density, respectively. h_v, h_l, and h are the gas, liquid and mixture specific enthalpy, respectively. And q is the vapor mass fraction.

For both accumulators of the freezing system, the initial filling level represented 2/3 of the whole volume.

III.5. **Valve model**

The valve model used is an orifice valve model already available in the library and directly adopted. The model calculates the mass flow rate in function of the pressure drop using Bernoulli's equation. The mass flow rate could be computed by the equation below:

$$\dot{m}_v = A_{eff}.\sqrt{(p_1 - p_2).2\rho_1} \quad \textbf{(Eq.III.14)}$$

where A_{eff} is the effective flow area, ρ_1 is the inlet refrigerant density, p_1 and p_2 are the inlet and outlet pressures, respectively. The effective flow area of the high pressure side expansion valve is fixed at 4×10^{-6} m^2

III.6. **Pump model**

The pump model used is the refrigerant simple pump model of TIL library. The model is based on steady state mass and energy balance equations. A pump efficiency is defined at 60% as fixed value. This parameter is needed to calculate the pump shaft power that is entirely added to the energy balance of the medium. The mass flow rate is defined by the author based on the circulating rate which is equal to 4 in our case. Doing this, the gas mass fraction at the outlet of the evaporator is equal to 0.25 at nominal dry conditions.

III.7. **Condenser model**

The condenser modeled is an ALFA-LAVAL water-cooled condenser plate type with a maximal capacity of 517 kW. The geometric data of the condenser is summarized in **Table III.3** and illustrated in **Figure III.7**.

Table III.3: Condenser geometric data.

Condenser geometry	Plate exchanger
Number of plates	40
Length (m)	1.11
Width (m)	0.4
Pattern angle φ (deg)	35
Wall thickness (mm)	0.75

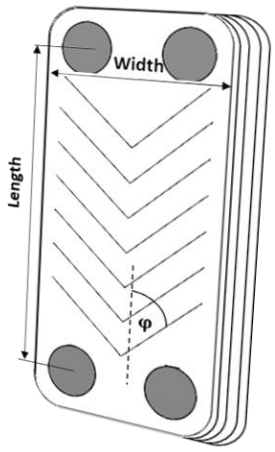

Figure III.7: Condenser geometry.

As the evaporator model, the condenser plate heat exchanger model is based on the finite volume elements approaches. Both refrigerant and water side are discretized and connected by mass, and heat transfer connectors. To solve the mass, energy and momentum balance equations, we have chosen a constant heat transfer coefficient that is equal to 2,000 $W.m^{-2}.K^{-1}$ for both mediums. And a zero-pressure drop is assumed for both sides. The water inlet temperature is equal to 21 °C.

III.8. **Cooling tower model**

Since the cooling tower is rated at different off-design conditions depending on ambient wet bulb temperature, on air and water flows and on heat load, its thermal performance varies as well. This latter had two key indicators called approach and range temperatures. They are defined as the difference between the inlet cold water temperature and wet bulb temperature, and the difference between the inlet and outlet water temperature, respectively. The smaller the approach temperature and the higher the range temperature, the more efficient the cooling tower.

A simple cooling tower is used from Building Library developed by Wetter et al. [154] on Modelica. The model represents a cooling tower with variable speed fan using a "York" cooling tower performance curve to compute the approach temperature. As expressed in equation **(Eq.III.15**), the "York" correlation uses a polynomial curve fit with water and airflow rate

ratios, wet-bulb temperature, and range temperature. The inlet air wet bulb temperature, tower range, and tower approach temperature at design conditions are defined. In our case, they are equal to, 12 °C, 9 K and 9 K, respectively. The corresponding water flow rate of 4.67 kg/s, and fan power of about 2 kW are specified. Thereafter, and using the empirical curves the approach temperature and fan power at off-design conditions are computed.

$$\boldsymbol{Approach = f(T_{wb}, T_r, F_{rw}, F_{ra})} \quad \textbf{(Eq.III.15)}$$

where:

T_{wb} : is the wet-bulb temperature;

T_r : is the range temperature;

F_{rw}, F_{ra}: are the ratio of actual mass flow rate and design flow rate for water and air, respectively.

It is to note that the ambient conditions are determined by real weather data of Nantes (France) based on EnergyPlus resources [183]. The water flow rate is imposed by the condenser loop. The airflow rate is imposed by the fan in order to maintain a constant exit water temperature.

The fan power is computed as follows:

$$\boldsymbol{P_{shaft} = P_{shaft,design} \times (F_{ra})^3} \quad \textbf{(Eq.III.16)}$$

Where $P_{shaft,design}$ is the fan power at design conditions.

The "York" model is only valid for a specific range of conditions (**Table III.4**). For each range, the authors make sure that each actual operating points would be between the minimum and maximum values especially when defining the control signals of the pump and the air fan.

Table III.4: Minimum and maximum limits for approach temperature in York and Actual models.

Independent Variable Limit	York	Model
Minimum Inlet Air Wet-Bulb Temperature	-34.4 °C	-4 °C
Maximum Inlet Air Wet-Bulb Temperature	26.7 °C	20 °C
Minimum Tower Range Temperature	1.1 K	9 K
Maximum Tower Range Temperature	22.2 K	9 K

Minimum Tower Approach Temperature	1.1 K	1.1 K
Maximum Tower Approach Temperature	40 K	26 K
Minimum Water Flow Rate Ratio	0.75	0.75
Maximum Water Flow Rate Ratio	1.25	1.25

III.9. **Tunnel and product**

III.9-1. Freezer Space

The interior freezer space including tunnel and products is modeled by an air volume with a heat flow source and a humidifier. The heat flow source represents the head load of the products to be frozen, thermal loads of air infiltrations, wall thermal losses, the conveyor belt heat load, and heat exchange between the tunnel and duct area. The humidifier modeled by a water vapor source represents water losses of the product during freezing. In addition, a hydraulic resistor is added to the air loop in order to take into consideration the pressure drop inside the freezer tunnel (**Figure III.8**).

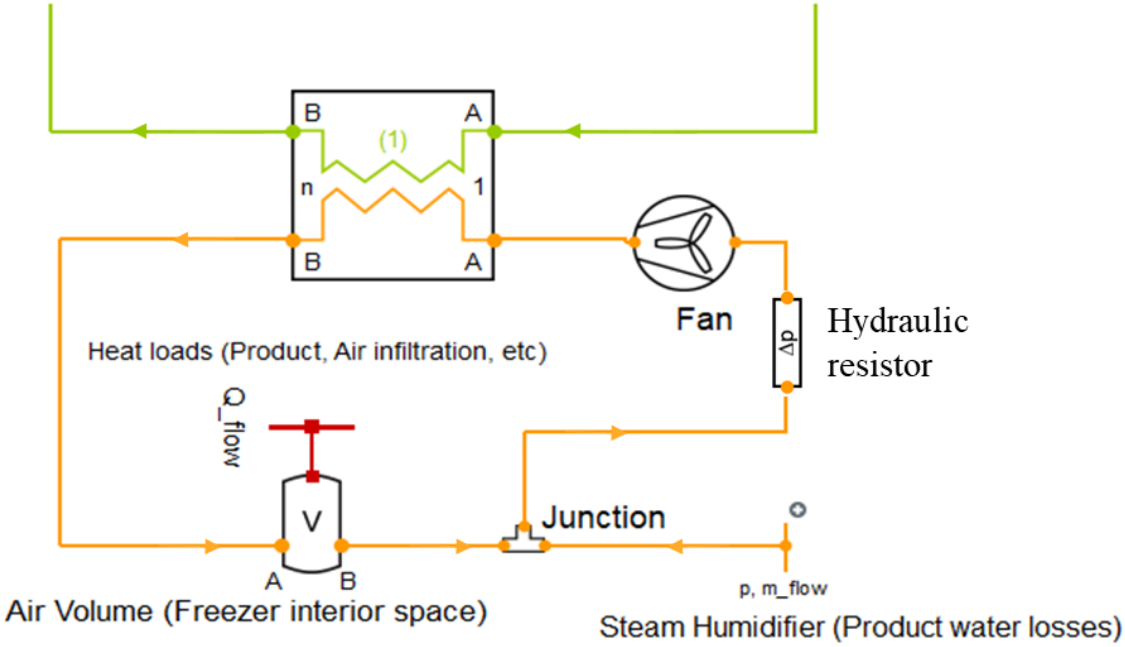

Figure III.8: Air loop model on Dymola layout.

A. Food product

The processed food products are unpackaged rectangular pizzas. Each pizza is 1 cm thick and measures 310 mm × 510 mm and spends 42 minutes inside the freezer. To take into

consideration the presence of product during the freezing process, the heat load of the product is computed by the following equation:

$$\dot{Q}_{air-produit} = \alpha_p A_p (T_{freezer} - T_{product}) + \dot{m}_{water\ vapor} L_{sv} \quad \textbf{(Eq.III.17)}$$

where,

- $T_{freezer}$ is the freezer temperature computed as the average air temperature at the evaporator outlet and inlet;
- $T_{product}$ is a representative temperature of the product during freezing;
- A_p is the exchange area. In our case, only the bottom and top surface of the product are considered;
- α_p is the convective heat transfer coefficient. It is computed by a correlation developed from the experimental results as function of air velocity. It will be presented in the experimental **section III.11**.

Regarding the product moisture losses, they have been determined from the experimental results. Doing this, a mass flow rate $\dot{m}_{water\ vapor}$ was defined in the steam humidifier, thus taking into consideration the latent heat loads.

B. Other heat loads

All the heat loads described in **section A** are presented by a simplified equation represented as:

$$\dot{Q}_F = \dot{Q}_{conveyor} + K\ A_F\ (T_{freezer} - T_{dock\ area}) \quad \textbf{(Eq.III.18)}$$

Where,

- *K* is an overall coefficient of heat transmission, assumed to be equal to 2.2 $W.m^{-2}.K^{-1}$. This coefficient has been determined based on an energy balance of the freezing system performed by CETIAT partner;
- A_F: is the external freezer surface;
- $\dot{Q}_{conveyor}$: a constant heat load representing the conveyor belt thermal load (21 kW).

III.10. **System control**

All the system control is carried out by PID controllers. The latter are used to:

- Control the driver position of the compressors in order to maintain constant the pressures at the Vapor-Liquid separators (Low and medium pressures). The minimum driver position is limited to 40%;
- Control the valve section in order to maintain constant the filing level of the vapor liquid separator of medium pressure;
- Control the water flow rate of condenser pump in order to maintain constant the condensation pressure;
- Control the cooling tower fan speed in order to maintain constant the water exit temperature at the set point.

III.11. **Experiment and instrumentation**

An experimental investigation has been conducted by Oniris, CETIAT and GEA Refrigeration. The objective of this study was to better understand the freezing system behavior during a real production day in a frozen food production industry.

In fact, several measurements have been carried out in order to analyze the effect of frost on the hydrothermal performance of the freezer, on the product quality, and also to identify the major source of humidity responsible for frost formation. A series of measurement has been made but for both reasons of confidentiality and system complexity, only few experimental results has been exploited and will be presented in this document.

III.11-1. Pressures and air velocity

Many Pitot tubes are placed downstream and upstream of the evaporator and the fan in order to measure the static and total pressures. These measurements were carried out in nominal conditions first (freezing system being turned off), in order to determine the nominal heat exchanger pressure drop, the frontal air velocity and the fan nominal pressure and airflow rate. Thereafter, the same measurements are made under frost conditions in order to dynamically monitor the influence of frost.

The static and total pressure are measured with a Pitot tube with measuring range -1,250/1,250 Pa, within the uncertainty range -3/+3 Pa. The dynamic pressure is then transmitted by KIMO 0-100 differential transmitter. Knowing the evaporator frontal area, the air velocity is deduced.

The Pitot tubes are placed downstream and upstream of the evaporator and the fan. The cold coil has been divided into several meshes where the pressure sensors have been placed (**Figure**

III.9). It has been observed that the air velocity is not uniform over the entire coil. This is due to the non-uniform ventilation and air distribution. For this reason, the air velocity values in each cell were recorded, and then averaged over the entire coil surface.

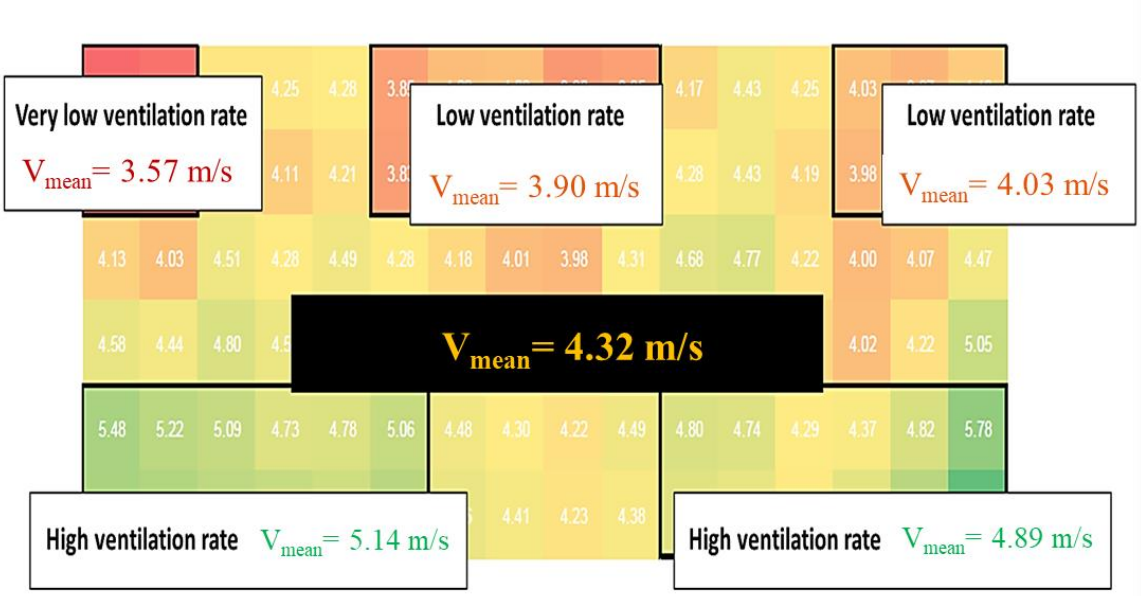

Figure III.9: Air velocity measured on the frontal side of the evaporator (measured by CETIAT).

III.11-2. Air and refrigerant temperatures

The average inlet air temperature is calculated as the average temperature of eight air temperatures measured by thermocouples placed at the entry of the evaporator. These measurements are carried out using type T-thermocouples, characterized by an uncertainty range of ±0.5 K and recorded on an acquisition unit placed outside of freezer. For each location

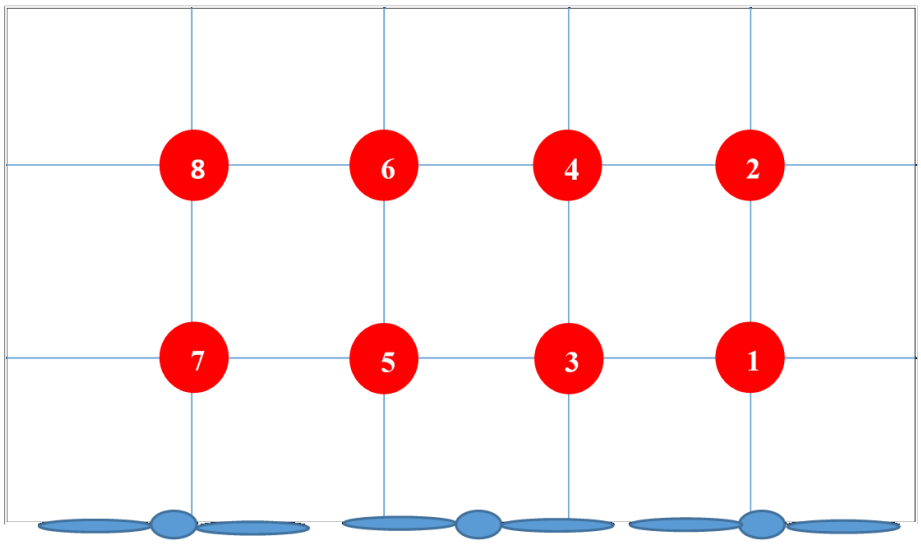

Figure III.10: Thermocouples location at the entrance of the evaporator

identified in **Figure III.10**, a pair of thermocouples has been installed. One thermocouple is left free in the airflow between fins, while the other is attached directly to the ammonia tube in order to record the contact temperature. The evolution of the temperature difference between these two values is exploited as an indicator of the evaporator frosting effect.

III.11-3. Air-product heat exchange quality

For the convective heat transfer coefficient of the food freezing process, a large number of convective heat transfer coefficient correlations have been obtained on the basis of experimental research, which can be directly used to calculate the convective heat transfer coefficient between food and air. However, these correlations are usually restricted to application condition. For specific geometries and flow field in industrial process, it is often complex to adopt these heat transfer coefficient correlations. Thereby, a specific correlation was developed for the actual conditions.

The air-product convective heat transfer coefficient was measured by a special heat flux sensor (**Figure III.11**) placed, at different moments during the production day over 15 hours, on the conveyor at the freezer inlet. The sensor spent, as the product, 42 minutes before being picked up. The results were used in order to bring out an average air-product convective heat transfer coefficient for each passage. Two thermocouples were connected to the device. One thermocouple was to measure the air temperature and the other one was placed in the heat flux cell to monitor its temperature during the 42 minutes residence time.

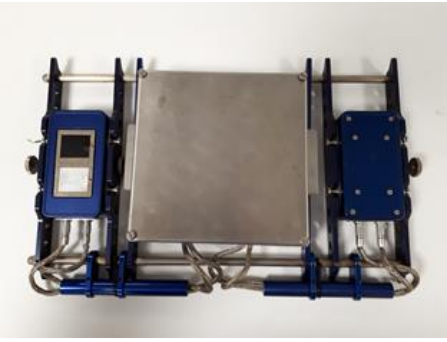

Figure III.11: Airflow device for air-product convective heat transfer coefficient measurement.

Figure III.12 illustrates the first recording measurement of the convective heat transfer coefficient (freezer empty) as function of the position on the conveyor belt. The position is defined depending on the full conveyor belt length L_0. It could be observed that the heat transfer coefficient oscillates depending on the horizontal distance from the fan. It is maximum when the products are on the fan side and minimum when they are on the opposite side. As

consequence, for simplification reason, the convective heat transfer coefficient was averaged. At each moment, the correspondent air velocity was defined by experimental results in order to perform the following empirical correlation:

$$\alpha_p = 22.3 \times V_a^{0.4} \qquad \textbf{(Eq.III.19)}$$

This correlation is valid for an apparent air velocity ranging from 2.5 m/s and 4.5 m/s.

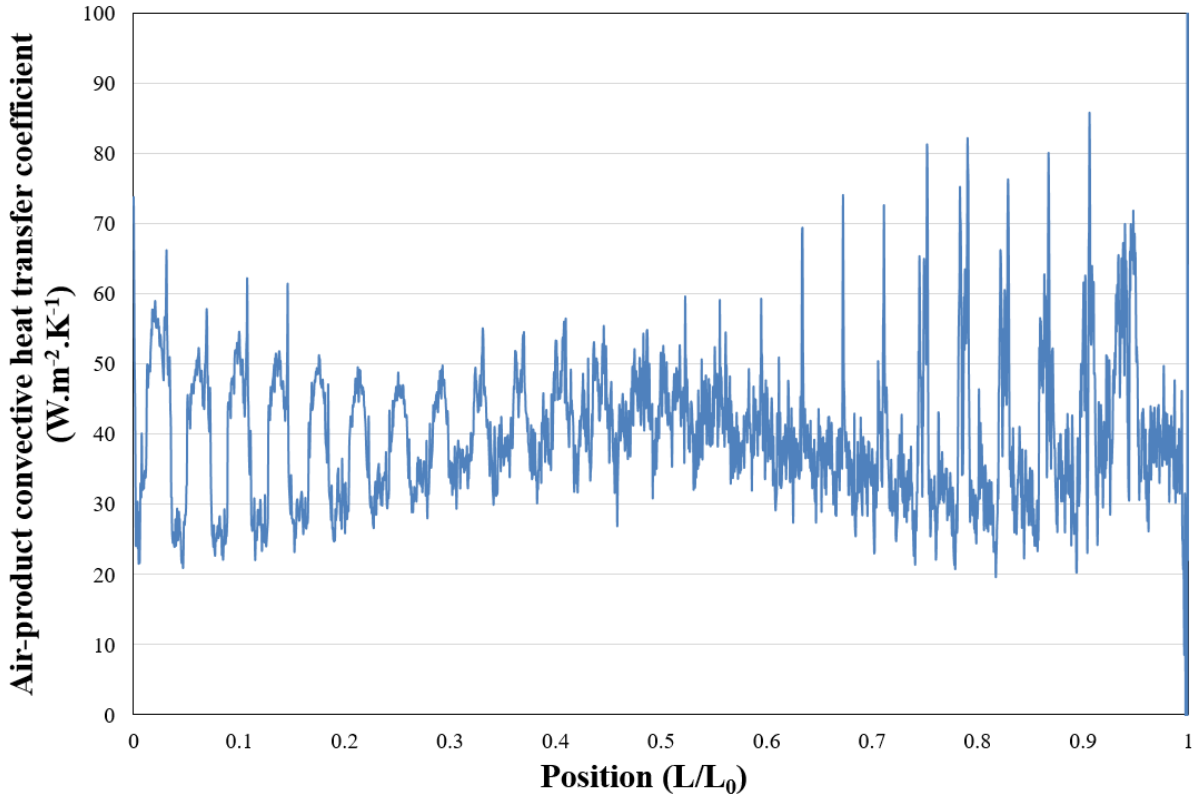

Figure III.12: First air-product convective heat transfer coefficient measurements as function of the position on the conveyor belt.

III.11-4. Product water losses

Successive weight measurements of many products throughout the production day (around one sample every 30 minutes) were performed at the inlet and the outlet of the tunnel.

It should be noted that two types of pizza of the same size but different mass, of 1.5 kg and 1.68 kg, respectively, were frozen during the production day. The first 11 hours were devoted to the first type and 4 hours for the second. 1 hour was spent in production line adaptation between the two references.

Table III.5: Experimental results of the amount of food water losses during freezing.

	Water losses during freezing	
	Type 1	**Type 2**
Average (g)	16.8	18.7
Standard deviation (g)	2.2	2.1

As depicted in **Table III.5** the rate of water loss during the freezing process for both pizza types represent almost 1.1% of the initial pizza weight. This value is in agreement with typical blast freezer application [184].

III.11-5. Frost growth and evaporator cross section area

A recording camera was placed below the evaporator (at the inlet air-side) (**Figure III.13**) to monitor its front side. Also, it takes pictures every 7 seconds. GO5000 camera is used with a sensor (2,560 × 2,048 pixels) associated with a RICOH FL-BC2518-9M lens with a focal length of 25 mm. The lens is positioned 60 cm from the ground, which means that the camera-object distance is 103 cm. Under these conditions, the observation area window is 0.22 m² (529 mm × 423 mm) which represents around 2.2 % of the total frontal section. The resolution of the image is 207 µm / pixel.

The camera was turned on when the freezer tunnel was in cooling mode, around 4 a.m. A recorded film was made at the rate of one image every 7 seconds. From these films, 487 images were extracted with a time step of 112 s. Several disturbances are visible in the film, slight

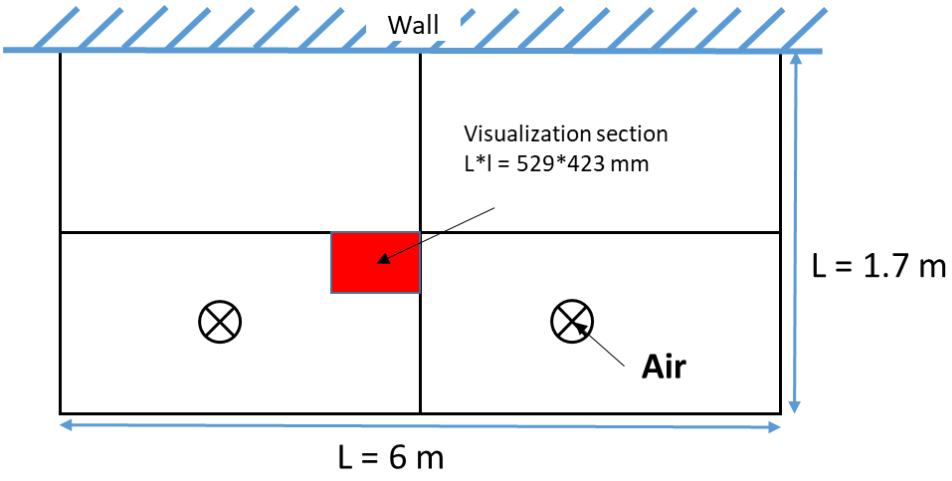

Figure III.13: Location of the recording camera in front of the evaporator

movements of the camera, sudden change in brightness due to door opening or staff intervention, etc.

In ImageJ software, the histograms of the images were normalized to smooth out differences in illumination. In the CTAn software, the images were filtered in order to increase the local contrasts with a Conditional mean filter (in 2D, round kernel of radius 3, threshold 50).

In ImageJ, the images have been aligned on the initial image (Stack Reg function) and a film has been made. Image 3 of the film was chosen to create the initial mask because it offers better contrast between the background and the coil. The mask was made from an overlay for the vertical tubes followed by thresholding (**Figure III.14**).

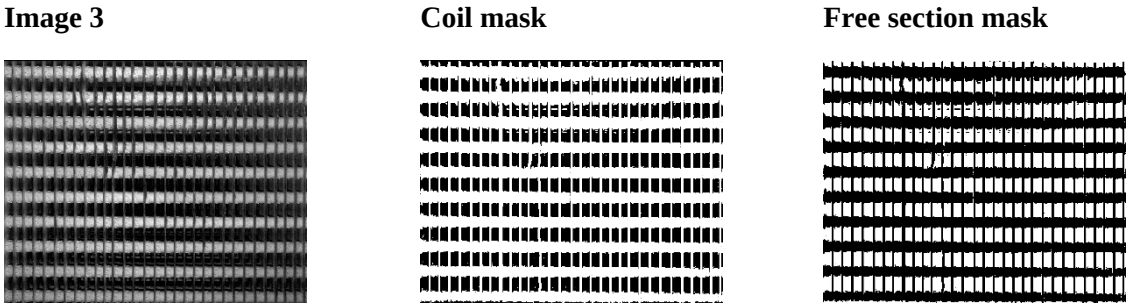

Figure III.14: Image processing - Coil and free section mask.

Then, image 3, chosen as the initial reference, was subtracted from all the images, which made it possible to obtain a film showing only the frost that forms during recording. Finally, the mask is applied to these images, then they are thresholded (gray level 44) to highlight the frost which forms at coil free opened section **Figure III.15**. The area of the openings can then be calculated.

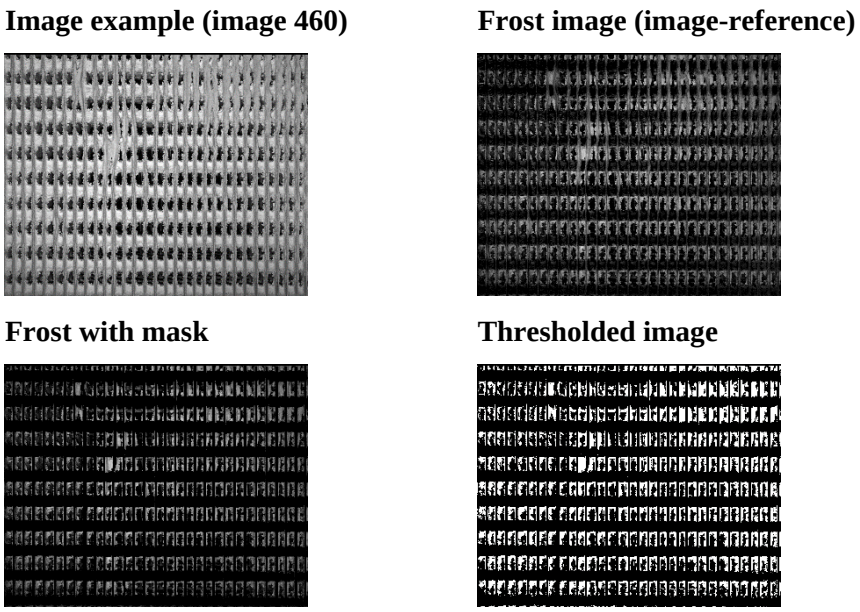

Figure III.15: Example of image processing.

III.12. **Results and discussions**

III.12-1. Fan pressure, Evaporator and tunnel pressure drop.

As can be seen on **Figure III.16**, the pressure drop across the evaporator continues to increase during the production cycle. The initial value is approximately 220 Pa, which corresponds to the experimental measurement and manufacturer's documentation at the nominal operating conditions. Operating under frosting conditions, the pressure drop increases to reach approximately 400 Pa, that means an increase of 100% compared to the initial value. This increase is due to the accumulation of frost on the coil which ultimately has the effect of reducing the airflow through the coil. Note that the pressure supplied by the fan is the reverse image of the pressure drop: the fan undergoes pressure changes. The residual static pressure, computed using experimental results, is represented by the gray curve and it is assumed to be the pressure drop through the tunnel.

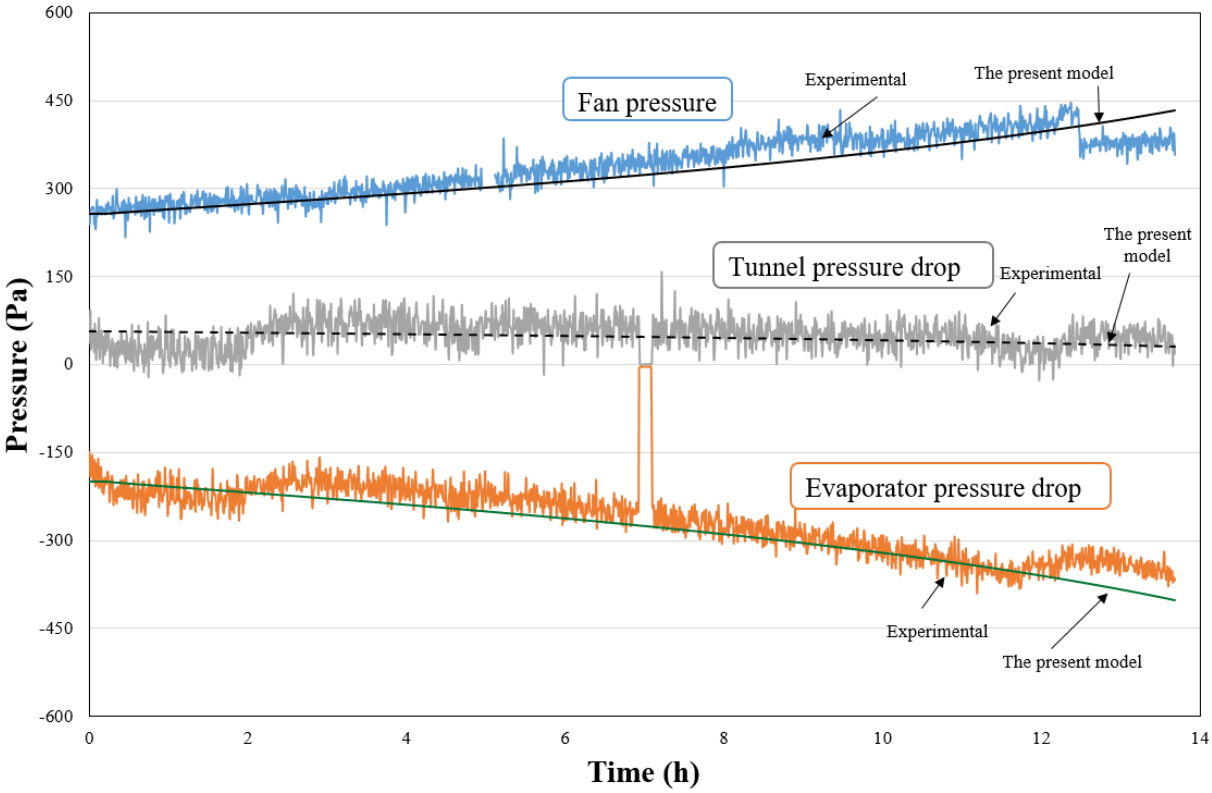

Figure III.16: Experimental and numerical results: Fan pressure, pressure drop through the evaporator coil and tunnel.

The deposition and growth of frost on the surface of heat exchanger leads to a smaller airflow passage area. This has a direct impact on air-side conditions by increasing the pressure drop across the coil. The experimental value for pressure drops increases from 220 Pa to around 450

Pa at the end of the experiment. The actual model predicts the same trends. Numerical values are within 5% far from the experimental results.

By the end of production cycle, an intervention was made in order to scrape the front of the evaporator coil from frost. This operation is therefore effective which explains the small reduction in pressure drop toward the end on the experimental curve. By the end the pressure drop was around 380 Pa. This intervention could explain the difference between numerical and experimental results by the end of the day.

III.12-2. Evaporator cross section area

One can observe from **Figure III.17** that the air cross section area was reduced by almost 60% during the day. The numerical model predicts similar trend during 15 hours. The difference between the numerical and experimental results could be explained by several causes. The main cause is the section filmed by the camera which represents only 2.2 % of the entire air passage section. Noting that the frost is not distributed uniformly on the front face, this opening rate does not necessarily represent the average opening rate of the entire cold coil. On the other hand, measurement uncertainties could lead to small differences.

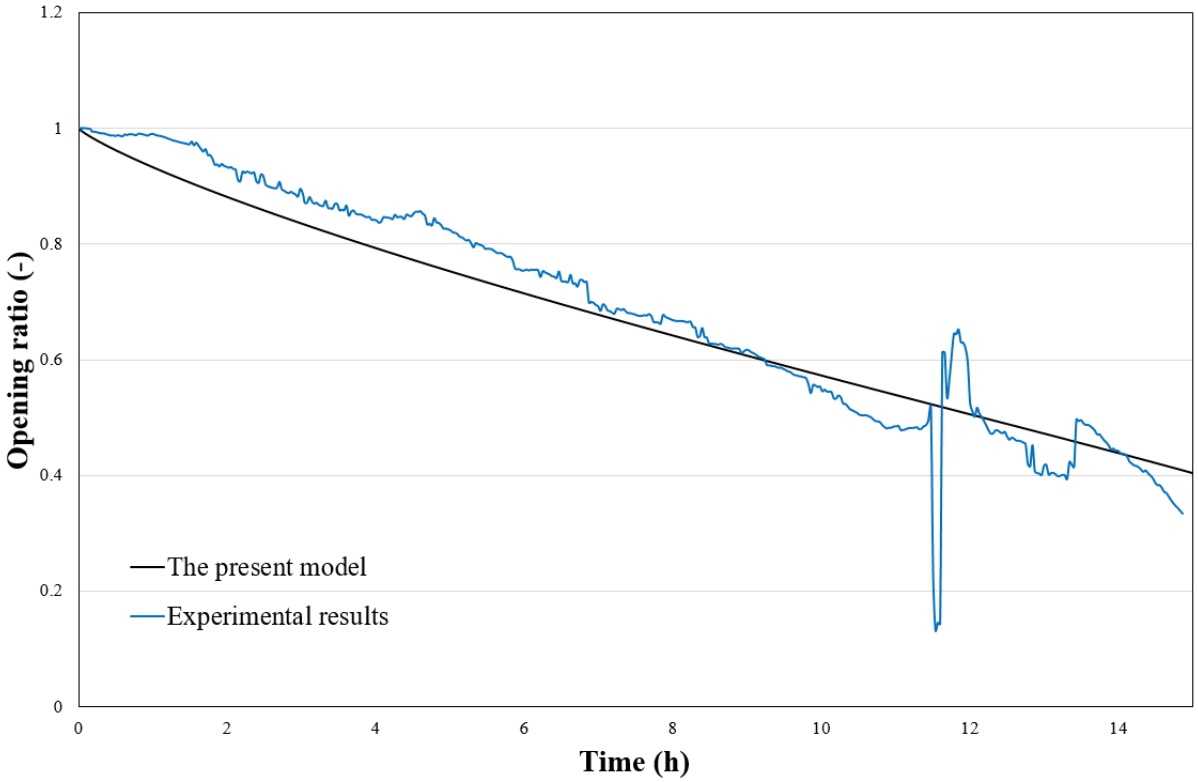

Figure III.17: Experimental and numerical results of the cross section area opening ratio.

Moreover, brutal variations can be noted in **Figure III.17**, especially at the 12th hour. This is due to frost formation on the glass windows of the camera and also to the high sensitivity of the camera to lighting disturbance inside the freezer.

III.12-3. Air-product heat transfer coefficient

Another phenomenon directly related to the blockage of the airflow passage section is the reduction of the Air-product heat transfer coefficient. According to **Figure III.18**, the convective heat transfer coefficient decreases slowly at beginning of the freezing process then it increases slightly at the 12th hour of the production day. This due to the change of product after a freezing stop of one hour. Since the freezer was empty for an hour, the performance was slightly improved and the convective heat transfer coefficient at the introduction of the second product was around of 38 W.m^{-2}.K^{-1} comparing to the end of the first production where it was around 36 W.m^{-2}.K^{-1}. This operation could also explain the slight difference between numerical and experimental results.

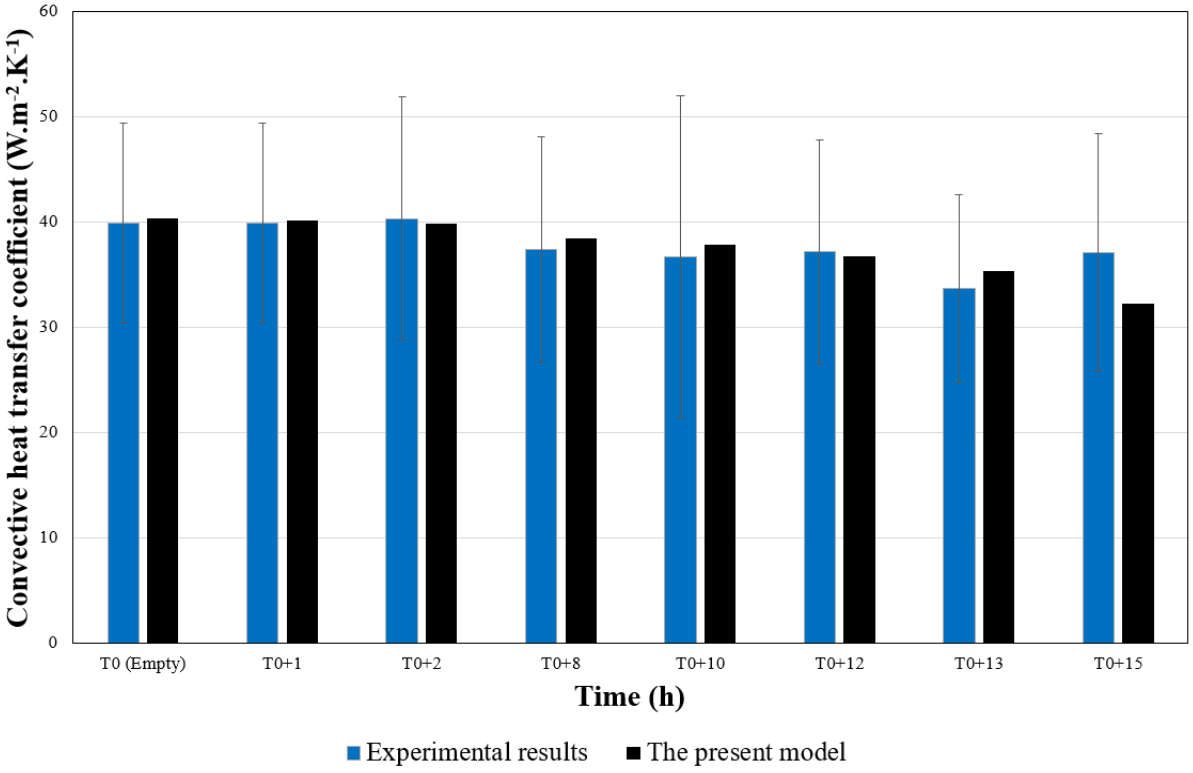

Figure III.18: Experimental and numerical results: Air-product convective heat transfer coefficient.

The interpretation of the whole situation could be that the reduction is directly attributed to the blockage of airflow passage due to the frost buildup. Taking into consideration the hydraulic coupling between the fan and the coil, the airflow reduces in fan-supplied evaporator which is one of the main causes of the heat exchange reduction. The cross-section area has been blocked

by 80%, the pressure drops increase by 100%, and the heat transfer coefficient decreases by about 20%. It is to note that the standard deviation does not reflect the measurement uncertainty but rather the deviation of the convective coefficient values that vary as the heat flux device passes through the tunnel.

III.13. **Summary**

A theoretical model of a whole and complete freezing system subjected to frost accumulation has been developed based on Modelica orient object language. The model prediction agreed well with their experimental data in terms of air pressure drop, blockage ratio of the evaporator cross section area and the air-product convective heat transfer coefficient.

The comparisons between the simulation and experimental data show that the proposed model can capture the major heat transfer and flow transients characteristics of the freezing system under real frosting conditions. Thereafter, the numerical model could be exploited to obtain possible data about the local aspect of frost on the evaporator as well as the effect of the frost accumulation on the energy performance and on the quality of the product during a typical industrial production day.

CHAPTER IV

Results analysis and sensitivity study

CHAPTER IV: Results analysis and sensitivity study

This chapter analyses the numerical results boosted by the experimental analysis of the freezing system behavior under frosting conditions. The aim is to firstly present and discuss of frost growth formation at the evaporator level. The second objective is to quantify the effect of frost formation on the energy performance of the whole system and on the quality of the product. Subsequently, a sensitivity analysis is performed in order to quantify the effect of product water losses on frost growth since it appears to be the main source of moisture in such an industrial freezer with unpacked products. Finally, optimizations strategies are proposed conjoining energy performance and food quality preservation in both dry and frosting conditions.

IV.1. **Nominal conditions**

The results discussed in this section aim to analyze the freezing system behavior under baseline conditions where the evaporator temperature is equal to -40 °C and the initial air inlet temperature is around -35 °C. The products enter into the freezer at initial temperature of 40 °C with a rate of 8 pizzas/min. During the freezing process that lasts 42 min, the product lost water flow rate is of the order of 2.2 g/s. The initial air relative humidity inside the freezer is assumed to be 70%.

IV.1-1. Local Analysis

The numerical results reported on **Figure IV.1** shows the distribution of frost thickness along the airflow direction. It is noticeable that the evaporator is subjected to non-uniform frost growth from one row to another. Thicker frost layers tend to form in the first rows, where both mass transfer coefficient and humidity gradients are much higher, whereas thinner frost layer build up in the last rows. In the first few minutes, the absolute humidity difference between air and frost surface is around 7.35×10^{-5} kg/kg_{da} in the first row at the leading edge. The absolute humidity difference reaches 5.32×10^{-5} kg/kg_{da}, 2.03×10^{-5} kg/kg_{da} and 1.11×10^{-5} kg/kg_{da} in the 5^{th} row, the 9^{th} row and the last row at the exit side, respectively. This means that the driving force, i.e., absolute humidity difference decreases by 84% from the air inlet to the exit side.

As can be seen from the graph of the calculated frost thickness versus time, there is not a big difference between the thicknesses in the rows, in particular between the row 1, 5 and 9. After 15 hours of operation, the thickness at the leading edge is only 1.2, and 2 times greater than that

at row 5 and 9, respectively. There are usually much more variations in frost thickness through the airflow direction in uniform finned tube heat exchangers. This can be explained by the fact that lower humidity gradient downstream of the coil is compensated by its higher fin density, which leads to a larger surface area for frost formation. It is only at the rear of the heat exchanger that the frost accumulation rate becomes significantly low due to the low humidity of the air at the outlet as well as the low temperature and humidity gradients. At the end of the day, the frost formed is only 1.7 mm thick downstream of the evaporator.

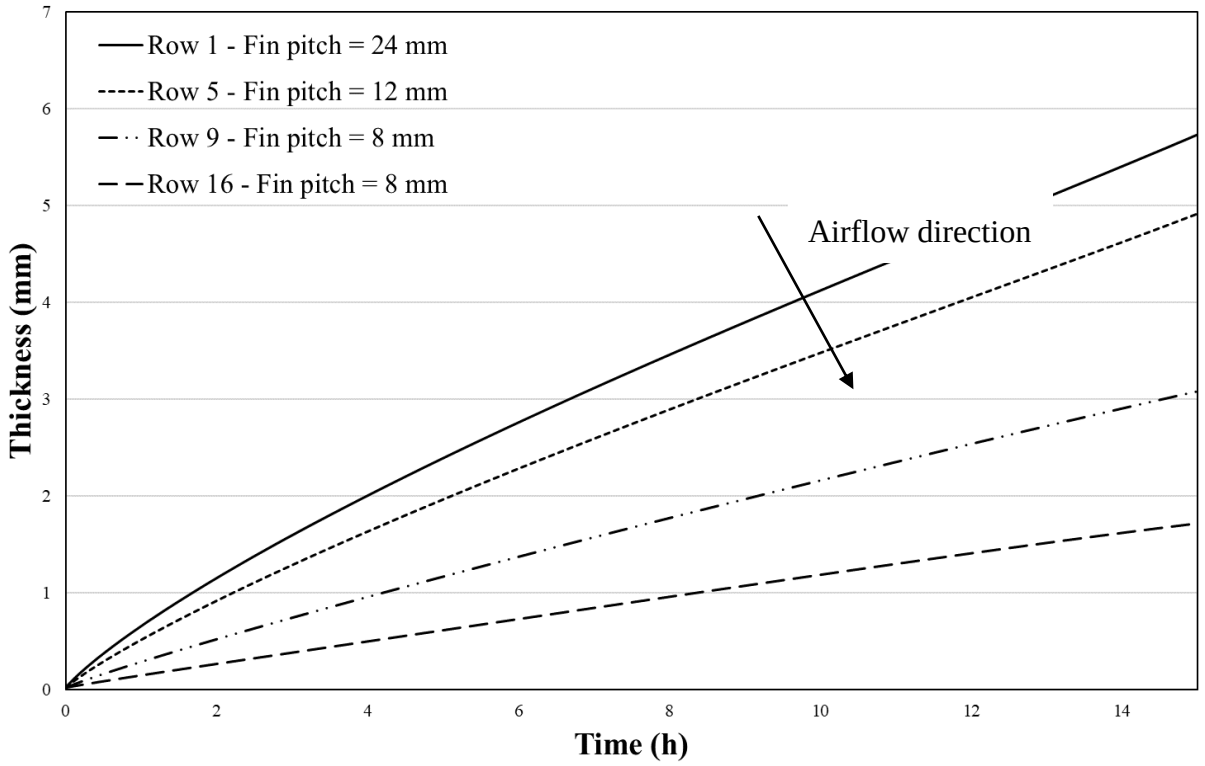

Figure IV.1: Frost Thickness distribution along the evaporator.

The present numerical model appears to be able to predict the distribution of frost which is consistent with previous reports. However, the experimental results showed another distribution of frost, in particular on the front face of the evaporator. The frost is not uniformly accumulated on the cross section (**Figure IV.2**). This can be explained by the non-uniform air velocity measured experimentally upstream of the evaporator **(Figure III.1)**. Another reason is that the evaporator in such food processing application is usually exposed to a warm and humid air stream from fresh food entering the freezer, and cold and dry air stream from the frozen food. Therefore, at the same time, different airflow states are circulated by the fan and distributed over the leading edge. In order to simplify the analysis, the model does not account for this type of local variation in the frost thickness, and assumes that the frost grows uniformly within each

control volume. The proposed model is then unable to capture this phenomenon, but it predicts well the whole frost mapping that has been proven in the estimation of the air side pressure drop presented in the **previous chapter**.

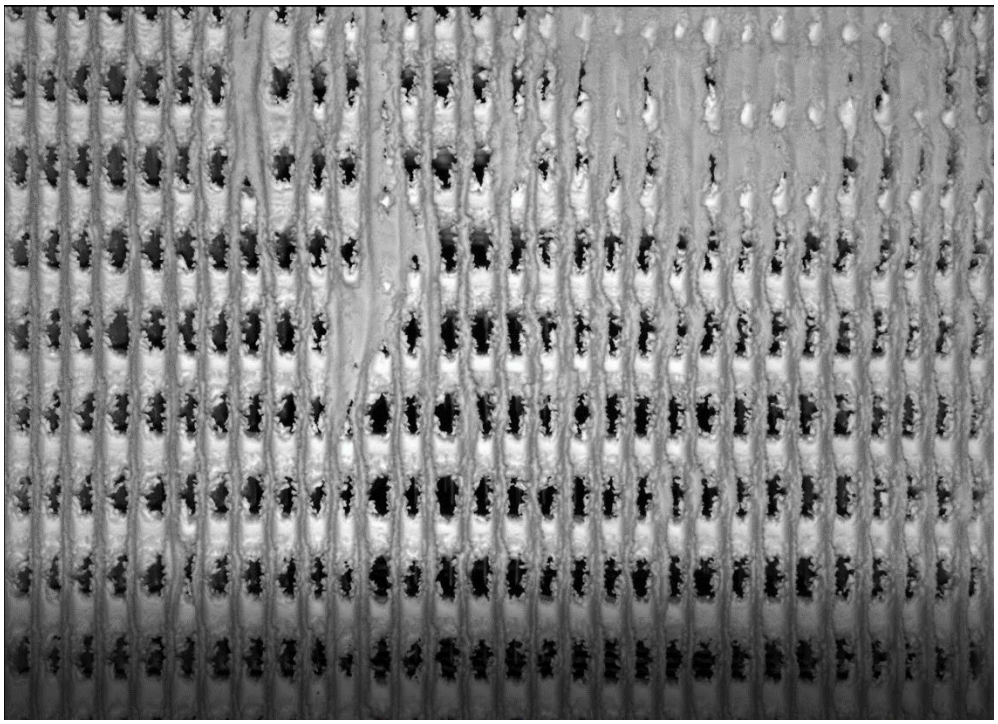

Figure IV.2: Frost morphology and distribution on the cross section area.

The frost thickness does not tell the whole story though. Another important frost characteristic to the evaporator operation is the frost layer density. **Figure IV.3**, shows the frost density along the airflow direction. The trends stay the same as frost thickness. Row 1 has the denser frost layer and row 16 at the exist of the evaporator has the lower density. As the humid air flows along a cold plate, the temperature and the humidity of the air decrease due to the upstream heat and mass transfer with cold surface. Thus, the thickness and the density of the frost layer decrease with distance from the leading edge.

As discussed in **Chapter 2**, and consistently with previous studies [31], [33], [106], the freezing conditions give rise to frost growth that is more rough, thick, and with very low-density comparing with frost that grows under heat pump or air-conditioning conditions. At air temperature of 5 °C, wall temperature of -15 °C, air velocity of 1 m/s and relative humidity of about 80%, the frost density may reach 150 kg/m^3 only after 180 min of operation. At these conditions, the densification flux represented about 30% of the total mass flux of water vapor transferred from the air to the frost surface. Under freezing conditions, as illustrated in **Figure IV.3** and clearly shown on **Figure IV.2**, the frost seems to be snow-like in both appearance and crystal structure, and is fundamentally different from more traditionally formed frost.

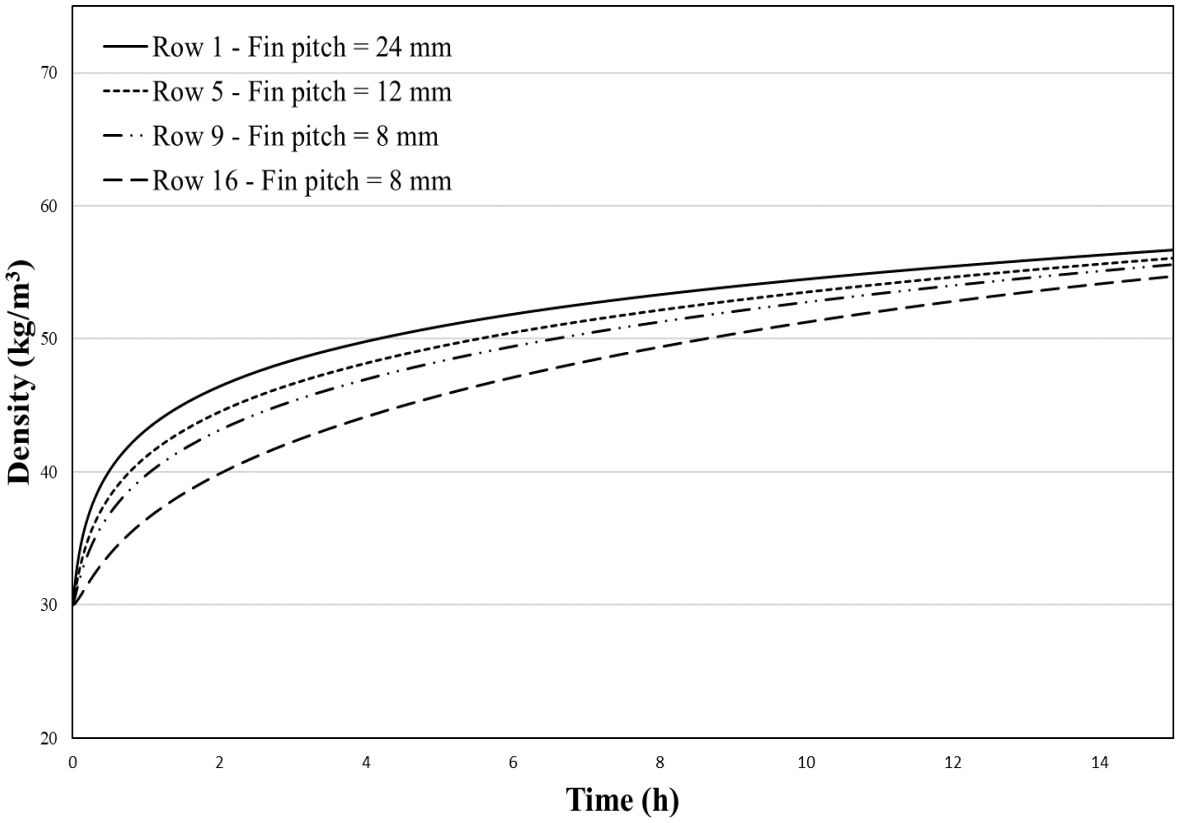

Figure IV.3: Frost density distribution along the airflow direction.

The average frost density on the whole evaporator is around 55 kg/m^3 after 15 hours of operation. The densification rate represents only 10% of the whole growth rate. Consequently, the frost formed has a low average thermal conductivity in the order of 0.15 W.m^{-1}.K^{-1} closer to the thermal conductivity of snow (0.045 W.m^{-1}.K^{-1}) than this of a compact ice layer (2.1 W.m^{-1}.K^{-1}).

As we saw in the previous chapter, the pressure drop on the air side keeps increasing during the operating time. This increase affects the airflow rate supplied by the fan and, therefore, the cooling capacity. As shown in **Figure IV.5**, the airflow rate has decreased by 37%, highlighting the importance of considering the fan characteristics when the evaporator operates under frosting conditions.

The cooling capacity decreased by about 19% after 15 hours. This is due not only to the drop in the air volume flow rate but also to the additional surface thermal resistance imposed by the frost.

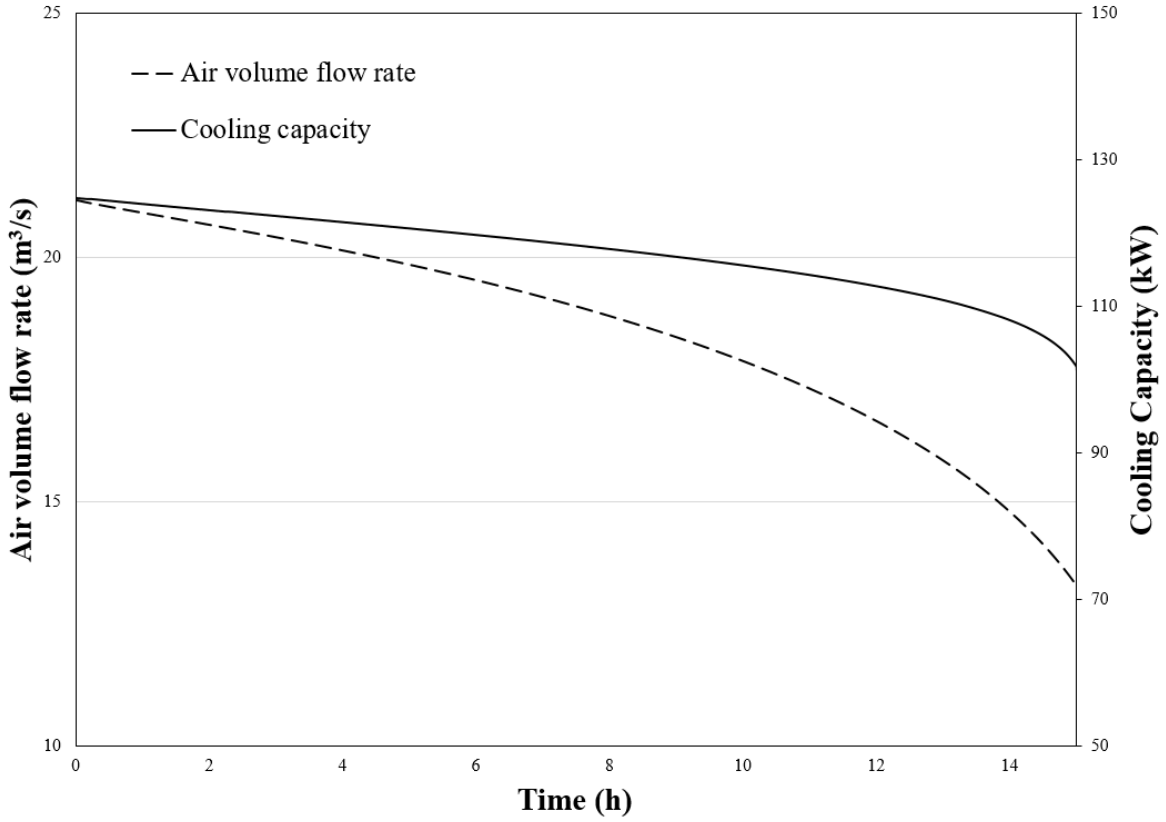

Figure IV.5: Air volume flow rate and cooling capacity.

Figure IV.4 compares the influence of the frost blocking effect (convective thermal resistance) and the low conductivity frost layer (conductive thermal resistance) on the overall thermal resistance.

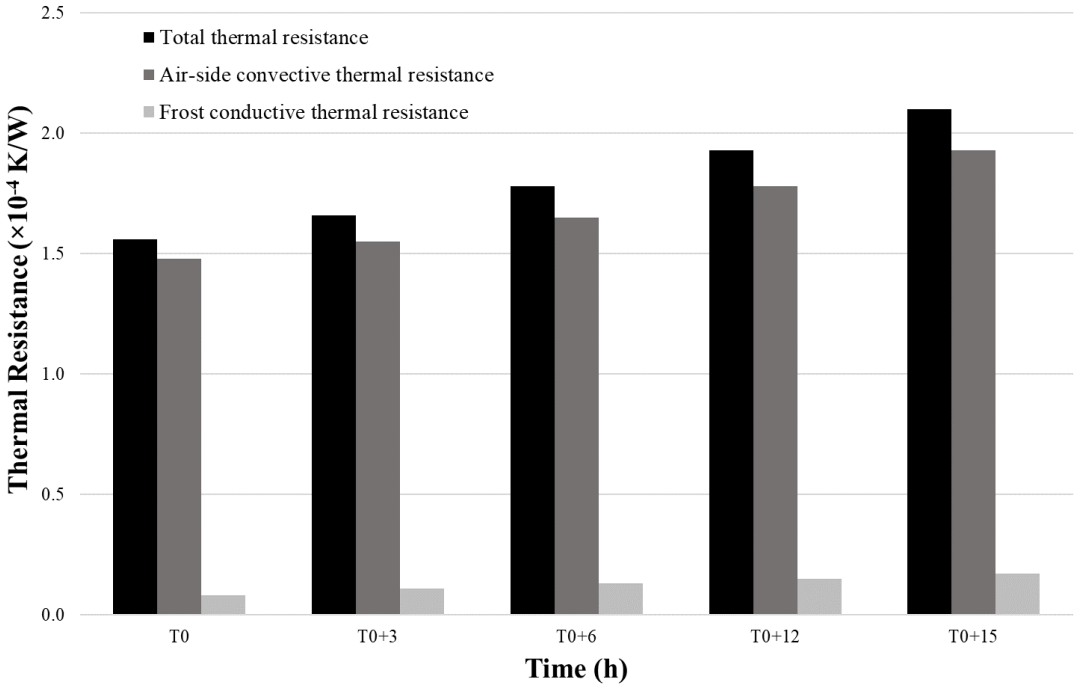

Figure IV.4: Comparison between air-side and frost layer thermal resistances.

The frost conductive thermal resistance represents 5% of the total thermal resistance in the early stages of frosting, and increased to 8% after 15 hours. The convective thermal resistance between the frost surface and the air was approximately 93% of the total thermal resistance. It increased by about 21% during the day. Therefore, the coupling between the airflow rate and the growth of frost could not be negligible when predicting the performance of a frosted heat exchanger.

IV.1-2. System-level Analysis

If the frost formation affects primarily the evaporator, it leads also to degradation of the performance of the other components of the installation and, therefore of the whole system. When analyzing the system behavior, pressure levels in suction and discharge lines affect compressor performance and energy consumption. The pressure levels are influenced by surrounding conditions. The heat transfer conditions are influenced by the presence of frost. The heat transfer quality as well as the food heat load affect the evaporating temperature whereas the cooling water affects the condensing temperature. It is known that higher differences between these temperatures results in lower COP.

Let us start with the compressors since they are considered with the evaporator fans as the largest consumers of energy that often not operated at their highest efficiency. Since the freezer cooling capacity decreases due to frost accumulation, the PID controllers adapts the compressors' capacities to the changing requirements.

An analysis of the volumetric efficiency of the compressors showed that they move away from the optimal operating point. Since the two compressors of the actual freezing system were screw compressors regulated by slide valves, they provide easy capacity control, but also have low energy efficiency. **Figure IV.6** illustrated the varying volumetric efficiency with a slide valve. When the slide valve is open, it creates a by-pass to the compression chamber and then some of the gas inside the compressor will be vented back to the suction port. This provides a regulation of the cooling capacity but the efficiency is reduced because of the reduction the swept volume. The LP and HP compressors start running at approximatively full load that lasts for about 1 hour and 1.5 hours, respectively. Thereafter they continue on part-load operation mode. One can observe that a small opening of the slide valve results in a larger capacity drop. A small opening of around 4% can lead to a reduction in volumetric efficiency by about 17%.

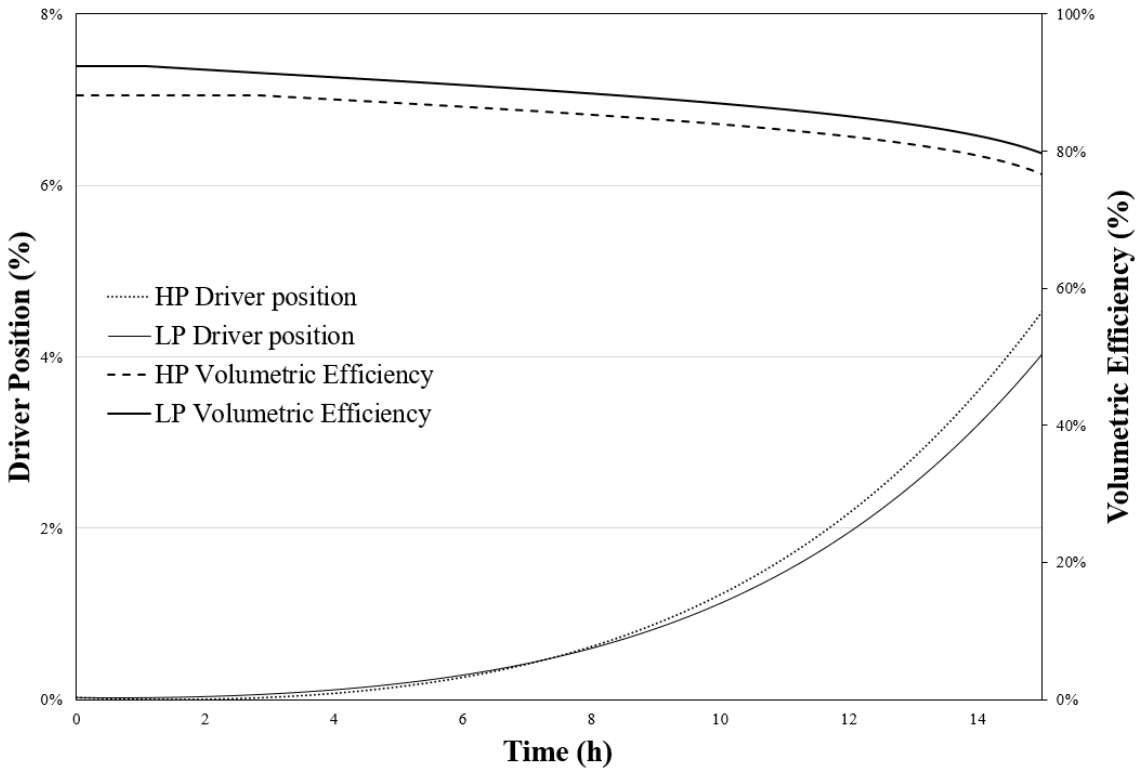

Figure IV.6: Compressors' Volumetric efficiencies and Drivers' positions.

The filing level of the intermediate pressure separator remains constant by using the valve opening control on the expansion valve. However, the filing level of the low pressure separator drops slightly. The mass flow rate of the ammonia entering the condenser decreases and the condensing pressure remains constant thanks to the cooling water mass flow rate controlled by the pump.

As consequence, the cooling water temperature at the outlet of the condenser increased. It reaches about 32 °C at the end of simulation. Therefore, the cooling tower fan speed adapts to adjust the condensing power.

As shown in **Figure IV.7**, the freezer temperature, computed as the average temperature between the evaporator air exit and inlet temperature, increases over time due to the decrease of the cooling performance of the evaporator. By imposing the same heat load of the product, the air inlet temperature increases with time. The evolution trend seems to be consistent with experimental observations but the experimental results could not be used for comparison. During our experimental campaign, the freezer was empty during more than an hour due to change over time, i.e., in order to adapt the production line to the second reference of product to be processed. As consequence, the freezer slightly recovered its performance and the air temperature has been decreased before introducing the products. Since these specific

interventions are not taken into account in the simulation process, some measured parameters cannot be compared.

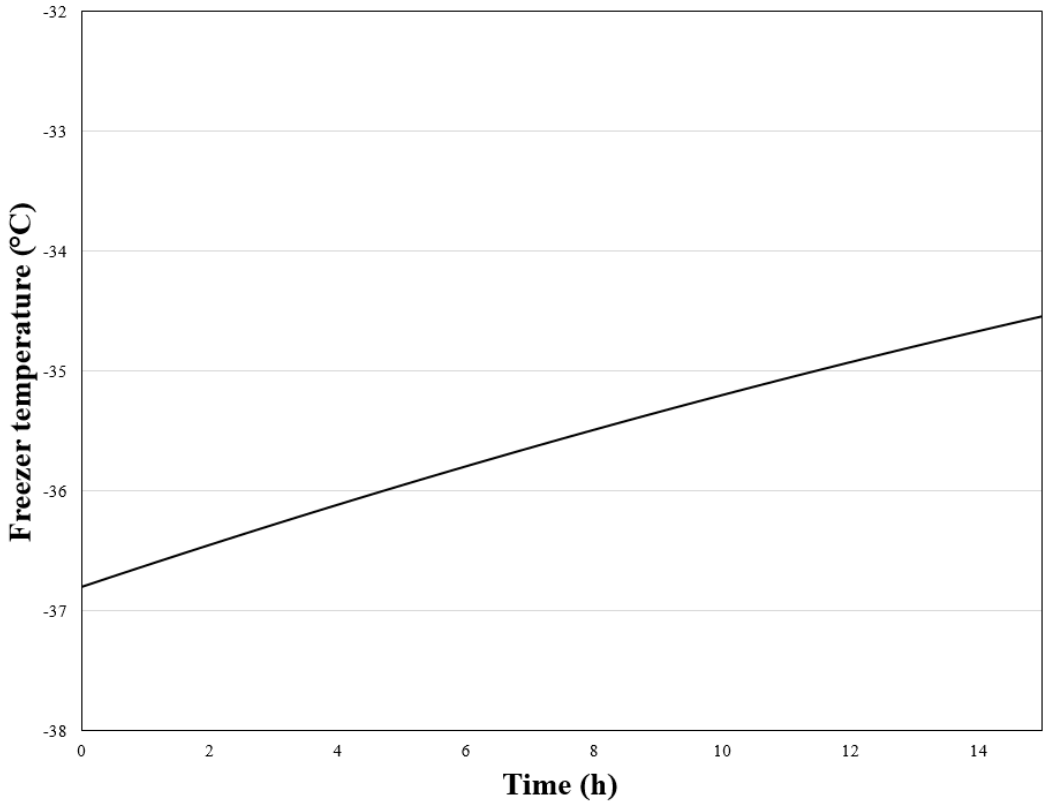

Figure IV.7: Freezer temperature evolution.

The frost accumulation has a direct effect on the variations in thermo-hydraulic performance of the evaporator. Dealing with these variations, all the components react in order to adapt to the cooling capacity at each time. This effect can be highlighted by evaluating the overall performance indicator COP. The former refers to the ratio of cooling capacity of the system to the energy consumed by compressors, fans, and pumps. The instantons COP_{inst} is computed by **(Eq.IV.1)**:

$$\boldsymbol{COP_{inst} = \frac{\dot{Q}_{evap}}{\dot{W}_{compressors} + \dot{W}_{pumps} + \dot{W}_{fans}}} \qquad \textbf{(Eq.IV.1)}$$

Where, $\dot{Q}_{evap}$ is the evaporator cooling capacity.

The most important characteristic indicator for the whole 15-hours operating time is the average COP_{avg} defined by **(Eq.IV.2)**:

$$\boldsymbol{COP_{avg} = \frac{\int \dot{Q}_{evap}\ dt}{\int (\dot{W}_{compressors} + \dot{W}_{pumps} + \dot{W}_{fans})\ dt}} \qquad \textbf{(Eq.IV.2)}$$

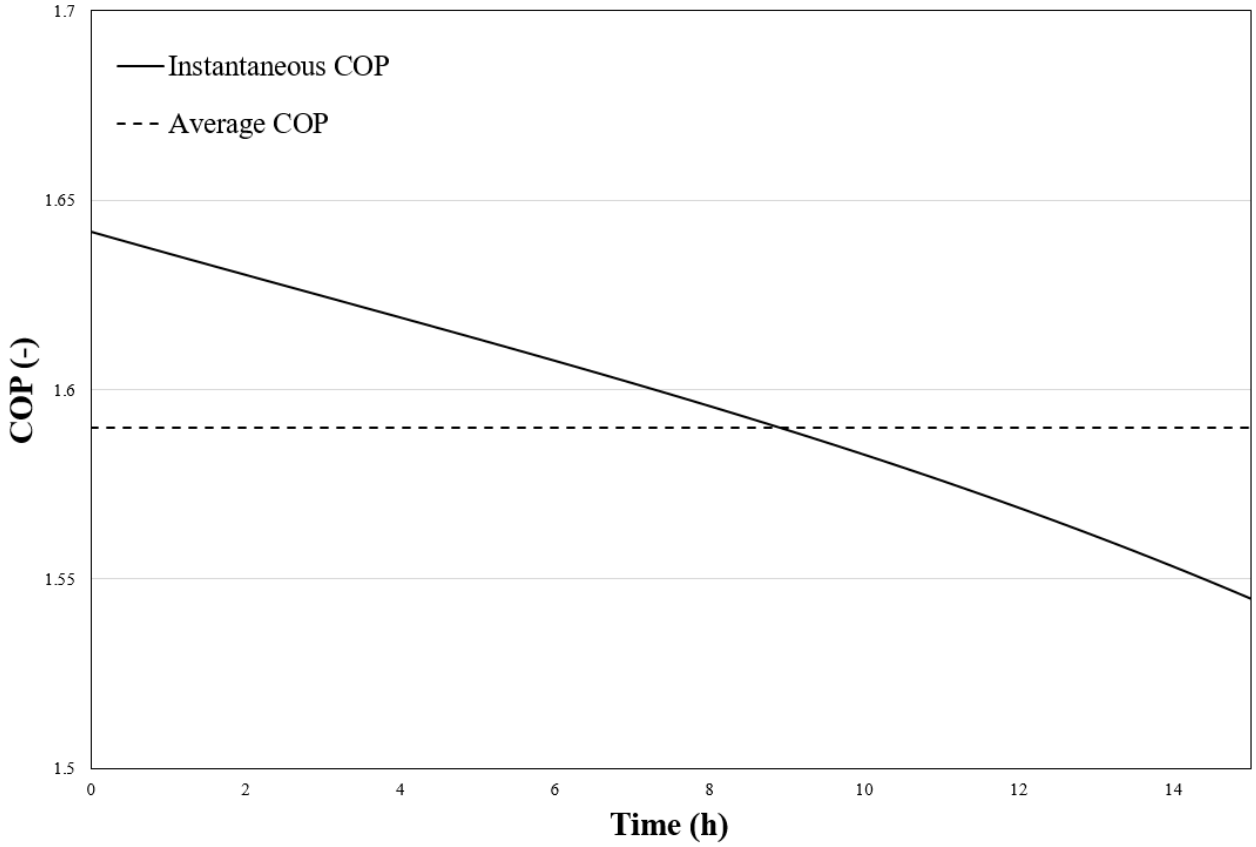

Figure IV.8: Instantaneous and average COP of the freezing system.

Focusing on **Figure IV.8**, we found that the instantaneous coefficient of performance decreases over time by about 7% compared to initial conditions, respectively. The initial COP was around 1.64.

The COP drop is not due directly to energy overconsumption but rather to the drop in cooling capacity. Once the latter is decreased, all the components of the freezing system including fans and compressors undergo this fall. As a result, the power of the compressors well as the power of the two fans coupled with evaporator and the cooling tower decreased. However, the rate of decrease is not the same between the part lost in cooling and the reduction in energy consumption. The cooling energy decreases by about 8% over 15 hours, while the energy consumed decreased only by 4%. **Figure IV.9** depicts the hourly energy consumed. It can be clearly seen that the large part of energy consumption is linked to the two HP and LP

compressors, which represent 52% and 35% of the total consumption, respectively. The freezer fan consumption represents 8% and the remaining 4% represent the consumption of the other auxiliary components: cooling tower fan and pumps. Since the compressors in the existing system can operate simultaneously with reduced capacities, this results in reduced energy efficiency of the part-load operation mode that cannot be avoided.

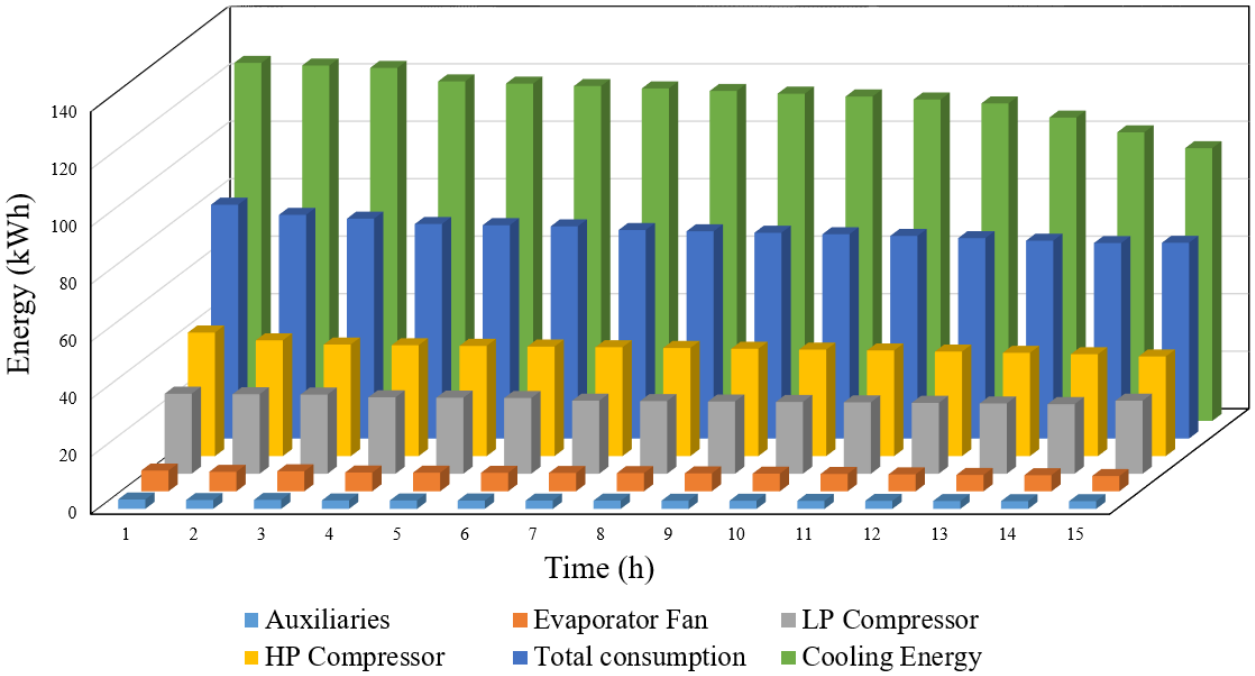

Figure IV.9: Cooling energy and energy consumption of each component of the freezing system as function of time.

IV.1-3. Product quality analysis

One of the most important results in the present study is the consideration of air-food interactions during freezing. Indeed, the frost accumulation effect is not only noticeable on the energy performance, but also on the product quality. This latter is affected by the raise in the air temperature inside the freezer and the degradation of the convective heat transfer coefficient between the air and the product.

To better identify this effect, a product quality variation over time is predicted. The objective is to estimate the outlet product temperature and the ice fraction in the frozen food from the energy balance equations between the air and the product. As was presented in previous chapter, the numerical model computes heat load as:

$$\dot{Q}_{air-produit} = \alpha_p \times A_p \times (T_{air} - T_{Product}) + \dot{m}_{water\ vapor} L_v \qquad \textbf{(Eq.IV.3)}$$

The term $\dot{Q}_{air-produit}$ represents the useful power used to cool down and freeze the product. This latter is frozen following three mean stages: Cooling down to the initial freezing temperature, freezing the constituent water and cooling down to storage temperature (**Figure IV.10**).

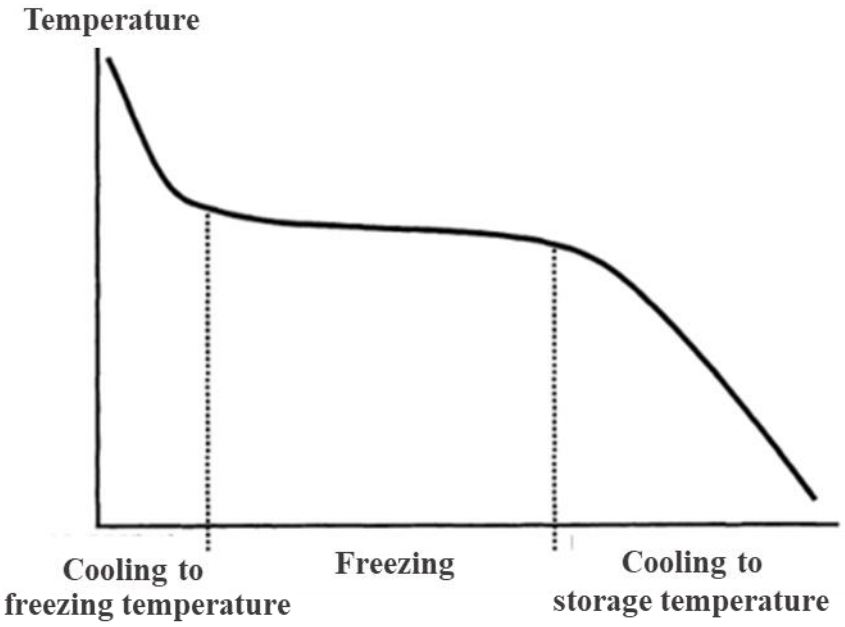

Figure IV.10: Practical definition of the freezing process.

The whole process could be mathematically expressed by equation **(Eq. IV.4)**. The product heat load is computed by considering sensible heat removable from initial temperature to freezing temperature, latent heat removal during phase change and sensible heat removal from initial freezing temperature to final temperature.

$$\dot{Q}_{air-produit} = \sum_{i=1}^{i=n} x_i \dot{m}_p c_{p_i} \left(T_{initial} - T_{freezing}\right) + x_i \dot{m}_p L_{f_i} + \sum_{i=1}^{i=n} x_i \dot{m}_p c_{p_{i_{below-freezing}}} \left(T_{freezing} - T_{final}\right) \quad \textbf{(Eq. IV.4)}$$

where $\dot{m}_p$ is the product mass flow rate, x_i is the mass fraction of the ith product ingredient, n is the number of ingredients and L_{f_i} is the latent heat of fusion.

Typically, in such a freezing process, the surface temperature of the food product drops quickly and generally reaches the phase change point in a short time comparing to the central temperature that drops slowly. With the advance of the phase change interface, the temperature difference between the food surface and the freezing medium decreases, and the surface

temperature drops more slowly. Also, the temperature gradient in the food increases, and the central temperature drops quickly until it almost reaches the phase change point. Thereafter, the central temperature reaches the phase change point and remains at this point for a long period. Meanwhile the surface temperature continues to decreases, etc. This freezing process may change depending on food properties and the freezing system parameters. In the present study, the product is considerably thin, therefore, and for the sake of simplicity its temperature is assumed to be homogenous ($\mathrm{Bi} = \frac{\alpha_p \times \delta_p}{2k_p} \ll 1$).

The second indicator of frozen product quality is the ice fraction. The latter is defined following the equation **(Eq.IV.5)**, assuming that the amount of the water contained in the fresh food is totally freezable.

$$x_{ice} = \frac{\dot{Q}_{air-produit} - \sum_{i=1}^{i=n} x_i \dot{m}_p c_{p_i} (T_{initial} - T_{freezing})}{\sum_{i=1}^{i=n} x_i \dot{m}_p L_{f_i}} \qquad \textbf{(Eq.IV.5)}$$

The food product properties of interest when considering the freezing process include thermal conductivity, specific heat, enthalpy and latent heat. These properties must be known for in the establishment of the exit food quality at the end of the residence time (42 min). The simple approach suggested below use the thermal properties of each ingredient in the pizza (**Table IV.1**) in order to solve the equations **(Eq. IV.4**) and **(Eq.IV.5)**.

Table IV.1: Pizza ingredients and thermal properties [169].

Pizza Ingredients	Water content (%)	Specific heat above freezing ($kJ.kg^{-1}.K^{-1}$)	Specific heat below freezing ($kJ.kg^{-1}.K^{-1}$)	Latent heat of fusion ($kJ.kg^{-1}$)
Tomato sauce	93.91	4.03	1.74	317
Ham	68.26	3.47	2.22	228
Cheese	54.14	3.15	2.46	185
Mushroom	91.81	3.99	1.84	307
Dough	60.21	2.71	1.62	140

Since the present approach is not based on a detailed physical model of the product, the evaluation of product quality is mainly based on ice fraction. This means that the product is considered as compliant if its ice fraction at the outlet of the freezer is equal to 100% regardless of its outlet temperature. Below this value, the product is considered as non-compliant. This rough approach does not claim to provide a precise evaluation of the quality of the product, but it provides an interesting indication in such a multi-criteria assessment.

In **Table IV.2**, we resume the thermal damage of the actual system operating under frosting conditions. Admitting that the freezing system works for 15 hours without any intervention, the amount of energy required is computed and the number of the compliant frozen pizza is determined. Finally, the specific energy consumption is deduced. The results reported showed quantified data about the energetic impact of frost discussed in previous sections. Both cooling and required energy decreases over time due to frost accumulation. One can notice that the frosting conditions have a direct effect on product quality and on productivity of the freezer. In this simulation, only 5510 compliant pizzas were insured by the actual freezer while 7200 compliant pizzas could be processed by the same freezer operating without frost. The specific energy consumption in this unfavorable operating mode is 33% higher compared to same reference. To give an approximate order of magnitude, the final temperature of the compliant frozen pizzas (100% of ice fraction) is increasing by about 0.03 °C/min during the day.

Table IV.2: Energy performance and food quality indicators at the end of one production day - 15 hours.

Energy performance and productivity	Dry conditions	Frosting conditions
Based on the same production time (15 hours)		
Cooling Energy (kWh)	1,898	1,760
Consumed Energy (kWh)	1,155	1,110
Average COP (-)	1.64	1.58
Number of compliant products	7,200	5,510
Specific energy consumptions (kWh/kg of compliant product)	0.10	0.13

IV.2. **Sensitivity Study and optimization strategies**

IV.2-1. Product water losses.

It is believed that the food water losses are considered one of the major source of humidity in such a blast freezer processing unpacked products. In present study, another factor that favors water migration during the freezing process is the high temperature of pizzas at the freezer inlet. For this, it is considered important to assess how much this factor could influence the freezing system behavior. A sensitivity analysis is therefore performed by varying the amount of product water losses. The reported results will also be discussed and analyzed in term of energetic performance and food quality indicators. Three quantity of water losses are evaluated. They are detailed in **Table IV.3**. For the three cases, all the initial properties of the products and

processing rate were kept similar; only the weight losses change. Case 0 represents the lowest amount of water losses, case 1 is the baseline conditions representing the actual real situation, and case 2 represents the most unfavorable case where the pizzas could lose up to 1.4% of their initial mass during freezing process.

Table IV.3: Summary of the numerical conditions for product water losses sensitivity analysis.

Case N°	**Product water losses (%)**	**Water migration mass flow rate (g/s)**
Case 0	0.8	1.6
Case 1 (Baseline Conditions)	1.1	2.2
Case 2	1.4	2.8

The first result to analyze is the cooling capacity of the evaporator. **Figure IV.11** depicts the effect of varying the amount of food water losses on the freezer cooling capacity. It is found that the heat transfer rate across the evaporator decreases gradually over time for the three cases. During the first hours of operation the cooling capacity decreases with approximatively similar trends. After about 8 hours, the decline become more significant for case 2 until it reaches 80 kW after 12 hours. The strong dependency of cooling capacity to the amount of water losses is obvious on **Figure IV.11**. For case 2, we notice a small oscillation of the model response after 12 hours. This is purely due to numerical resolution. If the cross section area blocking ratio would reach 100%, the air volume flow rate had to be zero which is a structural issue in

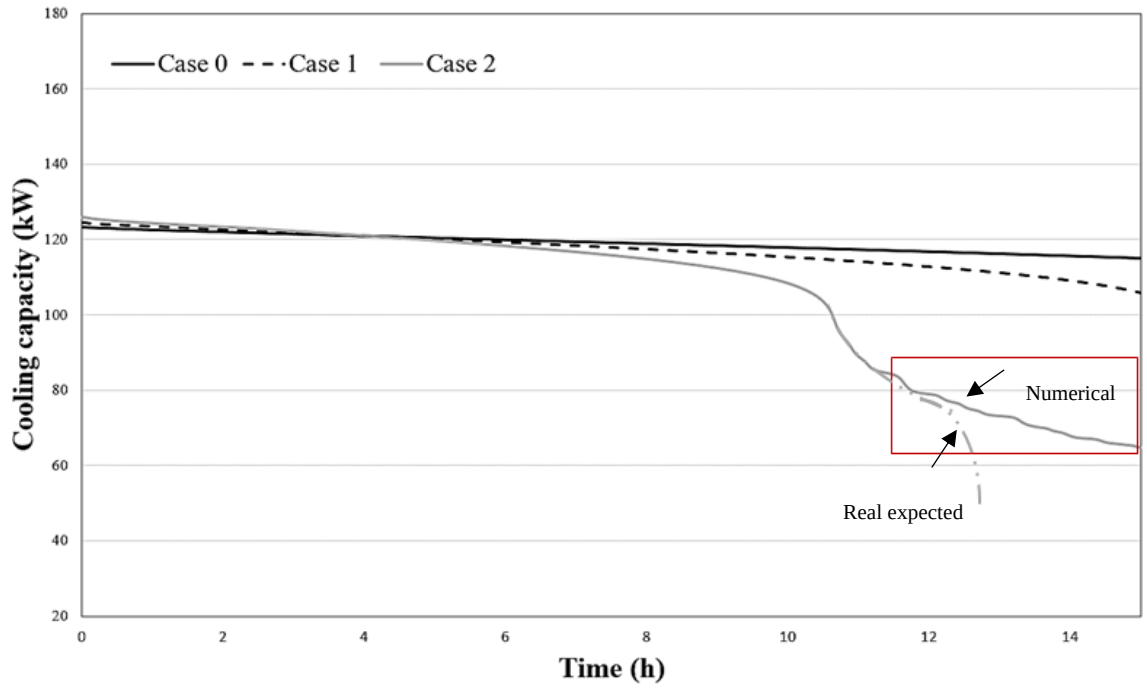

Figure IV.11: Effects of food water losses on cooling capacity.

numerical resolution. For this reason, above 90% of cross section area blockage, the model considers a slowdown of frost accumulation managed numerically by smooth transition so the blockage ratio can approach 100% but not reach it. This means that the variation trend beyond 12 hours does not really represent the correct evolution. Generally, once a row is blocked, the volume airflow rate and the cooling capacity fall rapidly. Within 12 hours, the cooling capacity decreases by about 4% for 0.8% water losses, 10% for 1.1% water losses and 35% for 1.4% water losses. These different results are likely due to the strong dependence of the amount of frost to the amount of water vapor transferred from the product to the air.

The results reported on **Figure IV.12** show that an increase in the product water losses causes a decrease in the volume airflow rate. Such a behavior is explained by the increase in the air pressure drop through the evaporator that affect the airflow rate depending on the fan characteristics. As for cooling capacity, the initial operating point is slightly deflected, and the performance are not highly deviated in case 0. However, in case 1, and case 2, the difference is largely clear and the airflow rate decreases rapidly and fall within 9 hours in case 2. This means that the cooling capacity follows roughly the same behavior as the air volume flow rate, highlighting that the former has a major impact on performance degradation. The fan operating point at different moment for the three cases is illustrated in **Figure IV.13**. One can observe that for case 2, and above 12 hours, the operating point gets closer to the fan stall region.

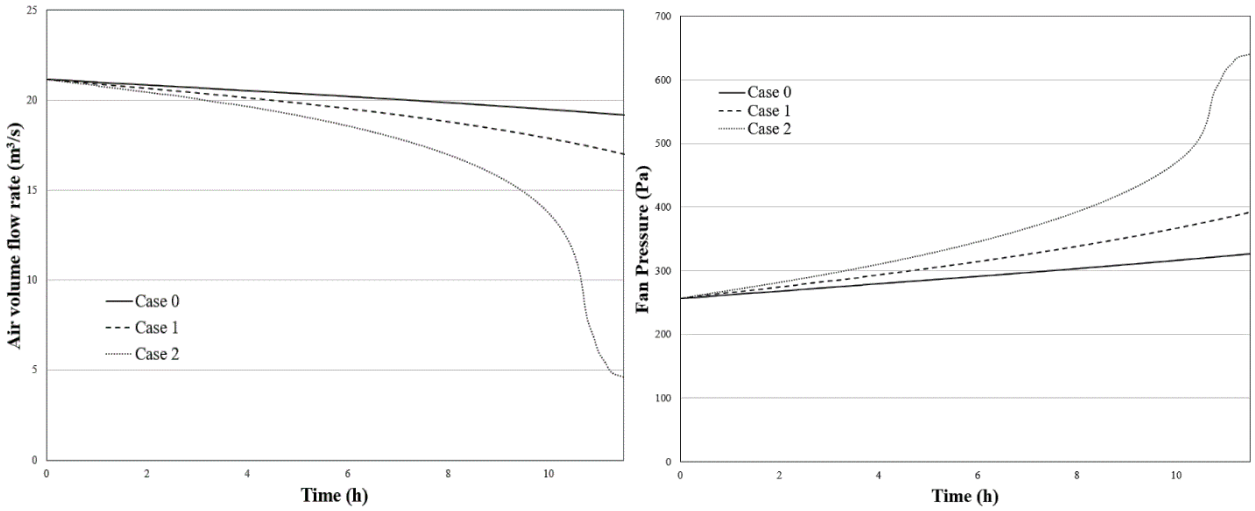

Figure IV.12: Sensitivity of the airflow and pressure drop to food water losses.

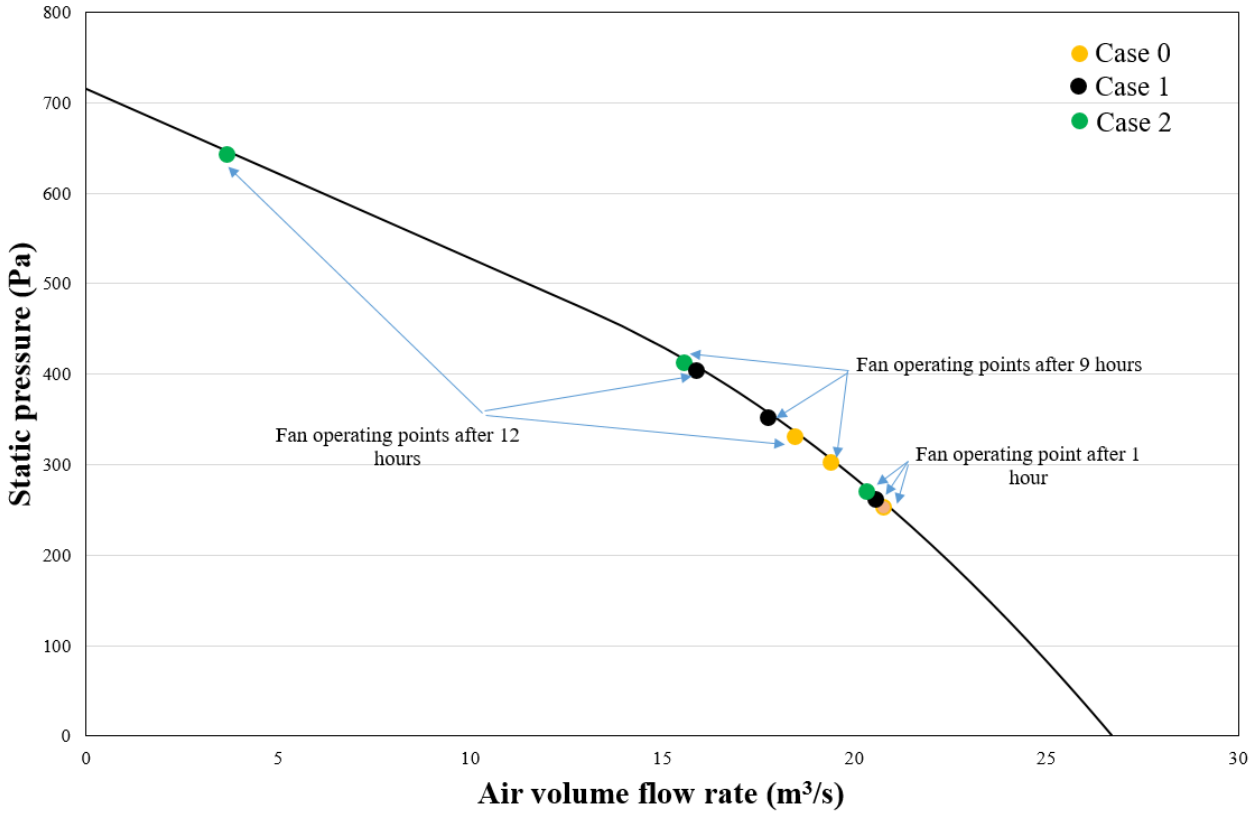

Figure IV.13: Fan operating points for different amount of product water losses

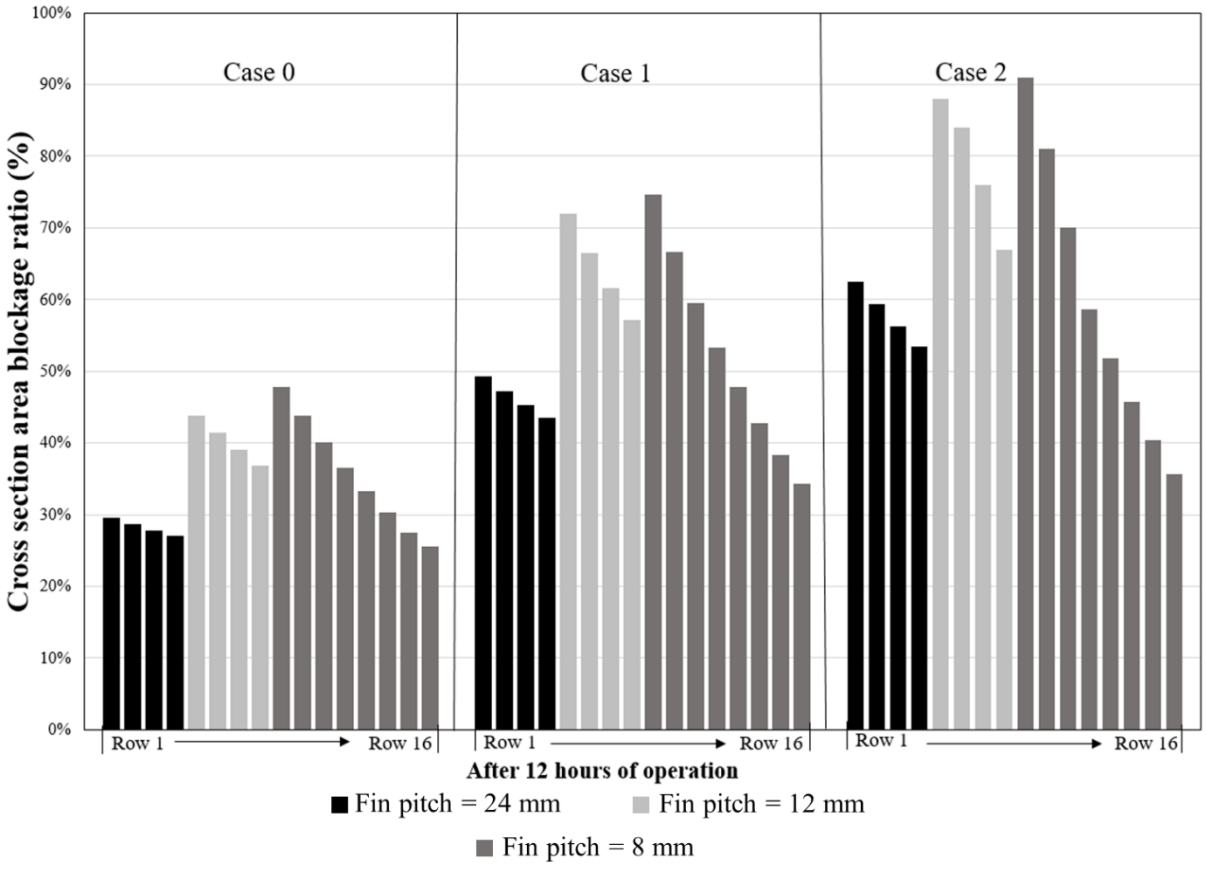

Figure IV.14: Cross section area blockage ratio for different amounts of moisture released by products.

Another interesting observation should be emphasized on the local distribution of frost through the airflow direction. The fraction of the free flow area at different location of the heat exchanger is represented in **Figure IV.14**. It shows that the amount of water vapor contained in the air does not affect the distribution of the frost over the heat exchanger. Moreover, it can be noted that the cross section area at the 5th and 9th row of the heat exchanger is reduced, within 12 hours, by about 45%, and 50% in case 0, and by 72% and 76% in case 1, and by 84 and 98% in case 2. However, the frontal section area has been only reduced by 30%, 49% and 62% in case 1, 2 and 3, respectively. Moreover, it can be observed that the cross section area blockage ratio decreases through the first 4 tube rows having the same fin pitch. Across these rows, only the air properties vary in the airflow direction. However, when increasing the number of fins per tube row at the 5th row then at the 9th row, the blockage ratio increases as well. It observed that the blockage ratio is maximum on the 9th for the three cases.

To clearly visualize the frost distributions and the blockage rate, the geometry of the evaporator is divided into four sections with the same number of tubes in the direction of airflow. As represented in **Figure IV.15**, the first three sections will represent the effect of fin pitch varying from 24 mm to 8 mm with fixed tube rows, and the last is the outlet section with the same 8 mm fin pitch as the third. **Figure IV.16** shows that frost mass per area decreases through the evaporator. The leading edge has larges gradients of humidity and temperature compared with the values of gradients at the exit region. However, it is observed that the first and second middle

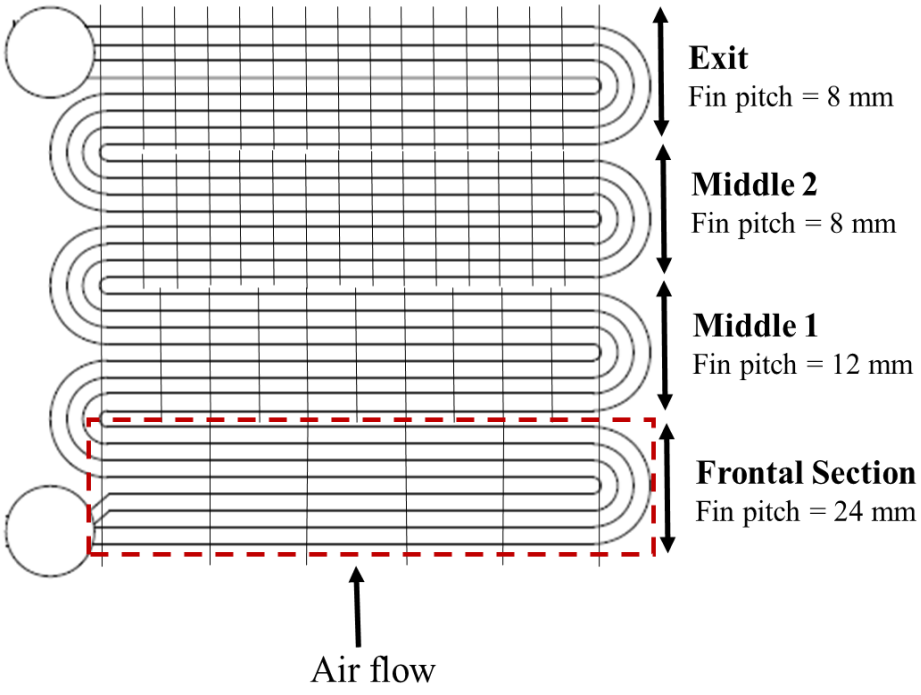

Figure IV.15: Schematic of evaporator geometry sections for frost mass analysis.

sides get rapidly blocked although the rest of sections, namely the frontal and exit, weren't even half blocked in both case 0 and case 1. Because fin pitch decreases through the air direction, the heat transfer area increases, leading to a faster blockage rate in both middle sides in the three cases.

A larger inlet fin pitch could be useful choice in an optimal design to trap the maximum amount of frost upstream of the evaporator. However, the digressive fin pitch of the actual evaporator is not sufficient to maintain the energy performance and extended time between defrost cycles. A general design shall attempt not to have uniform distribution of the amount of frost accumulated through the airflow direction, but to achieve uniform blockage ratio throughout the heat exchanger.

The blockage of the fin gap is not the only cause linked to the reduction in performance but obviously the thermal resistance of frost mainly linked to its density.

Table IV.4 resumes the average frost density on the whole evaporator within 12 hours for the three cases.

The effects of varying the amount of water vapor transferred from the food to the air is clearly shown on frost density. The frost layer is more porous when increasing the air humidity that passes from 91% in case 0, to 95% in case 1, and then to 98% in case 2. This is due to the large increase of the surface temperature of the frost in case 2 compared to case 1 and 0. The latter increase results from the rapid growth of the frost layer with a low density due to the large driving potential of the mass transfer with increasing humidity.

The relation between frost densification and air humidity is not as evident as frost growth. There are several parameters varying simultaneously in each time step influencing the next one in different ways going from case 0 to case 2. A large quantity of water vapor quickly boosts heat and mass transfer. This tends to reduce more and more the airflow path, thus affecting the flow rate and the air velocity depending on fan behavior. The air temperature and frost surface temperature vary as well. Therefore, the dominance of one phenomenon over another is not so obvious.

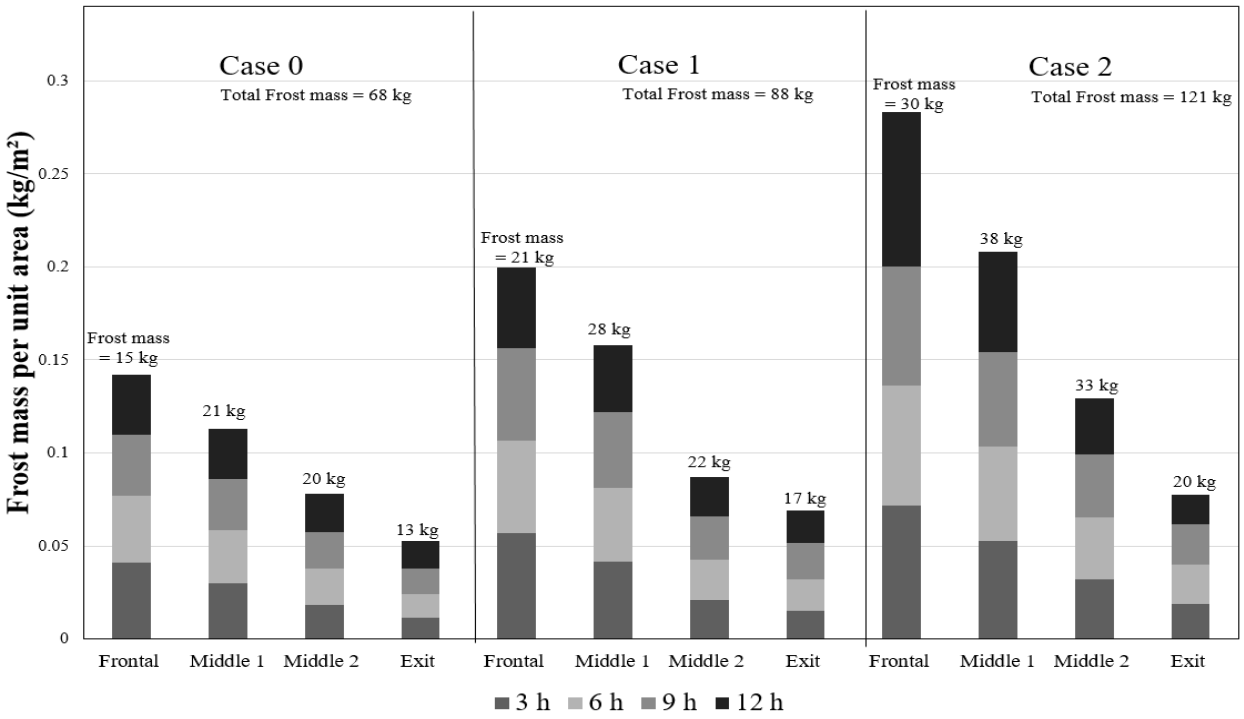

Figure IV.16: Frost mass for different amounts of moisture released by products.

Table IV.4: Sensitivity of frost properties to food water losses.

Frost growth	**Case 0**	**Case 1**	**Case 2**
Ratio of frost densification and total mass transfer (%)	17	10	6
Average frost density (12 hours) (kg/m^3)	65	52	45
Thermal conductivity (W/m/K)	0.152	0.148	0.145

The results obtained in the present study showed that the weight loss of food during freezing could highly modify the freezing parameters within time, thus affecting the food itself. As presented in **Figure IV.17**, the air velocity does not show significant slope on case 0 and the air-product convective heat transfer coefficient decreases only by about 5% within 12 hours. In case 1, the air velocity decreases from 4.32 m/s to 3.4 m/s, and the air-product heat exchange quality decreases by about 10%. Case 2 reaches 15% drop in convective heat transfer coefficient within only 10 hours of operation. After 10 hours, the air velocity is almost decreased and the decrease rate becomes more brutal reaching 0.8 m/s at T0+12. Bringing the analysis to the system level, we report the performance, quality and productivity indicators for the 3 cases, within 12 hours of operation, in **Table IV.5**.

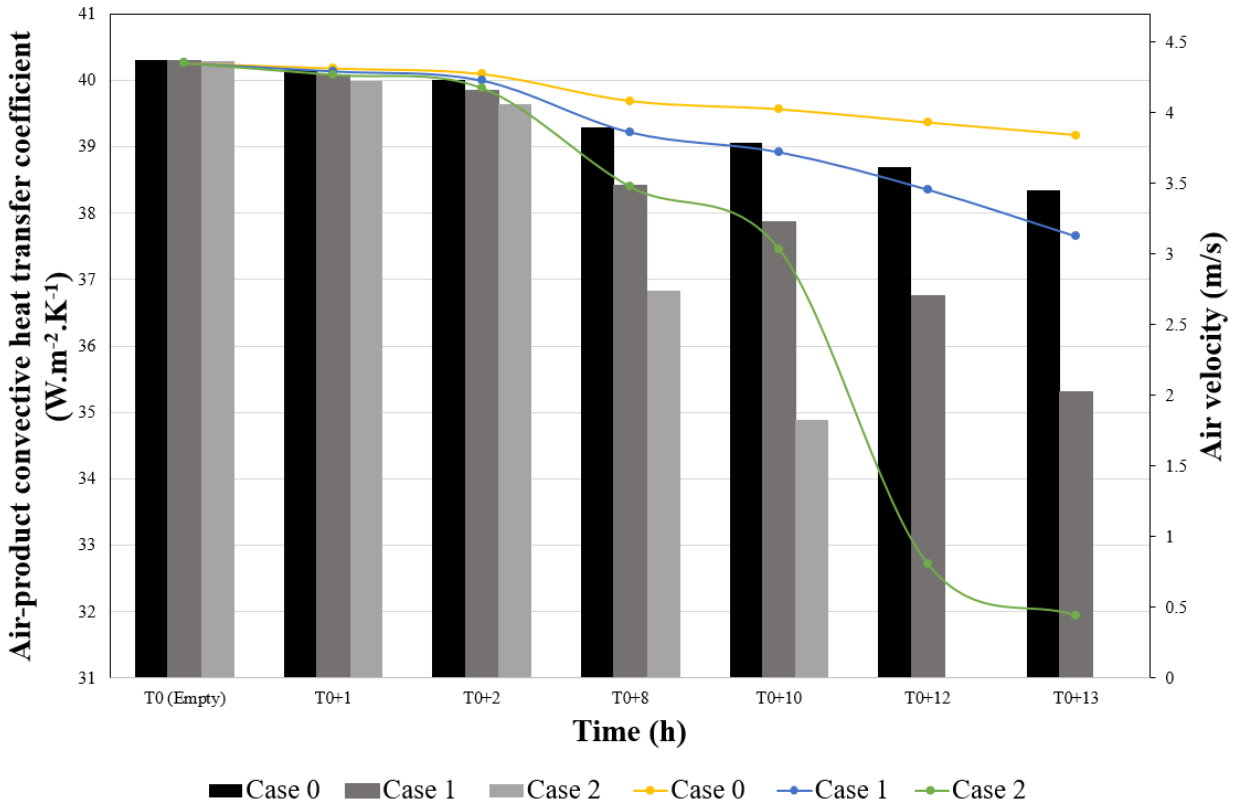

Figure IV.17: Air-product heat transfer coefficient and air velocity depending on product water losses.

Table IV.5: Sensitivity of energy performance and food quality to food water losses within 12 hours.

Energy performance and productivity	**Case 0**	**Case 1**	**Case 2**
Based on the same production time (12 hours)			
Cooling Energy (kWh)	1,473	1,450	1,380
Consumed Energy (kWh)	910	901	882
Instantaneous COP after 12 h of operation (-)	1.6	1.57	1.43
Average COP (-)	1.62	1.61	1.56
Number of compliant products	5,760	5,505	4,080
Specific energy consumption (kWh/kg of compliant product)	0.1	0.1	0.13

One can observe that the cooling energy and the consumed energy both decrease going from case 0 to case 2. Analyzing over 12 hours of operation, the difference is not so wide between case 0 and 1. This is due to the freezing parameters, which are quite similar during the first hours of operation between the two cases (e.g., air velocity and temperature). However, we can clearly observe the impact that could happen on productivity. Regarding case 2, the results indicate the poor energy performance represented also by the lower coefficient of performance

compared to the case 0 and 1. In these most unfavorable conditions, the freezer is able to maintain food quality only for 8.5 hours before requiring a defrosting cycle. In order to avoid the deterioration in the performance of the freezing system and the product quality, defrosting should start before the heat transfer reduces drastically. This time is around 17 hours, 11.5 hours, and 8.5 hours in case 0, case 1, and case 2, respectively. Extending the analysis over one production day, we must therefore count the defrost duration and consumption for both case 1 and 2. In conditions of case 0, the freezer can continue to operate throughout the day without the need for intervention to remove the frost.

IV.2-2. Fan control mode

Although a large number of studies have been carried out on investigating the frosting behaviors and its impacts on finned tube heat exchangers, comparative studies for frosting behavior and frost impact using different control modes were still lacking. Hence, a sensitivity study comparing two different air fan control modes is carried out.

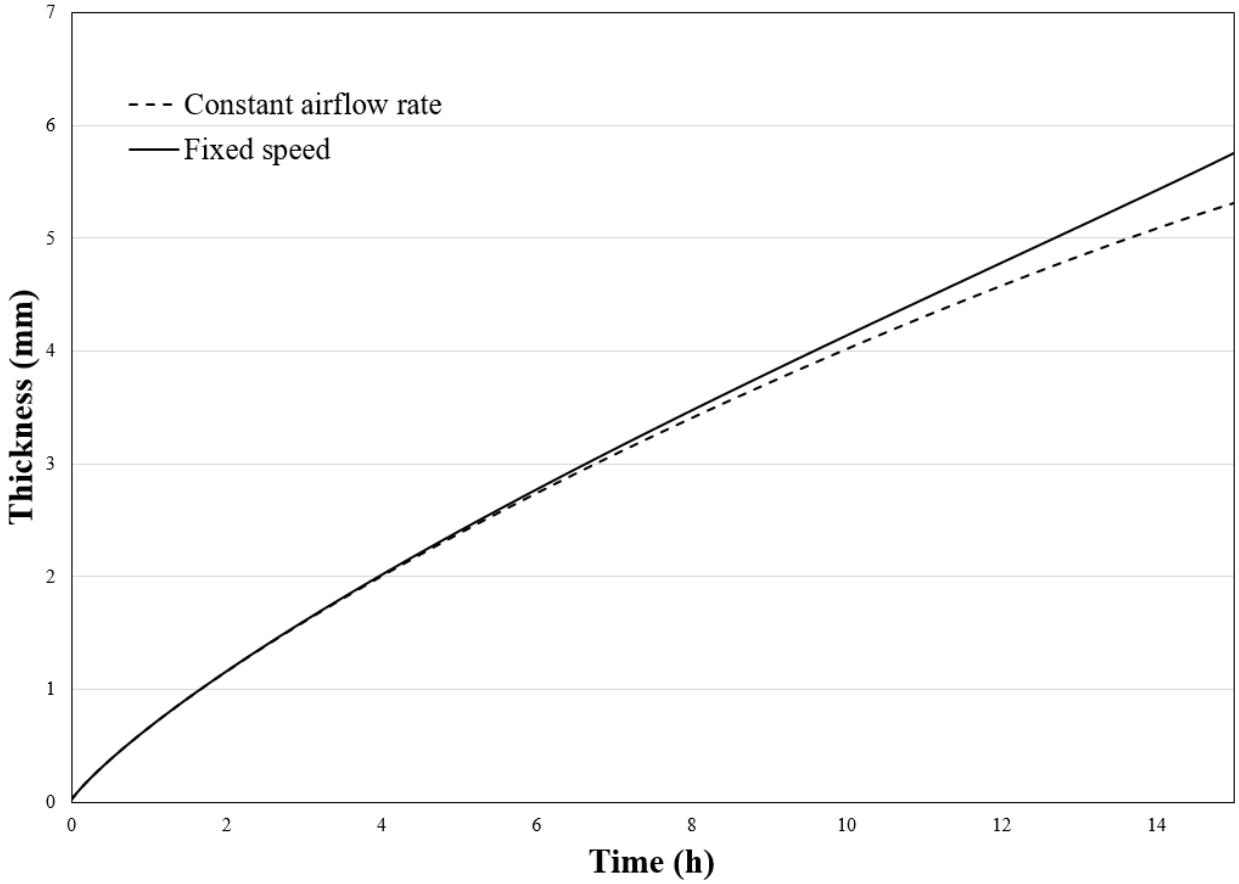

Figure IV.18: Frost thickness at the leading edge under different fun control modes.

Two types of fan control modes are compared. The first is the same as the default baseline conditions on case 1 with a variable air flowrate VAF (constant speed). The second control mode is a variable speed fan to maintain a constant airflow rate CAF during frosting.

Comparing the frost layer properties, it was noted that the frost under the constant airflow rate control mode was slightly thinner than that under the constant outdoor air fan speed control mode. As seen in **Figure IV.18**, the frost thickness under CAF control mode and that under the VAF control mode was nearly similar during the first 10 hours. After this period, the differences between the two modes started to increase, which was believed to be mainly due to the air velocity.

The air velocity under the two fan control modes were both increased gradually as frosting progressed, but the increasing rate in air velocity under the CAF control mode was much larger than that under the VAF mode. This was particularly true when the air passages for the evaporator was largely blocked.

At 10 hours, the averaged inlet air velocity to the evaporator under the CAF control mode was at 16% greater than that under the constant fan speed control mode. Beyond 10 hours, air velocity under the CAF control mode reached was 30% greater than that under the VAF control mode. On one hand, an increased air velocity can lead to an increased heat transfer. Based on the Lewis analogy, mass transfer was also increased, leading to an increase in frosting rate and hence frost thickness. From this point of view, an increased air velocity positively affected frost growth with respect to its thickness. On the other hand, an increased air velocity can also lead to an increased frost surface temperature, leading to a decreased moisture content difference between air stream and frost surface, namely the driving force for frosting, and consequently a reduced frosting rate and hence frost thickness. The overall trends of the frosting rates for the frosted evaporator under both fan control modes were decreased as frosting progressed. However, the main reasons for the decreasing frosting rates under two fan control modes were different. Under the constant airflow rate control mode, the main reason was a continuously increased frost surface temperature caused by increased frost thickness and air velocity. On the other hand, under the constant outdoor air fan speed control mode, the main reason was a combined effect of an increased frost surface temperature and a decreased amount of moisture content in the air because of a decreased airflow rate.

Despite the small difference in the aspect of frost between the two control modes, it is interesting to analyze the effect on the cooling capacity of the freezer under the two modes in order to highlight the impact of the airflow reduction on the cooling capacity. As depicted in **Figure IV.19**, the cooling capacity reduces by 19% under fixed speed control mode while it reduces only by 7% when maintaining the air volume flow rate, thus believing in the dominance of the air side convective resistance due to the air path blockage.

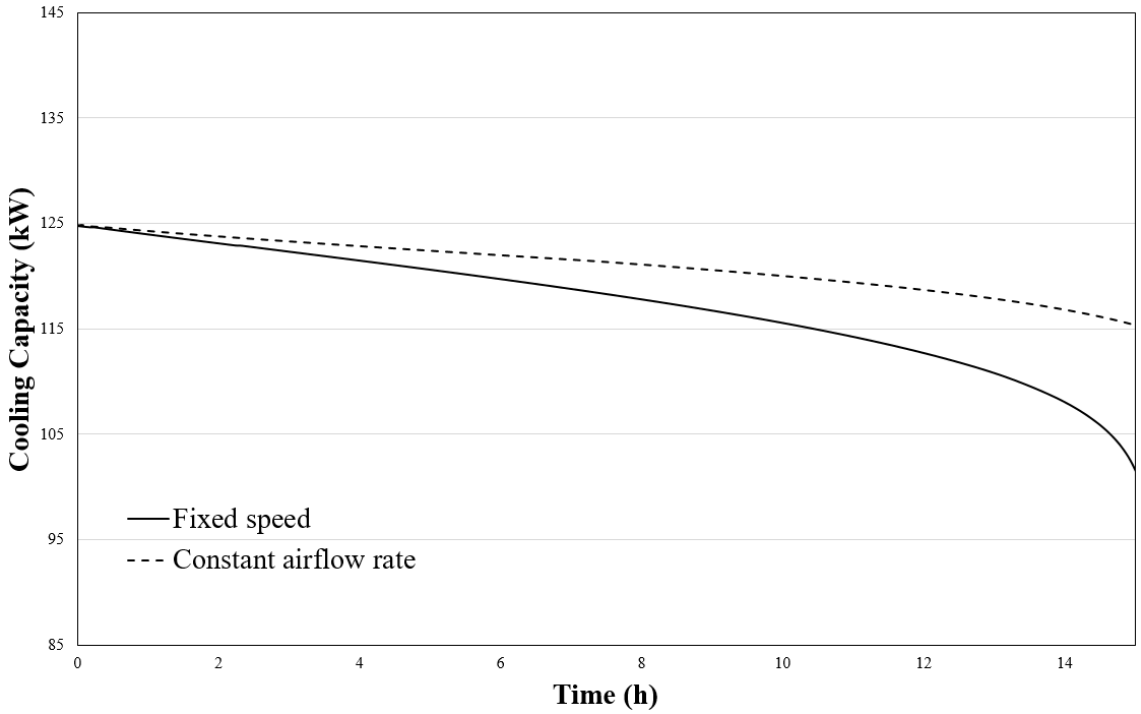

Figure IV.19: Cooling capacity versus time under different fan control mode.

Assuming that two freezers each operating with a control mode during 12 hours, the energy performance and the productivity of each industrial site during this day are summarized in **Table IV.6**.

Table IV.6: Energy performance and productivity under different fan control modes.

Energy performance and productivity	**Constant airflow rate**	**Fixed speed**
Based on the same production time (12 hours)		
Cooling Energy (kWh)	1,461	1,450
Consumed Energy (kWh)	945	901
Average COP (-)	1.55	1.57
Number of compliant products	5,760	5,505
Specific energy consumption (kWh/kg of compliant products)	0.10	0.10

The difference is not that much when comparing the energy performance. This is due to the production duration time suggested as 12 hours and defined as the maximal duration of the baseline mode to freeze food adequately.

Extended the analysis on 15 hours - daily production duration - the freezer operating with a constant airflow is able to maintain food quality without need to defrost. However, the energy consumed will be a penalty in this case since the fan shaft power of the variable speed fan highly increases with time (**Figure IV.20**).

As can be seen in **Figure IV.20**, the shaft power of the fixed speed mode decreases over time. However, within 15 hours, the shaft power requested by the variable speed fan increases from 7 kW to approximatively 30 kW.

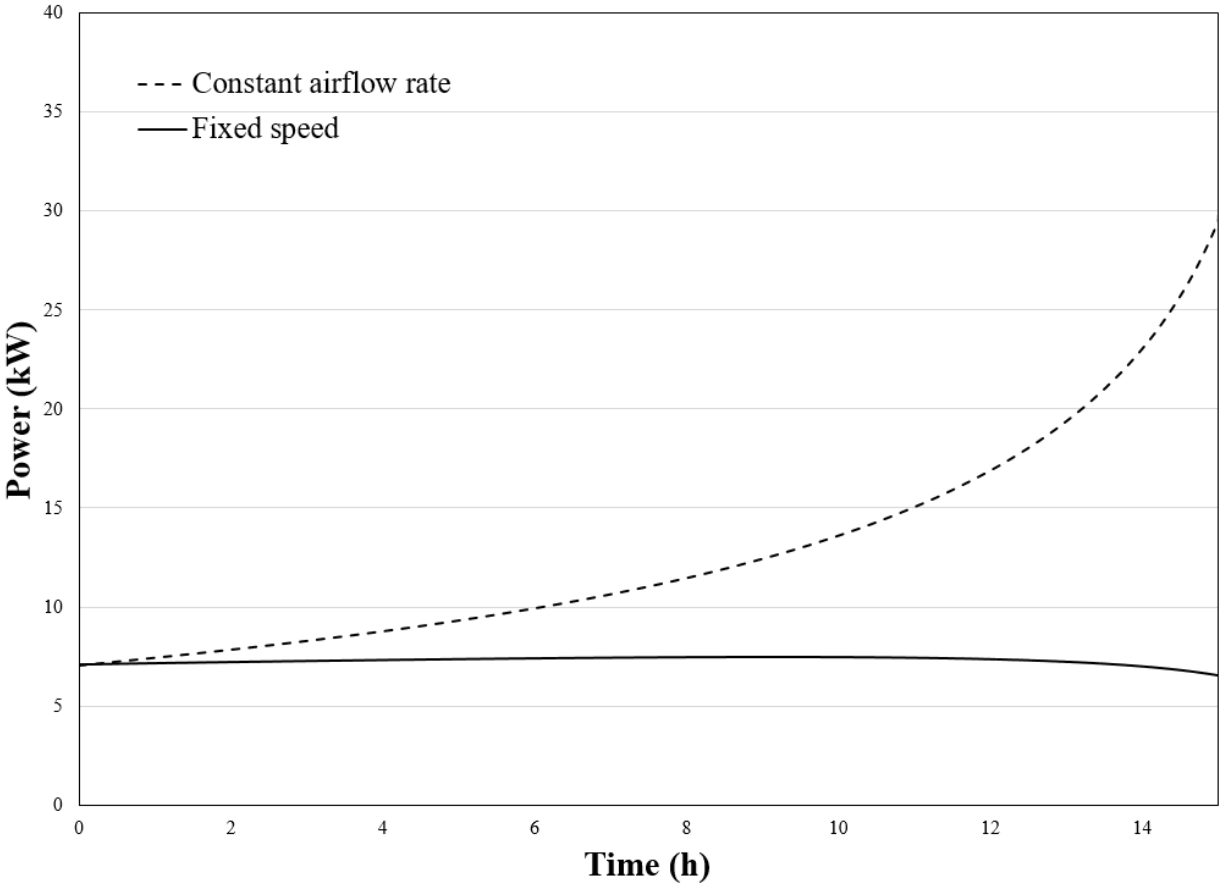

Figure IV.20: Fan shaft power under different control modes

IV.3. **Summary**

It can be inferred that frosting is a complex phenomenon that deteriorates the cooling capacity of a freezer and the overall performance of the freezing system. Each system component is affected by what happens in the refrigeration space.

Depending on control mode in such a two-stage system, the compressors tend to maintain the pressures in the tank separators. Based on an adjustment by a power driver, the compressor efficiencies showed a high sensitivity to a small variation in the cooling capacity.

The effect does not concern only energy, but also productivity and product quality. The reduction of the airflow section, reduction of airflow linked to the air side pressure drop, the increase in the air temperature inside the refrigerated space, are all consequences of the formation of frost which modifies freezing parameters.

The product being very sensitive to these parameters, and especially to the convection exchange coefficient linked to the air velocity, deteriorates as the frost builds up.

The actual design of the industrial evaporator is based on a digressive fin pitch in the direction of the airflow. This choice is justified by the fact that a large pitch of fins at the leading edge makes it possible to receive the large quantity of moisture at the evaporator entrance without blocking the flow path. The choice of fin pitch distribution on the rows of the tubes is not always obvious and could not absolutely help to avoid the non-uniformity of frost. This means that when adopting this configuration, the cross section area of many fin rows still tend to block before the others requesting a defrost initiation. This suggest that selecting the fin pitch that provide uniform blockage ratio may lead to a longer operation time.

In the present case studied in this thesis, the products are considered the major source of humidity in the refrigerated space. A sensitivity study to the quantity of water was carried out highlighting the great sensitivity of the frosting rate, energy performance, and product quality to food weight losses.

Conclusions and future works

The objective of this thesis was to develop a numerical model to dynamically study the frosting phenomenon in an industrial food freezer in order to quantify the penalties associated with frost accumulation in terms of system energy performance and food quality. This work benefited of an experimental campaign performed in the framework of the ADEME FOODEFREEZE project, on a freezing system with an ammonia two-stage compression system. This spiral air blast freezer operates at -40 °C and processes 480 pizzas/h entering at an initial temperature of 40 °C and releasing 7.9 kg of water per hour during freezing. The evaporator subjected to frost accumulation is a flooded evaporator supplied by a recirculating pump. It is a finned tube heat exchanger with a digressive fin pitch in the airflow direction. At nominal conditions, the air inlet temperature is around -35 °C and apparent air velocity is equal to 4.32 m/s.

To reach the objective of this thesis, several approaches were adopted using the open-access language Modelica with the environment software Dymola.

A local approach aimed to determine the frost characteristics depending on operating conditions: A physical model was developed for predicting the frost growth. The model was first validated by experimental data from the literature for both heat pump and freezing conditions. Thereafter, local phenomena of mass and heat transfers from the airflow to the frost layer surface and inside the first layer have been discussed. It was found that the frost layer formed in freezing conditions, characterized by very low evaporating and air temperature and high air velocity, is less dense compared to the frost formed in refrigeration and heat pump applications.

The frost model was integrated as a sub-model of the freezing system evaporator modeled with a finite volume approach. The evaporator model is connected to a fixed speed fan model defined by its characteristic curve. A screw compressor model, whose capacity is controlled by a slide valve, was developed based on constructor data. The models of the other components (tank separators, condenser, cooling tower, pumps and valves) were selected and adapted from thermal systems and building libraries. A relatively basic approach was adopted in order to model the product taking into consideration its sensible and latent heat loads.

The slide valves of both low and high pressure compressors are controlled in order to maintain pressure in the tank separators. The filing level of the medium tank separator is maintained constant by controlling the valve opening section.

First, the numerical results were compared with data obtained on the industrial food freezing system during one production day over 15 hours. The numerical model shows good prediction and trends similar to those observed experimentally, such as reduction of the airflow cross-section, air-side pressure drops, and decreased air-product convective heat transfer coefficient.

The numerical model was then exploited to bring both local and system level analysis:

- At the scale of the evaporator, the frost appears to be thicker at the leading edge than at the evaporator outlet.
- In these freezing conditions, the frost density is very low compared to the density of frost that formed in heat pump conditions. This is due to the low temperature that promotes vapor desublimation on the frost surface before the water vapor could diffuse inside the frost layer. The mass flux diffusion inside the frost layer represents only 10% of the total water vapor mass flux transferred from the air to the frost surface. After 15 hours, the average frost density was around 55 kg/m3.
- As frost build-up, the free cross section area decreases resulting in an increase of pressure drops and a decrease of the air volume flow rate supplied by the fan. Moreover, the low thermal conductivity of the frost layer adds an additional thermal resistance between the air and the refrigerant. Both convective and conductive thermal resistances led to a degradation of the cooling capacity by about 19%.
- In such freezing system operating with specific control mode, all the components undergo the cooling capacity reduction. The compressors efficiencies showed a high sensitivity to this degradation and a small variation of the slide valve of 4% led to a high decrease in compressors efficiencies by about 17%, thus affecting the average performance coefficient.
- The average performance coefficient COP decreased by 5%.
- Under these conditions, the freezer could maintain the final food quality only for 12 hours. After this time, defrosting should be initiated.

Important new results were found:

- Usually, the heat exchanger geometry with a uniform fin pitch has a maximum blockage rate in the first row at the leading edge. However, the finned tube evaporator with digressive fin pitch shows a different behavior. This study points out that the cross section area of the middle side of the evaporator is more blocked than the leading edge side. This result could help for a new design of evaporators that would ensure a longer

time between successive defrost cycles. A uniform cross section area blockage ratio could be the optimal configuration to avoid the early blockage of few rows that leads to abrupt performance degradation. An optimization procedure could be proposed to find the adequate distribution of fin pitches across the evaporator that would lead to a uniform cross section area blockage.

The numerical model was also exploited to conduct sensitivity analyses. Local phenomena, system behavior, food quality and productivity were analyzed for different amounts of moisture released from the product during freezing. As expected, a large amount of moisture led to a high performance degradation and poor productivity. To maintain final food quality, the freezer would operate for more than 17 hours in the case where the food products lose 0.8% of their initial weight during freezing. However, it would operate only for 12 hours, and 8 hours if the products lose 1.1% and 1.4% of their initial weights, respectively. A precooling of the product is recommended to limit these harmful weight losses.

Since the decrease of the volume airflow rate is one of the major causes leading to decrease of the cooling capacity, two fan control modes were compared. The fixed fan speed, which is the actual fan of the freezing system, and the variable fan speed which keeps the volume air flow constant. The second maintains the freezer performance and food quality for longer time compared to the baseline mode. However, the shaft power of the variable fan speed increases greatly over time.

These numerical results obtained on a complex freezing system, following an object-oriented approach, could guide manufacturers in managing production strategies, product quality and defrosting sequences. They could also be useful to design engineers for the selection of the geometrical parameters of evaporators in order to extend the operating time between two successive defrosts.

While this thesis continues to advance the dynamic modeling capabilities of freezing systems, the following points could further improve research in this area and most likely make the developed modeling system more useful to industry.

The present system level modeling approach serves two purposes in general: 1) to explore the system behavior under frosting conditions and 2) to design and evaluate control strategies. As this thesis has mainly focused on the first aspect, more suitable models for controller design must be developed to achieve the second objective.

Further works could be firstly devoted to improving the model that addresses product quality during the freezing process. The distribution of temperature and ice content inside the food would provide more accurate results.

A more important step is to consider defrosting phenomena. Models need to be developed to improve the analysis and get closer to industrial system configurations. More complete information could be obtained by adding energy data related to defrosting.

Finally, a rigorous experimental validation must be conducted on both frosting and defrosting in freezing conditions. In this thesis, only few data from experimental measurements have been used to make the model more reliable. More experiments can improve the understanding of these processes and in turn complete the numerical studies.

References

[1] D. Coulomb, “Refrigeration and cold chain serving the global food industry and creating a better future: two key IIR challenges for improved health and environment,” *Trends Food Sci. Technol.*, vol. 19, no. 8, pp. 413–417, Aug. 2008.

[2] S. J. Vermeulen, B. M. Campbell, and J. S. I. Ingram, “Climate Change and Food Systems,” *Annu. Rev. Environ. Resour.*, vol. 37, no. 1, pp. 195–222, Nov. 2012.

[3] S. G. Sutariya and V. Sunkesula, “Food Freezing: Emerging Techniques for Improving Quality and Process Efficiency a Comprehensive Review,” in *Innovative Food Processing Technologies*, Elsevier, 2021, pp. 36–63.

[4] S. Schudel, K. Prawiranto, and T. Defraeye, “Comparison of freezing and convective dehydrofreezing of vegetables for reducing cell damage,” *J. Food Eng.*, vol. 293, p. 110376, Mar. 2021.

[5] M. Sadot, S. Curet, S. Chevallier, A. Le-Bail, O. Rouaud, and M. Havet, “Microwave assisted freezing part 2: Impact of microwave energy and duty cycle on ice crystal size distribution,” *Innov. Food Sci. Emerg. Technol.*, vol. 62, p. 102359, Jun. 2020.

[6] L. Bøgh-Sørensen, *Recommendations for the Processing and Handling of Frozen Foods.* IFF-IIR, 2006.

[7] P. Dempsey and P. Bansal, “The art of air blast freezing: Design and efficiency considerations,” *Appl. Therm. Eng.*, vol. 41, pp. 71–83, Aug. 2012.

[8] W. A. Johnston, *Freezing and refrigerated storage in fisheries*. Food and Agriculture Organization of the United Nations, 1994.

[9] P. Dempsey and P. Bansal, “Air blast freezers and their significance to food freezing: A Review, Proceedings of the 13th Brazilian Congress of Thermal Sciences and Engineering, 2010, Uberlandia, Brazil.”

[10] G. V Barbosa-Cánovas and P. Juliano, “Symposium 3 Part 2: The Food Chain: Food Processing and Food Safety Adaptation of Classical Processes to New Technical Developments and Quality Requirements,” 2004.

[11] B. T. Marinyuk, “Heat and mass transfer under frosting conditions,” *Int. J. Refrig.*, vol. 3, no. 6, pp. 366–368, Nov. 1980.

[12] T. Hosoda, “Effects of Frost on the Heat Transfer Coefficient,” *Hitachi Hyoron*, vol. 49, no. 6, pp. 647–651, 1967.

[13] A. A. Aganda, J. E. R. Coney, and C. G. W. Sheppard, “Airflow maldistribution and the performance of a packaged air conditioning unit evaporator,” *Appl. Therm. Eng.*, vol. 20, no. 6, pp. 515–528, Apr. 2000.

[14] C. T. Sanders, “Frost formation: The influence of frost formation and defrosting on the performance of air coolers.” Ph.D. dissertation, Faculty of Mechanical, Maritime and Materials Engineeing, 1974.

[15] X.-M. Guo, Y.-G. Chen, W.-H. Wang, and C.-Z. Chen, “Experimental study on frost growth and dynamic performance of air source heat pump system,” *Appl. Therm. Eng.*, vol. 28, no. 17–18, pp. 2267–2278, Dec. 2008.

[16] M. Heim, “Etude du givrage et du dégivrage d’évaporateurs de chambre froide - Optimisation expérimentale.,” Laboratoire d'Energétique et Automatique, Lyon, Tech.

Rep, 1989.

[17] M. Amer and C. C. Wang, “Review of defrosting methods,” *Renew. Sustain. Energy Rev.*, vol. 73, no. January, pp. 53–74, 2017.

[18] G. Mader and C. Thybo, “A new method of defrosting evaporator coils,” *Appl. Therm. Eng.*, vol. 39, pp. 78–85, 2012.

[19] Q. Ma, X. Wu, F. Chu, and B. Zhu, “Experimental and numerical investigations of frost formation on wavy plates,” *Appl. Therm. Eng.*, vol. 138, pp. 627–632, Jun. 2018.

[20] X. Wu, S. Hu, and F. Chu, “Experimental study of frost formation on cold surfaces with various fin layouts,” *Appl. Therm. Eng.*, vol. 95, pp. 95–105, Feb. 2016.

[21] R. O. Piucco, C. J. L. Hermes, C. Melo, and J. R. Barbosa, “A study of frost nucleation on flat surfaces,” *Exp. Therm. Fluid Sci.*, vol. 32, no. 8, pp. 1710–1715, Sep. 2008.

[22] M. Song and C. Dang, “Review on the measurement and calculation of frost characteristics,” *Int. J. Heat Mass Transf.*, vol. 124, pp. 586–614, 2018.

[23] P. Dinis Gaspar and P. D. Da Silva, Handbook of research on advances and applications in refrigeration systems and technologies. IGI Global; 1st Ed. Portugal, 2005 .

[24] D. Janssen, “Experimental strategies for frost analysis”. Ph.D. dissertation, Dept Mec. Eng. Mimesota, 2013

[25] H. Qiao and R. Radermacher, “Transient modeling of two-stage and variable refrigerant flow vapor compression systems with frosting and defrosting,”. Ph.D. disseration, Dept Mec.Eng. Maryland, 2014.

[26] L. Zhang, Y. Jiang, J. Dong, Y. Yao, and S. Deng, “A comparative study of frosting behavior on finned tube heat exchanger under different fan control modes,” *Appl. Therm. Eng.*, vol. 160, p. 114063, Sep. 2019.

[27] N. F. Aljuwayhel, “Numerical and Experimental Study of the Influence of Frost Formation and Defrosting on the Performance of Industrial Evaporator Coils,” 2006.

[28] H. *Lotz, “*Heat and mass transfer and pressure drop in frosting finned coils*,” in Refrigeration Science and Technology, Proceedings of the XII International Congress of Refrigeration, 1967, pp. 449–505.*

[29] A. Patin, “Optimisation des dégivrage par gaz chauds en chambre à basse temperature,” *Int. J. Refrig.*, vol. 13, no. 5, pp. 325–329, 1990.

[30] H. Chen, L. Thomas, and R. W. Besant, “Modeling frost characteristics on heat exchanger fins: Part II. Model Validation and Limitations,” *ASHRAE Trans.*, vol. 106, pp. 368–376, 2000.

[31] Y. Mao, H. Chen, and R. W. Besant, “Frost characteristics and heat transfer on a flat plate under freezer operating conditions: Part I, Experimentation and Correlations,” *ASHRAE Trans.*, vol. 105, 1999.

[32] H. Chen, L. Thomas, and R. W. Besant, “Modeling frost characteristics on heat exchanger fins: Part I. Numerical model,” *ASHRAE Trans.*, vol. 106, pp. 357–367, 2000.

[33] S. A. Sherif, P. J. Mago, N. K. Al-Mutawa, R. S. Theen, K. Bilen, and R. W. Besant, “Psychrometrics in the supersaturated frost zone,” *ASHRAE Trans.*, vol. 107 PART 2, pp. 753–767, 2001.

[34] P. Verma, C. W. Bullard, and P. S. Hrnjak, “Design Tool for Display Case Heat

Exchanger Frosting and Defrosting," Air conditioning and refrigeration center, Tech. Rep. TR-201, 2002.

[35] N. F. Aljuwayhel, D. T. Reindl, S. A. Klein, and G. F. Nellis, "Experimental investigation of the performance of industrial evaporator coils operating under frosting conditions," *Int. J. Refrig.*, vol. 31, no. 1, pp. 98–106, 2008.

[36] D. Seker, H. Karatas, and N. Egrican, "Frost formation on fin-and-tube heat exchangers. Part I - Modeling of frost formation on fin-and-tube heat exchangers," *Int. J. Refrig.*, vol. 27, no. 4, pp. 367–374, Jun. 2004.

[37] D. Seker, H. Karatas, and N. Egrican, "Frost formation on fin-and-tube heat exchangers. Part II - Experimental investigation of frost formation on fin-and-tube heat exchangers," *Int. J. Refrig.*, vol. 27, no. 4, pp. 375–377, Jun. 2004.

[38] N. F. Aljuwayhel, D. T. Reindl, S. A. Klein, and G. F. Nellis, "Comparison of parallel- and counter-flow circuiting in an industrial evaporator under frosting conditions," *Int. J. Refrig.*, vol. 30, no. 8, pp. 1347–1357, Dec. 2007.

[39] R. O. Piucco, C. J. L. Hermes, C. Melo, and J. R. Barbosa, "A study of frost nucleation on flat surfaces," *Exp. Therm. Fluid Sci.*, vol. 32, no. 8, pp. 1710–1715, Sep. 2008.

[40] C. J. L. Hermes, R. O. Piucco, J. R. Barbosa, and C. Melo, "A study of frost growth and densification on flat surfaces," *Exp. Therm. Fluid Sci.*, vol. 33, no. 2, pp. 371–379, Jan. 2009.

[41] Z. Cao, H. Han, B. Gu, and N. Ren, "A novel prediction model of frost growth on cold surface based on support vector machine," *Appl. Therm. Eng.*, vol. 29, no. 11–12, pp. 2320–2326, Aug. 2009.

[42] W. Wang, Q. C. Guo, W. P. Lu, Y. C. Feng, and W. Na, "A generalized simple model for predicting frost growth on cold flat plate," in *International Journal of Refrigeration*, 2012, vol. 35, no. 2, pp. 475–486.

[43] E. F. Kumala, R. A. Priramadhi, and P. Pangaribuan, "Frost Preventive Control System of Freezer," in *IOP Conference Series: Materials Science and Engineering*, 2018, vol. 434, no. 1.

[44] D. Badri, C. Toublanc, O. Rouaud, and M. Havet, "Dynamic modeling and simulation of frost formation on blast freezer heat exchanger.," *6th IIR Int. Conf. Sustain. Cold Chain. Proc. Nantes, Fr. August 26-28 2020*, 2020.

[45] P. L. T. Brian, R. C. Reid, and Y. T. Shah, "Frost Deposition on Cold Surfaces," *Ind. Eng. Chem. Fundam.*, vol. 9, no. 3, pp. 375–380, Aug. 1970.

[46] T. Kobayashi, "On the Habit of Snow Crystals Artificially Produced at Low Pressures," *J. Meteorol. Soc. Japan. Ser. II*, vol. 36, no. 5, pp. 193–208, 1958.

[47] K. Qu, S. Komori, and Y. Jiang, "Local variation of frost layer thickness and morphology," *Int. J. Therm. Sci.*, vol. 45, no. 2, pp. 116–123, Feb. 2006.

[48] X. Wu, W. Dai, W. Xu, and L. Tang, "Mesoscale investigation of frost formation on a cold surface," *Exp. Therm. Fluid Sci.*, vol. 31, no. 8, pp. 1043–1048, Aug. 2007.

[49] Y. . Lee and S. . Ro, "Frost formation on a vertical plate in simultaneously developing flow," *Exp. Therm. Fluid Sci.*, vol. 26, no. 8, pp. 939–945, Oct. 2002.

[50] L. M. Tajima O, H Yamada, U Kobayashi, "Frost Formation on Air Coolers, Part I : Natural Convection for a Flat Plate Facing Upwards," *Heat Tans. Japanese Res.*, vol. 1,

no. 2, pp. 39–48, 1972.

[51] C. J. Cremers and V. K. Mehra, “Frost Formation on Vertical Cylinders in Free Convection,” *J. Heat Transfer*, vol. 104, no. 1, p. 3, 1982.

[52] H. Do Han and S. T. Ro, “The characteristics of frost growth on parallel plates,” in *Advances in Cold-Region Thermal Engineering and Sciences*, Springer Berlin Heidelberg, pp. 55–64.

[53] A. Leoni, “Etude Experimentale et modelisation de la formation et du developpement du givre sur une plaque refroidie, ” Ph.D. dissertation, CETHIL. Lyon University, 2017.

[54] Y. Hayashi, A. Aoki, S. Adachi, and K. Hori, “Study of frost properties correlating with frost formation types,” *J. Heat Transfer*, vol. 99, no. 2, pp. 239–245, 1977.

[55] A. Leoni, M. Mondot, F. Durier, R. Revellin, and P. Haberschill, “Frost formation and development on flat plate: Experimental investigation and comparison to predictive methods,” *Exp. Therm. Fluid Sci.*, vol. 88, pp. 220–233, 2017.

[56] D. L. O’Neal and D. R. D. Tree, “A review of frost formation in simple geometries,” *ASHRAE Trans.*, no. June 1985, pp. 267–281, 1985.

[57] E. Moallem, L. Cremaschi, D. E. Fisher, and S. Padhmanabhan, “Experimental measurements of the surface coating and water retention effects on frosting performance of microchannel heat exchangers for heat pump systems,” *Exp. Therm. Fluid Sci.*, vol. 39, pp. 176–188, 2012.

[58] M. Amini, A. R. Pishevar, and M. Yaghoubi, “Experimental study of frost formation on a fin-and-tube heat exchanger by natural convection,” *Int. J. Refrig.*, vol. 46, pp. 37–49, Oct. 2014.

[59] A. Léoni, M. Mondot, F. Durier, R. Revellin, and P. Haberschill, “State-of-the-art review of frost deposition on flat surfaces,” *Int. J. Refrig.*, vol. 68, pp. 198–217, 2016.

[60] H. W. Schneider, “Equation of the growth forming on cooled,” *Int. J. Heat Mass Transf.*, vol. 21, no. 8, pp. 1019–1024, 1978.

[61] Y. Barzanoni, O. Noorshams, H. B. Tabrizi, and E. Damangir, “Experimental investigation of frost formation on a horizontal cold cylinder under cross flow,” *Int. J. Refrig.*, vol. 34, no. 4, pp. 1174–1180, Jun. 2011.

[62] D. L. O’Neal and D. R. Tree, “Measurement of frost growth and density in a parallel plate geometry,” *ASHRAE Trans.*, vol. 90, no. 2, pp. 278–290, 1984.

[63] K.-S. Lee, W.-S. Kim, and T.-H. Lee, “A one-dimensional model for frost formation on a cold flat surface,” *Int. J. Heat Mass Transf.*, vol. 40, no. 18, pp. 4359–4365, Nov. 1997.

[64] A. El Cheikh and A. Jacobi, “A mathematical model for frost growth and densification on flat surfaces,” *Int. J. Heat Mass Transf.*, vol. 77, pp. 604–611, 2014.

[65] T. H. Lee, K. S. Lee, and W. S. Kim, “The Effects of Frost Formation in a Flat Plate Finned-Tube Heat Exchanger,” in *International Refrigeration and Air Conditioning Conference*, 1996.

[66] X. Liping, G. Xianmin, and X. Zhen, “Experimental Study of Frost Growth Characteristics on Surface of Fin-tube Heat Exchanger,” *Energy Procedia*, vol. 105, pp. 5114–5121, May 2017.

[67] J. Cui, W. Z. Li, Y. Liu, and Y. S. Zhao, “A new model for predicting performance of fin-and-tube heat exchanger under frost condition,” *Int. J. Heat Fluid Flow*, vol. 32, no.

1, pp. 249–260, Feb. 2011.

[68] J. Cui, W. Z. Li, Y. Liu, and Z. Y. Jiang, “A new time- and space-dependent model for predicting frost formation,” *Appl. Therm. Eng.*, vol. 31, no. 4, pp. 447–457, Mar. 2011.

[69] D. Kim, C. Kim, and K. S. Lee, “Frosting model for predicting macroscopic and local frost behaviors on a cold plate,” *Int. J. Heat Mass Transf.*, vol. 82, pp. 135–142, Mar. 2015.

[70] J. S. Kim, K. S. Lee, and S. J. Yook, “Frost behavior on a fin considering the heat conduction of heat exchanger fins,” *Int. J. Heat Mass Transf.*, vol. 52, no. 11–12, pp. 2581–2588, May 2009.

[71] D. K. Yang, K. S. Lee, and D. J. Cha, “Frost formation on a cold surface under turbulent flow,” *Int. J. Refrig.*, vol. 29, no. 2, pp. 164–169, Mar. 2006.

[72] B. W. Jones and J. D. Parker, “Frost formation with varying environmental parameters,” *J. Heat Transfer*, vol. 97, no. 2, pp. 255–259, May 1975.

[73] B. Na and R. L. Webb, “New model for frost growth rate,” *Int. J. Heat Mass Transf.*, vol. 47, no. 5, pp. 925–936, Feb. 2004.

[74] B. Na and R. L. Webb, “Mass transfer on and within a frost layer,” *Int. J. Heat Mass Transf.*, vol. 47, no. 5, pp. 899–911, Feb. 2004.

[75] K. S. Lee, S. Jhee, and D. K. Yang, “Prediction of the frost formation on a cold flat surface,” *Int. J. Heat Mass Transf.*, vol. 46, no. 20, pp. 3789–3796, 2003.

[76] D. K. Yang and K. S. Lee, “Modeling of frosting behavior on a cold plate,” in *International Journal of Refrigeration*, 2005, vol. 28, no. 3, pp. 396–402.

[77] K. Lenic, A. Trp, and B. Frankovic, “Transient two-dimensional model of frost formation on a fin-and-tube heat exchanger,” *Int. J. Heat Mass Transf.*, vol. 52, no. 1–2, pp. 22–32, Jan. 2009.

[78] K. Lenic, A. Trp, and B. Frankovic, “Prediction of an effective cooling output of the fin-and-tube heat exchanger under frosting conditions,” *Appl. Therm. Eng.*, vol. 29, no. 11–12, pp. 2534–2543, Aug. 2009.

[79] X. Wu, Q. Ma, and F. Chu, “Numerical simulation of frosting on fin-and-tube heat exchanger surfaces,” *J. Therm. Sci. Eng. Appl.*, vol. 9, no. 3, Sep. 2017.

[80] J. M. Armengol, C. T. Salinas, J. Xamán, and K. A. R. Ismail, “Modeling of frost formation over parallel cold plates considering a two-dimensional growth rate,” *Int. J. Therm. Sci.*, vol. 104, pp. 245–256, Jun. 2016.

[81] J. Lee, J. Kim, D. R. Kim, and K.-S. Lee, “Modeling of frost layer growth considering frost porosity,” *Int. J. Heat Mass Transf.*, vol. 126, pp. 980–988, Nov. 2018.

[82] S. N. Kondepudi and D. L. O’Neal, “Frosting performance of tube fin heat exchangers with wavy and corrugated fins,” *Exp. Therm. Fluid Sci.*, vol. 4, no. 5, pp. 613–618, Sep. 1991.

[83] R. Le Gall, J. M. Grillot, and C. Jallut, “Modelling of frost growth and densification,” *Int. J. Heat Mass Transf.*, vol. 40, no. 13, pp. 3177–3187, Sep. 1997.

[84] S. Fukada and K. Inoue, “Internal mass flux through frost,” *intern*, vol. 45, no. 12, pp. 2646–2652, Dec. 1999.

[85] Y. B. Lee and S. T. Ro, “Analysis of the frost growth on a flat plate by simple models of

saturation and supersaturation," *Exp. Therm. Fluid Sci.*, vol. 29, no. 6, pp. 685–696, Jul. 2005.

[86] A. R. Tahavvor and M. Yaghoubi, "Experimental and numerical study of frost formation by natural convection over a cold horizontal circular cylinder," *Int. J. Refrig.*, vol. 33, no. 7, pp. 1444–1458, Nov. 2010.

[87] M. Kandula, "Frost growth and densification in laminar flow over flat surfaces," *Int. J. Heat Mass Transf.*, vol. 54, no. 15–16, pp. 3719–3731, 2011.

[88] C. P. Tso, Y. C. Cheng, and A. C. K. Lai, "An improved model for predicting performance of finned tube heat exchanger under frosting condition, with frost thickness variation along fin," *Appl. Therm. Eng.*, vol. 26, no. 1, pp. 111–120, Jan. 2006.

[89] F. Brèque and M. Nemer, "Frosting modeling on a cold flat plate: Comparison of the different assumptions and impacts on frost growth predictions," *Int. J. Refrig.*, vol. 69, pp. 340–360, Sep. 2016.

[90] Y. Yao, Y. Jiang, S. Deng, and Z. Ma, "A study on the performance of the airside heat exchanger under frosting in an air source heat pump water heater/chiller unit," *Int. J. Heat Mass Transf.*, vol. 47, no. 17–18, pp. 3745–3756, Aug. 2004.

[91] V. Mulot, H. Benkhelifa, D. Pathier, F. T. Ndoye, and D. Flick, "Measurement of food dehydration during freezing in mechanical and cryogenic freezing conditions," *Int. J. Refrig.*, vol. 103, pp. 329–338, Jul. 2019.

[92] B. H. Ashby, G. M. James, and A. Kramer, "Effects of freezing and packaging methods onn shrinkage of hams in frozen storage," *J. Food Sci.*, vol. 38, no. 2, pp. 254–257, Feb. 1973.

[93] S. J. Schmidt and J. W. Lee, "How Does the Freezer Burn Our Food?," *J. Food Sci. Educ.*, vol. 8, no. 2, pp. 45–52, Apr. 2009.

[94] F. Franks, "Freeze-drying of bioproducts: putting principles into practice," J. Pharm Biopharm., vol. 221, 1998.

[95] Y. Phimolsiripol, R. . Love, and D. . Cleland, "Verification of a simple product weight loss model for refrigerated storage of foods," in *Proceedings of the Third IIR International Conference on Sustainability and the Cold Chain, London*, 2014.

[96] M. G. Landerslev, A. Araya-Morice, L. Pomponio, and J. Ruiz-Carrascal, "Weight loss in superchilled pork as affected by cooling rate," *J. Food Eng.*, vol. 219, pp. 25–28, Feb. 2018.

[97] L. A. Campañone, V. O. Salvadori, and R. H. Mascheroni, "Weight loss during freezing and storage of unpackaged foods," *J. Food Eng.*, vol. 47, no. 2, pp. 69–79, Feb. 2001.

[98] R. Powell, "Further experiments on the evaporation of water from saturated surfaces," J. *Engineering.*, vol. 60, pp 236-256,1940.

[99] O. Laguerre and D. Flick, "Frost formation on frozen products preserved in domestic freezers," *J. Food Eng.*, vol. 79, no. 1, pp. 124–136, Mar. 2007.

[100] O. M. Bustabad, "Weight loss during freezing and the storage of frozen meat," *J. Food Eng.*, vol. 41, no. 1, pp. 1–11, Jul. 1999.

[101] R. C. Martins, M. G. Almeida, and C. L. M. Silva, "The effect of home storage conditions and packaging materials on the quality of frozen green beans," *Int. J. Refrig.*, vol. 27, no. 8, pp. 850–861, Dec. 2004.

[102] B. Doytcheva, A. Nikolova, G. Peev, and D. Todorova, “Mass transfer from a single grain to a fluid in an inert fixed bed,” *Int. Commun. Heat Mass Transf.*, vol. 25, no. 3, pp. 399–405, Apr. 1998.

[103] A. M. Tocci and R. H. Mascheroni, “Heat and mass transfer coefficients during the refrigeration, freezing and storage of meats, meat products and analogues,” *J. Food Eng.*, vol. 26, no. 2, pp. 147–160, Jan. 1995.

[104] K. Norne Widell, *Kristina Norne Widell Energy efficiency of freezing tunnels Kristina Norne Widell Energy efficiency of freezing tunnels*. 2012.

[105] G. Buisard, “Le traitement des surgélateurs et congélateurs en industries agro alimentaires,” pp. 25-7, 12 july, 2011. Available: http://gbuisard.chez.com/main7.html. [Accessed Dec. 2, 2021].

[106] G. Smith, “Theoretical cooling coil calculations at freezer temperatures to avoid unfavourable coil frost,” *ASHRAE Trans.*, vol. 95, no. 2, pp. 1138–1148, 1989.

[107] G. Smith, “Latent heat, equipment-related load, and applied psychrometrics at freezer temperatures.,” *ASHRAE Trans.*, vol. 98, no. 2, pp. 649–657, 1998.

[108] D.T. Reindl, “Defrosting industrial refrigeration evaporators., ” *ASHRAE J.*, vol. 51, no. August, 2009.

[109] D. Q. Deng, L. Xu, and S. Q. Xu, “Experimental investigation on the performance of air cooler under frosting conditions,” *Appl. Therm. Eng.*, vol. 23, no. 7, pp. 905–912, 2003.

[110] N. F. Aljuwayhel, D. T. Reindl, S. A. Klein, and G. F. Nellis, “Experimental investigation of the performance of industrial evaporator coils operating under frosting conditions,” *Int. J. Refrig.*, vol. 31, no. 1, pp. 98–106, Jan. 2008.

[111] Y. Xia, Y. Zhong, P. S. Hrnjak, and A. M. Jacobi, “Frost, defrost, and refrost and its impact on the air-side thermal-hydraulic performance of louvered-fin, flat-tube heat exchangers,” *Int. J. Refrig.*, vol. 29, no. 7, pp. 1066–1079, 2006.

[112] H. Chen, L. Thomas, and R. W. Besant, “Modeling frost characteristics on heat exchanger fins: Part I. Numerical model,” *ASHRAE Trans.*, vol. 106, pp. 368–376, 2000.

[113] W. B. Wagner, “Frost formation on a Extended Surface Heat Exchanger in Crossflow of Humid Air,” Ohio state University, 1963.

[114] D. L. Da Silva, C. J. L. Hermes, and C. Melo, “First-principles modeling of frost accumulation on fan-supplied tube-fin evaporators,” *Appl. Therm. Eng.*, vol. 31, no. 14–15, pp. 2616–2621, Oct. 2011.

[115] R. W. Rite and R. R. Crawford, “The Effect of Frosting on the Performance of Domestic Refrigerator-Freezer Finned Tube Evaporator Coils,” Ph.D dissertation, Illinois University, 1990.

[116] O’Hagan, “The Effect of Favourable and Unfavourable Frost on Air Cooling.” Ph.D dissertation, Massey University, 1994.

[117] T. Gatchilov and V. Ivanova, “Characteristics of the frost formed on the surface of the finned air coolers,” in *XV International Congress of Refrigeration, Venice*, 1979.

[118] B. Gin, M. M. Farid, and P. K. Bansal, “Effect of door opening and defrost cycle on a freezer with phase change panels,” *Energy Convers. Manag.*, vol. 51, no. 12, pp. 2698–2706, Dec. 2010.

[119] R. Zhao, D. Huang, Z. Zhang, and Y. Leng, “Effect of defrost heat leakage on freezer

temperature rise during periodical defrost cycles in a frost-free refrigerator–freezer with an electric defrost heater," *Sci. Technol. Built Environ.*, vol. 23, no. 1, pp. 211–217, Jan. 2017.

[120] M. Amer, C. Wang, M. Amer, and C. Wang, "Review of defrosting methods," *Renew. Sustain. Energy Rev.*, vol. 73, no. June, pp. 53–74, 2017.

[121] M. Song, S. Deng, C. Dang, N. Mao, and Z. Wang, "Review on improvement for air source heat pump units during frosting and defrosting," *Applied Energy*, vol. 211. Elsevier Ltd, pp. 1150–1170, 01-Feb-2018.

[122] N. Hoffenbecker, S. A. Klein, and D. T. Reindl, "Hot gas defrost model development and validation," *Int. J. Refrig.*, vol. 28, no. 4, pp. 605–615, Jun. 2005.

[123] J. A. Dopazo and J. Fernandez, "Modelling and experimental validation of the hot-gas defrost process of an air-cooled evaporator," *Int. J. Refrig.*, vol. 33, pp. 829–839, 2010.

[124] D. H. Niederer, "Frosting and Defrosting Effects on Coil Heat Transfer," *ASHRAE Trans.*, vol. 82, pp. 467–473, 1976.

[125] R.A. Cole, "Refrigeration loads in a freezer due to hot gas defrost and their associated costs," 1989, pp. 1149–1154.

[126] L. Pu *et al.*, "Experimental study of cyclic frosting and defrosting on microchannel heat exchangers with different coatings," *Energy Build.*, vol. 226, p. 110382, Nov. 2020.

[127] F. Wang, C. Liang, M. Yang, C. Fan, and X. Zhang, "Effects of surface characteristic on frosting and defrosting behaviors of fin-tube heat exchangers," *Appl. Therm. Eng.*, vol. 75, pp. 1126–1132, Jan. 2015.

[128] C. S. Heu *et al.*, "Frosting and defrosting behavior of slippery surfaces and utilization of mechanical vibration to enhance defrosting performance," *Int. J. Heat Mass Transf.*, vol. 125, pp. 858–865, Oct. 2018.

[129] L. Cai, R. Wang, P. Hou, and X. Zhang, "Study on restraining frost growth at initial stage by hydrophobic coating and hygroscopic coating," *Energy Build.*, vol. 43, no. 5, pp. 1159–1163, 2011.

[130] Z. Liu, H. Wang, X. Zhang, S. Meng, and C. Ma, "An experimental study on minimizing frost deposition on a cold surface under natural convection conditions by use of a novel anti-frosting paint. Part II. Long-term performance, frost layer observation and mechanism analysis," *Int. J. Refrig.*, vol. 29, no. 2, pp. 237–242, Mar. 2006.

[131] C. M. Joppolo, L. Molinaroli, S. De Antonellis, and U. Merlo, "Experimental analysis of frost formation with the presence of an electric field on fin and tube evaporator," *Int. J. Refrig.*, vol. 35, no. 2, pp. 468–474, Mar. 2012.

[132] D. Wang, T. Tao, G. Xu, A. Luo, and S. Kang, "Experimental study on frosting suppression for a finned-tube evaporator using ultrasonic vibration," *Exp. Therm. Fluid Sci.*, vol. 36, pp. 1–11, 2012.

[133] K.-S. Lee and W.-S. Kim, "The effects of design and operating factors on the frost growth and thermal performance of a flat plate fin-tube heat exchanger under the frosting condition," *KSME Int. J.*, vol. 13, no. 12, pp. 973–981, Dec. 1999.

[134] D. L. Silva and C. J. L. Hermes, " Optimal defrost cycle for air coolers revisited: a study of fan-supplied tube-fin evaporators," *Int. J. Refrig.*, vol. 89, 2018.

[135] L.-L. Shao, L. Yang, and C.-L. Zhang, "Comparison of heat pump performance using

fin-and-tube and microchannel heat exchangers under frost conditions," *Appl. Energy*, vol. 87, no. 4, pp. 1187–1197, 2010.

[136] K. Kim and K. S. Lee, "Frosting and defrosting characteristics of surface-treated louvered-fin heat exchangers: Effects of fin pitch and experimental conditions," *Int. J. Heat Mass Transf.*, vol. 60, no. 1, pp. 505–511, 2013.

[137] Y. Jiang, J. Dong, M. Qu, S. Deng, and Y. Yao, "A novel defrosting control method based on the degree of refrigerant superheat for air source heat pumps," *Int. J. Refrig.*, vol. 36, no. 8, pp. 2278–2288, Dec. 2013.

[138] T. R. Buick, J. T. McMullan, R. Morgan, and R. B. Murray, "Ice detection in heat pumps and coolers," *Int. J. Energy Res.*, vol. 2, no. 1, pp. 85–98, Jan. 1978.

[139] X. Li, Y. Li, and J. E. Seem, "International Refrigeration and Air Conditioning Conference. Paper 1094. *Proceeeding in International Refrigeration and Air Conditioning Conference at Purdue*," 2010.

[140] J. M. Maldonado *et al.*, "Frost detection method on evaporator in vapour compression systems," *Int. J. Refrig.*, vol. 110, pp. 75–82, Feb. 2020.

[141] P. D. Cleland, "Unfavorable frost - what is it, when does it occurs and how can it be avoided," *Aust. Inst. Refrig.* vol. 2, no. August, pp. 16–20, 2004.

[142] H. Chen, "Modeling and Measurement of Frost Characteristics on Heat Exchanger Surfaces," *Mol. Biol.*, p. xxi, 2000.

[143] S. W. Wang and Z. Y. Liu, "A new method for preventing HP from frosting," *Renew. Energy*, vol. 30, no. 5, pp. 753–761, Apr. 2005.

[144] L. Zhang, T. Fujinawa, and M. Saikawa, "Theoretical study on a frost-free household refrigerator-freezer," *Int. J. Refrig.*, vol. 62, pp. 60–71, Feb. 2016.

[145] Z. Wang *et al.*, "Experimental analysis on a novel frost-free air-source heat pump water heater system," *Appl. Therm. Eng.*, vol. 70, no. 1, pp. 808–816, Sep. 2014.

[146] P. Vivekh, M. Kumja, D. T. Bui, and K. J. Chua, "Recent developments in solid desiccant coated heat exchangers – A review," *Appl. Energy*, vol. 229, pp. 778–803, Nov. 2018.

[147] D.B. Thierry and P. Didier, "Systeme ameliorant les problemes de givrage dans les tunnels de surgelation par impaction," Patent, Sep. 2012.

[148] P. Fritzson, "Introduction to Object-Oriented Modeling and Simulation with Modelica Using OpenModelica," *Wiley Press; 2nd Ed* Nov. 2014.

[149] L. R. Petzold, "Description of DASSL: a differential/algebraic system solver." in *Proceedings of the 10th IMACS World Congress.* Sep.1982.

[150] A. Steiner and R. Rieberer, "Simulation based identification of the ideal defrost start time for a heat pump system for electric vehicles," *Int. J. Refrig.*, vol. 57, pp. 87–93, Jul. 2015.

[151] A. Steiner and R. Rieberer, "Parametric analysis of the defrosting process of a reversible heat pump system for electric vehicles," *Appl. Therm. Eng.*, vol. 61, no. 2, pp. 393–400, Nov. 2013.

[152] Y. Zhang, "System-Oriented Dynamic Modelling and Power Consumption Simulation for an Industrial Chiller Plant." Ph.D Dissertation, Stockholm, 2020.

[153] S. Mortada, A. Zoughaib, D. Clodic, and C. Arzano-Daurelle, "Dynamic modeling of an integrated air-to-air heat pump using Modelica," *Int. J. Refrig.*, vol. 35, no. 5, pp. 1335–

1348, Aug. 2012.

[154] M. Wetter, W. Zuo, T. S. Nouidui, and X. Pang, “Modelica Buildings library,” *J. Build. Perform. Simul.*, vol. 7, no. 4, pp. 253–270, Jul. 2014.

[155] H. Tummescheit, “Design and Implementation of Object-Oriented Model Libraries using Modelica.” Ph.D Dissertation, Lund University. 2002.

[156] C. C. Richter and : Braunschweig, “Proposal of New Object-Oriented Equation-Based Model Libraries for Thermodynamic Systems.” Ph.D Dissertation. 2008.

[157] N.-C. Strupp, N. Lemke, W. Tegethoff, and J. Köhler, “Investigation of low pressure accumulators in CO2 refrigeration cycles.,” in *ICR 2007. Refrigeration Creates the Future. Proceedings of the 22nd IIR International Congress of Refrigeration.*, 2007.

[158] M. Bockholt, W. Tegethoff, N. Lemke, N. Strupp, and C. Richter, “Transient Modelling of a Controllable Low Pressure Accumulator in CO2 Refrigeration Cycles,” *in* Modelica, March 3rd −4th, 2008.

[159] *VDI Heat Atlas*. Springer Berlin Heidelberg, 2010.

[160] E. W. Lemmon, I. H. Bell, M. L. Huber, and M. O. Mclinden, “REFPROP Documentation Release 10.0,” 2021.

[161] S. Försterling, *Vergleichende Untersuchung von CO2-Verdichtern in Hinblick auf den Einsatz in mobilen Anwendungen*, 1st ed. 2004.

[162] H. Auracher, “Water vapor diffusion and frost formation in capillaries Annex 1972-1,” *Bull. Int. Inst. Refrig.*, pp. 477–488, 1972.

[163] D. P. Dewitt, F. Incropera, A. Lavine “Fundamentals of Heat and Mass Transfer,” John Wiley & sons, 7th Ed. United States, 2011.

[164] Hadid Z, Zoughaib A, Bariteau N, and Robidou H, “Moding ice formation on heat exchangers fin.” *in Proceedings of the International Conference of refrigeration*, August, 2011.

[165] E. E. R. Georg and R. Drake Jr, *Analysis of heat and mass transfer*, 1 décembre. 1972.

[166] Z. Hadid, “Gazéification du GNL par cycle de Brayton associé à une boucle caloportrice et une pompe à chaleur.” Ph.D. Dissertation, Paris. 2012.

[167] S. A. Sherif, S. P. Raju, M. M. Padki, and A. B. Chan, “A semi-empirical transient method for modelling frost formation on a flat plate,” *Int. J. Refrig.*, vol. 16, no. 5, pp. 321–329, Jan. 1993.

[168] A. Z. Şahin, “An analytical study of frost nucleation and growth during the crystal growth period,” *Heat Mass Transf.*, vol. 30, no. 5, pp. 321–330, Jun. 1995.

[169] M. Owen, Ed., *Ashrae Handbook: fundamentals*, SI. 2005.

[170] H. D. Baehr and K. Stephan, Heat and mass transfer, Springer, Second Edition, 2017.

[171] A. Leoni, M. Mondot, F. Durier, R. Revellin, and P. Haberschill, “Frost formation and development on flat plate: Experimental investigation and comparison to predictive methods,” *Exp. Therm. Fluid Sci.*, vol. 88, pp. 220–233, Nov. 2017.

[172] C. Kim, J. Lee, and K.-S. Lee, “Numerical modeling of frost growth and densification on a cold plate using frost formation resistance,” *Int. J. Heat Mass Transf.*, vol. 115, pp. 1055–1063, Dec. 2017.

[173] J. Westhäuser, Z. You, J. Albrecht, N. Lemke, and J. Köhler, “Untersuchung der

Vereisung von Mikrokanal-Wärmeübertragern.", DKV Tagung. Aachen, 2018.

[174] S. K. Padhmanabhan, D. E. Fisher, L. Cremaschi, and E. Moallem, "Modeling non-uniform frost growth on a fin-and-tube heat exchanger," in *International Journal of Refrigeration*, 2011, vol. 34, no. 8, pp. 2018–2030.

[175] R. K. Shah and A. L. London, *Laminar Flow Forced Convection in Ducts - 1st Edition*, 1st Edition. 1978.

[176] S. Haaf, "Wärmeübertragung in Luftkühlern," in *Wärmeaustauscher*, Springer Berlin Heidelberg, 1988, pp. 435–491.

[177] W. Tegethoff, *Eine objektorientierte Simulationsplattform für Kälte-, Klima- und Wärmepumpensysteme*. VDI-Verl, 1999.

[178] R. Schmidt, *Eine Methode zur numerischen Untersuchung von Strömung und Wärmeübertragung in komplexen Geometrien*. Ibidem-Verl, 2003.

[179] M. H. Sharqawy, M. A. Antar, S. M. Zubair, and A. M. Elbashir, "Optimum thermal design of humidification dehumidification desalination systems," *Desalination*, vol. 349, pp. 10–21, Sep. 2014.

[180] C. T. Sanders, "Frost formation : The influence of frost formation and defrosting on the performance of air coolers," Ph.D. Dissertation, 1974.

[181] S. Kondepudi, "The Effects of Frost Growth on Finned Tube Heat Exchangers under Laminar Flow," Ph.D. Dissertation. Texas University,1988.

[182] J. Liu, Q. Li, F. Wang, and L. Zhou, "A new model of screw compressor for refrigeration system simulation," in *International Journal of Refrigeration*, 2012, vol. 35, no. 4, pp. 861–870.

[183] "EnergyPlus." [Online]. Available: https://energyplus.net/weather. [Accessed: 23-Oct-2021].

[184] O. Rouaud and Q. T. Pham, "Heat and mass transfer modelling during freezing of foodstuffs," *2012 COMSOL Conf.*, no. July, 2012.

[185] G. Saravacos and A. E. Kostaropoulos, "Food Engineering Series Handbook of Food Processing Equipment." Second Ed, USA. 2016

DOCTORAT BRETAGNE LOIRE SCIENCES POUR L'INGENIEUR

Oniris École Nationale Vétérinaire, Agroalimentaire et de l'Alimentation Nantes Atlantique — Santé et alimentation au cœur de la vie

UNIVERSITÉ DE NANTES

Titre : Etude numérique de la formation de givre dans un système industriel de surgélation

Mots clés : Modélisation, Givre, Surgélation, Energétique.

Résumé : La gestion du givre est une problématique majeure pour une très large majorité des industriels du secteur agroalimentaire. Pour ces entreprises, les processus de givrage et dégivrage représentent un surcoût énergétique, une perte de productivité et une détérioration de la qualité des produits.

Cette thèse a pour ambition de modéliser en langage Modelica un système industriel de surgélation et d'évaluer l'impact de la formation de givre sur ses performances. Dans ces conditions très spécifiques de surgélation à très basse température où les modèles conventionnels font défaut, un modèle physique de formation de givre a été développé, validé et introduit dans celui de l'évaporateur de type tubes-ailettes d'un surgélateur industriel. Les résultats de simulation présentent une bonne concordance avec des relevés expérimentaux réalisés sur site en conditions réelles de production.

Le modèle numérique est ensuite exploité pour étudier les caractéristiques et la distribution de givre tout au long de l'évaporateur. Ces caractéristiques sont reliées au comportement thermo-hydraulique de l'évaporateur lors de sa prise en givre.

L'effet du givre a été analysé sur la productivité de l'équipement et sur la qualité des produits. Un des résultats importants concerne les indicateurs de performance énergétiques locaux (puissance frigorifique, rendement des compresseurs, etc.), globaux (COP, IPE) et des indicateurs de qualité de produits. Cette étude s'est ensuite étendue au système complet pour décrire le comportement de chaque composant (notamment compresseurs et ventilateurs).

Une étude de sensibilité menée sur le taux de pertes d'eau des produits a permis d'évaluer l'impact de ce paramètre sur le fonctionnement de surgélateurs.

Une comparaison du mode de fonctionnement des ventilateurs a été présentée.

Finalement, des recommandations sont proposées ainsi que des perspectives pour de travaux de futurs.

Title: Numerical study of frost formation on an industrial food freezing system

Keywords: Modeling, Frost Freezing, Energy

Abstract: Frost management is a major problem that concerns the vast majority of manufacturers in the agri-food sector. For these companies, frosting and defrosting processes represent an additional energy cost, a loss of productivity and a deterioration in the quality of their food products.

In this thesis work, an industrial freezing system has been modeled using Modelica language. A physical model of frost formation was first developed, validated and then introduced into the tube-fin evaporator model of the freezer.

The simulations results show a good agreement with experimental results carried out on a production day. The numerical model was then used in order to study the characteristics and distribution of frost throughout the evaporator.

This study has been extended to the whole system in order to describe the behavior of each component (especially compressors and fans). The model also takes into account the food products. Therefore, the effect of frost was analyzed on the product quality and the productivity of the freezer. Simulations were carried out to follow local energy performance indicators (cooling capacity, compressor efficiency, etc.), global indicators (COP) and product quality indicators.

A sensitivity study was performed in order to quantify the effect of product water losses on the performance of the freezing system. A fan control mode comparison has been presented. Finally, solutions for geometry optimization and guidelines were proposed as well as perspectives for future work.